ISTANBUL TECHNICAL UNIVERSITY ★ GRADUATE SCHOOL

LAB-SCALE DC ELECTRIC ARC FURNACE DESIGN AND THERMODYNAMIC SLAG OPTIMIZATION FOR METAL RECOVERY FROM SLAG PHASE

M.Sc. THESIS

Mert SARAÇOĞLU

(521211019)

Department of Materials Science and Engineering

Materials Science and Engineering Programme

Thesis Advisor: Prof. Dr. Servet İbrahim TİMUR

JANUARY 2024

ISTANBUL TEKNİK ÜNİVERSİTESİ ★ LİSANSÜSTÜ EĞİTİM ENSTİTÜSÜ

CÜRUF FAZINDAN METAL GERİ KAZANIMI İÇİN LABORATUVAR ÖLÇEKLİ DC ELEKTRİK ARK FIRINI TASARIMI VE TERMODİNAMİK CÜRUF OPTİMİZASYONU

YÜKSEK LİSANS TEZİ

Mert SARAÇOĞLU

Malzeme Bilimi ve Mühendisliği Departmanı

Malzeme Bilimi ve Mühendisliği Bölümü

Tez Danışmanı: Prof. Dr. Servet İbrahim TİMUR

OCAK 2024

Mert SARAÇOĞLU, a M.Sc. student of ITU Graduate School student ID 521211019, successfully defended the thesis entitled "LAB-SCALE DC ELECTRIC ARC FURNACE DESIGN AND THERMODYNAMIC SLAG OPTIMIZATION FOR METAL RECOVERY FROM SLAG PHASE", which he prepared after fulfilling the requirements specified in the associated legislations, before the jury whose signatures are below.

Thesis Advisor :	**Prof. Dr. Servet İbrahim TİMUR** Istanbul Technical University	.....
Jury Members :	**Prof. Dr. Servet İbrahim TİMUR** Istanbul Technical University	.....
	Prof. Dr. Güldem KARTAL ŞİRELİ Istanbul Technical University	.....
	Dr.Öğr.Üyesi Hatice Kübra AKBEN Yeditepe University	.....

Date of Submission : 04.01.2024

Date of Defense : 22.01.2024

To the lights that guide me,

FOREWORD

Within the scope of this thesis, I have received numerous support and assistance from my friends, family, mentors, and esteemed colleagues in academia. Each of them has had an impact on my development, and I am grateful to all of them.

I extend my gratitude to Mr. Ümit SÖNMEZ and Mr. Aytuğ FONT from SÖNMEZ TRANSFORMER, who provided us with a power source transformer for use in my thesis. I also appreciate Vessem RECYCLING for supplying the ceramic converters used in the thesis, NADIR Metal Refinery Inc. and Mr. Murat Çınarlı for providing refractories, NADIR Metal Refinery Inc. for supplying the construction of the arc furnace and slag samples, and Mr. Hanife ÖZTÜRK and Mr. Mahmut EROL.

I am thankful to Mr. Sami OĞUZBAL Usta and his valuable team from ATM Energy, our cherished family friend and mentor, for showing me the system electricity, assisting in electrical connections, and helping with transformer installation.

I express my gratitude to Ar. Gör. Bora AYVAZ and Süleyman Semih KARAMAN, my colleagues with whom I enjoyed working on the automation of the electric arc system. Special thanks to Ar. Gör. Utku Orçun GEZİCİ, , who prioritized my needs before his own.

Since the nights I started working in the laboratory, where I sometimes slept on his couch, I thank Ar. Gör. Mehtap ARSLAN KABA for providing all the equipment. I am also grateful to my mechanical engineer friends, Mert UYGUN, Yavuz YARDIMCI, and Taha TOPAL, who sacrificed their time to help me with mechanical design, and Ar. Gör. Göksel HIZLI for guiding me in drawing mechanical design sketches and manufacturing system parts in the industry.

I express my appreciation to Ar. Gör. Erdem BALCI, who assisted in optical imaging, and to my lifelong camping friends, especially Doğukan DUYMAZ, who supported me both financially and morally throughout my thesis process.

My sincere thanks to Mubashir MANSOOR, who enhanced my scientific research perspective and provided invaluable experience in various fields during our late-night studies.

I am grateful to my dear friend Kağan HEPER, who generously helped in finding phases and X-ray diffraction. Special thanks to Rıdvan ORMAN, who ran to my aid before and during his thesis process whenever I faced problems.

I extend my thanks to Sevde Rana GÜNAL, the source of joy in the laboratory, for standing by me in every difficulty.

Special thanks to my elder brothers at Nanosilver Chemical Industry Trade Inc., Tanra GÜRÇAY and Rona GÜRÇAY, who helped turn my academic studies into tangible products, combining industry and market realities with academic insights.

I am thankful to Ar. Gör. Kerem Can DİZDAR for assisting me in all thermodynamic calculations and helping me obtain all the results in the theoretical part of this thesis. His cheerful attitude and helpfulness greatly shorthened my thesis process. I also express my gratitude to Prof. Dr. Bora DERİN, for providing the opportunity for FactSage calculations.

I express my gratitude to my uncle, Faruk DİKEN, who, regardless of his health issues, assisted me in building the electric arc furnace, crowning the theoretical part of this thesis with practical expertise gained throughout my university life.

I am indebted to my beloved mother, Ayşegül SARAÇOĞLU, for always prioritizing me, identifying and addressing each of my shortcomings in my student life,

Since the day I entered university, I am grateful to Prof. Dr. Servet TİMUR, who accepted me as a colleague, provided a scientific freedom in our research environment for five years, and not only taught me engineering but also life and communication with people. He has been a guiding light on the path of my self-discovery, and I will forever feel indebted to him.

I present my heartfelt thanks to all mentioned above.

Ocak 2024

Mert Saraçoğlu
(Material and Metallurgical Engineer)

TABLE OF CONTENTS

Page

ABBREVIATIONS

AOD	**:** Argon oxygen decarburization furnace
BF	**:** Blast furnace
BOF	**:** Basic oxygen furnace
DC	**:** Direct current
DSC	**:** Dynamic scanning calorimetry
EAF	**:** Electrical arc furnace
LOI	**:** Loss of ignition
MSW	**:** Municipal solid waste
NCA	**:** X-ray diffraction
PGM	**:** Platinum group metals
PLC	**:** Programmable logic controller
PWM	**:** Pulse width modulation
SAC	**:** Spent auto catalyst
XRF	**:** X-ray fluorescence

SYMBOLS

$\mathbf{T_m}$	**:** Melting temperature
$\mathbf{T_g}$	**:** Glass transition temperature
B	**:** Basicity
$\mathbf{r_c}$	**:** Radius of cation
$\mathbf{r_a}$	**:** Radius of anion
P	**:** Attraction or repulsion force
Q	**:** Electrical charge
a	**:** Atomic distance, inverse maximum fraction
K	**:** Interacting forces
K	**:** Coefficient of heat transfer ($W.m^2$)
K	**:** Kelvin
$\mathbf{Z_c}$	**:** Valence of a cation
$\mathbf{Z_c}$	**:** Valence of a anion
e	**:** Elementary charge
F	**:** Field Strength
ν	**:** Settling rate
$\boldsymbol{\rho_{metal}}$	**:** Density of a metal (kg/cm^3)
$\boldsymbol{\rho_{slag}}$	**:** Density of a slag (kg/cm^3)
$\Delta\boldsymbol{\rho}$	**:** Density difference
ρ	**:** Resistivity of graphite electrode ($\Omega.mm^2.m^{-1}$)
d	**:** Diameter of a droplet (m)
d	**:** Diameter of an electrode
g	**:** Gravity constant (m/s^2)
η	**:** Viscosity (Pa.s)
$\boldsymbol{\eta^o}$	**:** Viscosity without solid particles
n	**:** Geometrical shape constant
R	**:** Critical radius
γ	**:** Surface tension (N/m)
I	**:** Current (μA, mA, A, kA)
$\mathbf{I_{arc}}$	**:** Arc current
V	**:** Voltage (μV, mV, V, kV)
$\mathbf{V_{arc}}$	**:** Arc voltage
ΔV	**:** Voltage drop
$\mathbf{L_{arc}}$	**:** Arc distance
k	**:** Boltzmann constant
m	**:** Mass of particles
v	**:** Velocity
x	**:** Distance
E	**:** Electric field
v	**:** Velocity
x	**:** Distance
E	**:** Electric field

v **:** Velocity
x **:** Distance
E **:** Electric field

LIST OF TABLES

LIST OF FIGURES

LAB-SCALE DC ELECTRIC ARC FURNACE DESIGN AND THERMODYNAMIC SLAG OPTIMIZATION FOR METAL RECOVERY FROM SLAG PHASE

SUMMARY

Entrapment of metals in slag phase cause a drastic economical loss in various metallurgical slags due to inefficient metal/slag seperation. Copper slags, display a substantial copper (Cu) presence, ranging between 0.5% and 3.7%, comparable to or exceeding the copper content observed in standard copper ores. Moreover, treatment of secondary sources such as printed circuit boards (PCBs), spent auto-catalytic converters (SACs) and low grade jewelry waastes could be treated by the very same principles. E-wastes are found to contain notable concentrations of copper (Cu) and gold (Au), with levels approximately 13–26 times and 35–50 times higher, respectively, than those typically present in the minerals conventionally employed for the extraction of these metals. In SACs, Platinum group metals (PGMs) such as Pt, Pd, Rh is typically present in larger quantities with concentrations ranges spanning from 100-3000 ppm, 5-1700 ppm and 5-240 ppm respectively while PGM ore deposits contains only 2.8 to 0.7 ppm. Low-grade jewelry waste including floor sweepings, polishing dusts, rags and tissues, emerge as significant reservoirs of gold (Au) and silver (Ag), exhibiting concentrations as high as 848 ppm Au and 7812 ppm Ag was reported. In contrast, the gold concentration in conventional gold ores typically falls within the range of 1 to 15 ppm. This highlights the potential value in extracting precious metals from seemingly less significant waste materials, underscoring the importance of exploring diverse sources for resource recovery.

In this study, a pyrometallurgical process and slag optimization methodology were designed for the efficient separation of metals from slag phase. Particularly, a direct current (DC) electric arc furnace (EAF) capable of reaching a temperature of 1800 °C in a short time was designed and constructed for the recovery of metals trapped in various sources such as Cu flash furnace slag, jewelry waste slag and spent auto-catalyst (SAC) containing platinum group metals (PGMs). Slag optimization studies were made through thermodynamic calculations and thermal investigations.

During the construction of the DC-EAF involved several critical components: A hearth design was devised through heat transfer calculations, ensuring the inner crucible's resilience to temperatures reaching a maximum of 1800 °C. Consequently, the inner hearth was crafted using high-purity Al_2O_3 castable, while the outer hearth was constructed using MgO bricks and Al_2O_3-ZrO cement. Heat transfer calculations indicated that the outer steel casing could potentially attain temperatures as high as 425 °C, where the incorporation of a cooling system for both electrodes and the steel

casing is required. To facilitate electrode motion during smelting, an electrode motion system featuring two step-motors connected in two axes was designed. Continuous arc formation during melting is essential to reach high temperatures as quickly as possible. However, due to the variation in electrical resistance of the melting environment with temperature, presence of solid and liquid phases, arc formation was controlled using an automation system that could adjust both voltage and electrode-electrode distance (or arc length). Continuous arc formation was investigated using current-time graphs and it was observed that the arc consistently formed except for brief short circuits. A power source incorporating an AC to DC rectifier and an electrode system was constructed to provide the requisite energy for arc smelting. Additionally, a mechanical tilting system was implemented to facilitate the straightforward tapping of the system.

The recovery of metals from slag phase involved optimizing the melting of slags since the homogeneous melting of all phases in the slag and its connection to viscosity were crucial. Therefore, the optimization of the slags to be melted was carried out through thermodynamic calculations and thermal behavior measurements. Initially, slag samples were characterized using X-ray diffraction (XRD) and X-ray fluorescence (XRF). The SAC phase contained high amounts of SiO_2, Al_2O_3 and MgO thus, located in the cordierite phase region. Cu flash furnace slag contained fayalite slag with FeO.SiO, while jewelry waste slag was rich in PbO due to the cupellation process used to collect the metal phase in lead.

In this study, binary phase diagrams of SiO_2, Al_2O_3, MgO and FeO, along with flux additions (CaO, Na_2O, B_2O_3), were systematically examined, revealing crucial insights into low-temperature phases, eutectics and low liquidus temperatures. The phase-equilibrium diagrams for the spent auto-catalyst (SAC) phase, augmented with Na_2O, CaO and B_2O_3 flux additions, were meticulously calculated. Notably, SAC phase demonstrated a melting point of 1453 °C and Na_2O addition resulted in the formation of $NaAlO_2$, $NaAlSiO_4$ and Na_2SiO_3, at 0.75 SiO_2/Na_2O+SiO_2 and (0.05 $Al_2O_3/Na_2O+Al_2O_3$ achieving an overall slag formation temperature of 1100 °C. The introduction of B_2O_3 at a ratio of 0.5 MgO/B_2O_3+MgO led to the creation of $Mg_3B_2O_6$ at an exceptionally low temperature of approximately 500 °C. Moreover, a mere 30% (w/w) B_2O_3 addition remarkably decreased the slag temperature to 900 °C, demonstrating the pronounced influence of B_2O_3 on reducing viscosity through its interaction with the SiO_2-Al_2O_3 network. Conversely, the incorporation of CaO ((0.6 $SiO_2/CaO+SiO_2$) and (0.354 $Al_2O_3/CaO+Al_2O_3$)) formed calcium-based silicate and aluminates, with specific phases transforming at temperatures of 1350 °C, 1200 °C, 1180 °C and 1150 °C. Gibbs free energy calculations elucidated the feasibility of reactions between fluxes and slag phases. When the formation energy of CaB_2O_4 surpasses that of calcium silicate and aluminates, it does not contribute to a reduction in the melting point of these oxides. On the other hand, Na_2O together with B_2O_3 prove useful as the $Na_6Si_8O_{19}$, $NaAlO_2$ target phases forms rather than sodium borate species resulting a decrease in melting temperature and lowered viscosity. The study further explored the thermal behavior using Differential Scanning Calorimetry (DSC), revealing endothermic peaks corresponding to slag formation temperatures and viscosity calculations demonstrated that B_2O_3 induced a drastic reduction in slag viscosity, even at low concentrations (5%-10%), reaching as low as 125 Pa.s. This comprehensive investigation provides valuable quantitative insights into the thermodynamic and kinetic aspects of the studied pyrometallurgical process, paving the way for enhanced efficiency in metal recovery from diverse sources.

When determined flux additions from thermodynamic calculations, (0.75 SiO_2/Na_2O+SiO_2, 0.05 $Al_2O_3/Na_2O+Al_2O_3$, 0.5MgO/MgO+B_2O_3 and 30% B_2O_3) into SAC and (0.22 FeO/FeO+Na2O and 30% B_2O_3) into Cu flash furnace slag and only 30% B_2O_3 added to jewelry slag, recovery efficiencies were determined. The results indicated attainment of <%92.94 Pt and Pd recovery for SAC, %83.16 Cu recovery for Cu flash furnace slag and %98.48 Ag and %84.77 Cu recovery for jewelry slag.

This research strives to pioneer the creation of a comprehensive approach for extracting metals from slag phases. It integrates high-temperature smelting and introduces a slag optimization methodology to reduce melting temperature and viscosity. The objective is to incorporate a minimal flux volume, a critical element for improving recovery efficiency and streamlining the industrial adoption of the process.

CÜRUF FAZINDAN METAL GERİ KAZANIMI İÇİN LABORATUVAR ÖLÇEKLİ DC ELEKTRİK ARK FIRINI TASARIMI VE TERMODİNAMİK CÜRUF OPTİMİZASYONU

ÖZET

Metallerin cüruf fazında hapsedilmesi, verimsiz metal/cüruf ayrımı nedeniyle çeşitli metalurjik cüruflarda ciddi ekonomik kayıplara neden olur. Bu duruma örnek olarak, bakır cürufları %0,5 ila %3,7 arasında bakır içermekte ve standart bakır cevherlerinden daha fazladır. Ayrıca, baskı-devre kartları (PCB'ler), kullanılmış oto-katalitik konvertörler (SAC'ler) ve düşük metal içerikli mücevher atıkları gibi ikincil kaynakların işlenmesi de aynı prensiplerle metal kazanım prosesleri gerçekleştirilebilir. PCB'ler, kayda değer konsantrasyonlarda bakır (Cu) ve altın (Au) içermekte ve bu metallerin cevherlerindeki oranlarına kıyasla sırasıyla 13-26 kat ve 35-50 kat daha yüksektir. SAC içerisindeki seramik yapıda bulunan Pt, Pd ve Rh platin grubu metallerinin konsantrasyonu sırasıyla 100-3000 ppm, 5-1700 ppm ve 5-240 ppm aralığındadır ve bu miktarlar cevher yataklarında yalnızca 0,7 ila 2,8 ppm'dir. Düşük metal içerikli mücevherat atıkları (ramat) farklı kaynaklarda ciddi oranda, 848ppm Au ve 7812 ppm Ag içerdiği rapor edilmiştir.

Bu çalışmada, verimli metal/cüruf seperasyonu için pirometalurjik proses tasarımı yapılmıştır. Cu flash fırını cürufu, mücevher atığı cürufu ve PGM içeren kullanılmış oto-katalitik konvertör gibi çeşitli kaynaklarda cüruf fazında bulunan metallerin geri kazanımına yönelik olarak 1800 °C sıcaklığa kısa zamanda çıkabilen, bir doğru akım (DC) elektrik ark ocak (EAF) tasarlanmış ve inşa edilmiştir. Bununla birlikte termodinamik hesaplamalar ve termal incelemeler yoluyla cüruf optimizasyon çalışmaları yapılmıştır.

DC-EAF'nin ocak bölümü maksimum 1800 °C'ye ulaşan sıcaklıklara dayanacak şekilde ısı transfer hesaplamalarıyla gereken refrakter malzeme seçilmi yapılmıştır. İç ocak yüksek saflıkta Al_2O_3 dökülebilir malzeme kullanılarak inşa edilirken, dış ocak MgO tuğlalar ve Al_2O_3-ZrO çimentosu kullanılarak inşa edilmiştir. Isı transferi hesaplamaları, dış çelik mahfazanın potansiyel olarak 425 °C'ye kadar yüksek sıcaklıklara ulaşabileceğini gösterdi; bu da hem elektrotlar hem de çelik mahfaza için bir soğutma sistemi gerektiğini göstermiştir. Ergitme sırasında elektrot hareketini, iki eksene bağlı iki step motor içeren bir elektrot hareket sistemi tasarlanarak inşa edilmiştir. Ergitme esnasında sürekli ark oluşumu yüksek sıcaklıklara mümkün olduğunca çabuk ulaşmak açısından oldukça önemlidir. Ancak ergime ortamının elektriksel direncinin sıcaklığa bağlı olarak değişmesi, sürekli arkı kesmekte ve bu sebeple de hem voltajı hem de elektrot-elektrot mesafesini (veya ark uzunluğunu) ayarlayabilen bir otomasyon sistemi kullanılarak kontrol edilmiştir.

Sürekli ark oluşumu akım-zaman grafikleri kullanılarak incelenmiş ve saniyelik kesilmeler dışında dışında arkın tutarlı bir şekilde oluştuğu gözlenmiştir. Ark ergitme için gerekli enerjiyi sağlamak amacıyla AC'den DC'ye doğrultucu ve elektrot sistemini içeren bir güç kaynağı kullanılmıştır. Ek olarak, ergitme sonrası döküm sürecini kolaylaştırmak için için mekanik bir yatırma sistemi inşa edilmiştir.
Cüruf fazından metallerin geri kazanımı, cüruf içerisindeki tüm fazların homojen olarak ergimesi ve düşük viskoziteye sahip olmasına bağlı olduğundan yapılan çalışmadaki cüruf optimizasyonu bu parametreler üzerinden yapılmıştır. Cürufların optimizasyon çalışmaları, termodinamik hesaplamalar ve termal davranış ölçümleri yoluyla gerçekleştirilmiştir. Başlangıçta cüruf örnekleri X-ışını kırınımı (XRD) ve X-ışını floresansı (XRF) kullanılarak karakterize edildi. SAC fazı yüksek miktarda SiO_2, Al_2O_3 ve MgO içerdiğinden kordiyerit fazı bölgesinde yer almaktadır. Cu flaş fırın cürufu, FeO.SiO ile fayalit cürufu içerirken mücevher atığı cürufu, kurşundaki metal fazı toplamak için kullanılan kupelasyon işlemi nedeniyle PbO açısından zengin olduğu gözlemlenmiştir.
Bu çalışmada, SiO_2, Al_2O_3, MgO ve FeO'nun ikili faz diyagramları ile flaks ilaveleri (CaO, Na_2O, B_2O_3) sistematik olarak incelenmiş ve düşük sıcaklık fazları, ötektikler ve düşük sıvılaşma sıcaklıkları hakkında önemli bilgiler ortaya çıkarılmıştır. Na_2O, CaO ve B_2O_3 flaks ilaveleriyle harcanmış oto-katalizör (SAC) fazının faz dengesi diyagramları hesaplanmıştır. SAC fazı 1453 °C'da bir ergime noktası gösterirken, Na_2O ilavesiyle (0.75 SiO_2/Na_2O+SiO_2 ve 0.05 $Al_2O_3/Na_2O+Al_2O_3$) yapı içerisindeki SiO_2 ve Al_2O_3 fazları $NaAlO_2$, $NaAlSiO_4$ ve Na_2SiO_3 oluşturmuş, ve sistemin ergime sıcaklığı 1100 °düşmüştür. SAC komposizyonuna B_2O_3'ün 0,5 MgO/B_2O_3+MgO oranında eklenmesi, yaklaşık 500 °C gibi son derece düşük bir sıcaklıkta $Mg_3B_2O_6$'nın oluşmasına yol açmıştır. Üstelik yalnızca %30 (ağırlık/ağırlık) B_2O_3 ilavesi, cüruf sıcaklığını dikkate değer ölçüde 900 °C'ye düşürmesine rağmen yapı içerisindeki SiO_2-Al_2O_3 fazları 1400 °C'lere kadar cüruf fazına katılmamıştır. SAC kompozisyonuna CaO'nun ((0,6 $SiO_2/CaO+SiO_2$) ve (0,354 $Al_2O_3/CaO+Al_2O_3$)) dahil edilmesi, SiO_2 ve Al_2O_3 fazların dönüşmesiyle kalsiyum bazlı silikat ve alüminatlar oluşturmuş, ve bu fazlar 1100-1350 °C arası ergime sıcaklıklarına sahip olduğu gözlemlenmiştir. Gibbs serbest enerji hesaplamaları, flaks ve SAC'da bulunan fazlar arasındaki reaksiyonların oluşma enerjilerini incelemek için kullanılmıştır. Çalışmada ayrıca diferansiyel taramalı kalorimetre (DSC) kullanılarak SAC'ın termal davranış araştırılmıştır, cüruf oluşum sıcaklıklarına karşılık gelen endotermik tepe noktaları ortaya çıkarılmış ve viskozite hesaplamalarıyla B_2O_3'ün düşük konsantrasyonlarda bile (%5-%10) cüruf viskozitesinde 125 Pa.s'ye kadar ciddi bir azalmaya neden olduğunu anlaşılmıştır. Bu kapsamlı araştırma, çalışılan pirometalurjik sürecin termodinamik ve kinetik yönlerine ilişkin değerli bilgiler sağlayarak, ergitme işlemi esnasında cüruf bileşimi hazırlanmasında kullanılması hedeflenmiştir.
Termodinamik hesaplamalardanla flux ilaveleri belirlendiğinde SAC'ye (0,75 SiO_2/Na_2O+SiO_2, 0,05 $Al_2O_3/Na_2O+Al_2O_3$, 0,5$MgO/MgO+B_2O_3$ ve %30 B_2O_3) ve (0,22 $FeO/FeO+Na_2O$ ve %30 B_2O_3)) Cu flaş fırın cürufuna eklenmiş ve mücevher cürufuna sadece %30 B_2O_3 eklenmiş ve geri kazanım verimleri belirlenmiştir. Yapılan çalışmalarda SAC için <%92.94 Pt ve Pd, Cu flaş fırın cürufu için %83.16 Cu ve atık mücevher cürufu için %98.48 Ag ve %84.77 Cu geri kazanım verimine ulaşıldığını göstermiştir.
Bu araştırma, metallerin cüruf fazından geri kazanımına yönelik kapsamlı bir yaklaşımın oluşturulmasına öncülük etmeyi amaçlamaktadır. Yüksek sıcaklığı kısa sürede çıkabilecek potansiyele sahip DC-EAF tasarımının yanında düşük ergime

sıcaklığı ve viskoziteyi azaltmak için cüruf optimizasyon metodolojisini anlatan çalışmada, geri kazanım verimliliğini artırmak ve sürecin endüstriyel olarak boyutlara entegrasyonunu kolaytırmak adına en uygun ve düşük hacimdeki flaks miktarları belirlenmiştir.

xxx

1. INTRODUCTION

Earth's crust is mainly composed of oxygen (O), silicon (Si), aluminum (Al), iron (Fe) and calcium (Ca). When thermochemical stabilities of oxides have taken into account, it's not surprising that these oxides are present in at least one stage of all metallurgical processes. In metal production, such oxides must be separated from the metal melt in the phase called "slag" [1].

Slags have crucial function for production of metals from ores which are summarized as:

- Seperation of unwanted oxides and other impurities from melt
- Preventing the contamination originating from furnace atmosphere and combustion byproducts of the fuel
- Providing thermal insulation for the melt
- Regulating the supply of refining agents into the melt during the metal smelting.

To achieve these functions, slags must show certain properties such as having a low melting point (T_m) and immiscibility so that a homogenous slag melt can be achieved on the top of the molten metal. Slags are formed by the presence of oxide impurities from the gangue, along with the addition of "fluxes." Fluxes, are generally metal compounds (oxides, phosphates, flourides and chlorides) and their purpose is to lower the liquidus temperature, enabling the homogeneous separation between the metal phase and the slag phase due to the density difference [2].

Composition of the slag varies by the metallurgical processes where, it commonly composed of SiO_2, FeO, CaO and Al_2O_3. The formation of slag is an endothermic reaction that results in an increase in volume, leading to a higher heat input. Increase in slag volume also decreases the production yield, as it increases the entrapment of metals. Additionally, viscosity and wettability of slag directly influences the diffusion of reaction in the slag-

metal interface. Therefore, in order to create a slag, all of such must be taken into consideration [2], [3].

1.1. Slag Chemistry

In metallurgical industry, conventional approach is to adjust the "basicity" of the slag to achieve desired T_m while increasing refractory life and improving productivity of the process [4]. In 1947, Flood and Forland explained the behaviour of acid and basic oxides in terms of exchanging O^{2-} ions (Eq 1.1), presenting the key reactions as;

$$[..Si - O^{2-} - Si - O^{2-}..] + 2O^{2-} \rightarrow 2[Si - O^{2-}] + 2[Si - O^{2-}] \quad (1.1)$$

In Eq 1.1, a basic oxide donates an oxygen ion (O^{2-}) that cause Si-O bridges to break down. Basic oxides are the ones which donate O^{2-} ions to the slag (Eq 1.2), e.g. CaO, FeO, MgO, Cu_2O, Na_2O, K_2O, that ionise as follows:

$$CaO \rightarrow Ca^{2+} + O^{2-} \quad (1.2)$$

Acidic oxides which accept O^{2-} ions, e.g. SiO_2 , P_2O_5, Al_2O_3 and which produce complex cations by reaction with the oxygen anions (Eq. 1.3-1.4), i.e.

$$SiO_2 + 2O^{2-} \rightarrow SiO_4^{2-} \quad (1.3)$$

$$P_2O_5 + 2O^{2-} \rightarrow 2PO_4^{3-} \quad (1.4)$$

$$Al_2O_3 + 3O^{2-} \rightarrow 2AlO_3^{3-} \quad (1.5)$$

Therefore, one molecule of SiO_2 is balanced by the neutralization of two molecules of basic oxide ($2O^{2-}$ ions), whereas one molecule of Al_2O_3 and P_2O_5 each require the neutralization of three molecules of basic oxide, as observed in (Eq. 1.6 – Eq. 1.8). When the composition of the slag consists of these proportions of basic and acidic oxides, it lacks both basic and acidic properties and is referred to as a neutral slag.

$$SiO_2 + 2CaO \rightarrow Ca_2SiO_4 \text{or } CaO.SiO_2 \text{ or } 2Ca^{2+} + SiO_4^{4-} \quad (1.6)$$

$$P_2O_5 + 3CaO \rightarrow Ca_3(PO_4)_2 \text{ or } 3CaO.P_2O_5 \text{ or } 2Ca^{2+} + 2PO_4^{3-} \quad (1.7)$$

$$Al_2O_3 + 3CaO \rightarrow Ca_3(AlO_3)_2 + 3CaO.Al_2O_3 \text{ or } 3Ca^{2+} + 2AlO_3^{3-} \quad (1.8)$$

A slag became basic when it contains a higher proportion of basic oxides than the neutral ortho-compound composition, resulting in an excess of O^{2-} ions. On the other hand, an acidic slag holds more acidic oxides than the neutral ortho-compound composition, leading to an excess of SiO_2, P_2O_5, or Al_2O_3. A typical basic slag composition consists of three moles of CaO and one mole of SiO_2 (more CaO than seen in Eq. 1.6) while an acidic slag composition involves one mole of CaO for each volume of SiO_2 (less CaO than seen in Eq 1.6) [2], [4], [5]. Several formula exist for assessing a slag's basicity (as seen in Eq. 1.9 and Eq. 1.10), with the most precise being the basicity ratio (B), defined as [2], [6]:

$$B = \frac{\text{mole}_{CaO} + \text{mole}_{MgO}}{\text{mole}_{SiO_2} + \text{mole}_{Al_2O_3}} \quad (1.9)$$

$$B = \frac{\text{moles of basic oxide} - 3 * \text{mole}_{Al_2O_3}}{2 * \text{mole}_{SiO_2}} \quad (1.10)$$

When the basicity ratio (B) is equal to 1, a neutral slag composition is attained. B<1 indicates an acidic slag, while B>1 signifies a basic slag. Typically, an acidic slag tends to be more viscous than a basic slag. For simplicity, the CaO/SiO_2 ratio used to define viscosity in this context [2].

Despite basicity approach is commonly used in current metallurgical industry, it does not present a detailed slag behaviour. However, it could offer a slight perspective to create a slag. To accomplish this objective, it is essential to examine the reactions between metal oxide phases, the formation of the slag and the behavior of slag throughout thermodynamic and glass formation studies.

1.1.1. Structure of Slags

Slags could either behave as a glass or a ceramic, according to its dominant bond type (e.g. covalently bonded or ionically bonded) which is determined by its composition as seen in Figure 1.1. In this work, formation of slags were explained by the chemistry of glasses.

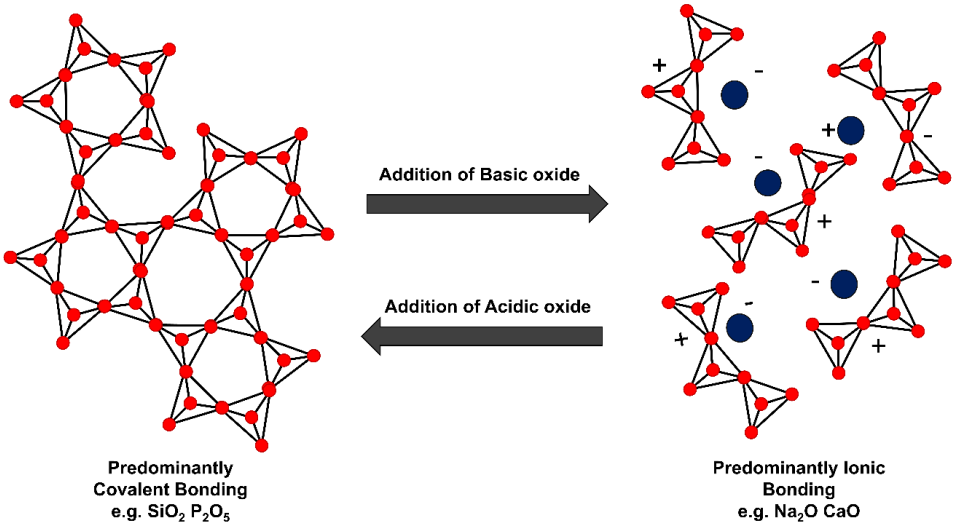

Figure 1.1: Illustration of gradual transition from the predominantly covalent bonding to ionic bonding by either acidic or basic oxide addition (Illustration is modified from ref [2].)

Si is the most common component in many slags where rapid cooling of it results in the formation of a glass structure without long-range crystalline order. Thus, molecules only interact in short-range forces [2]. To investigate this local arrangement of molecule networks, Zachariasen and Warren explained the glass structure where glass forming element oxides are connected in 3-D disordered infinite network. This network is formed by metals having low coordination number in oxide network. In the case of SiO_2 glasses, network is composed of SiO_4 tetrahedrons or in case of B_2O_3, BO_3 triangles [5].

Based on the Zachariasen-Warren network theory, certain principles apply to the creation of basic 3-dimensional networks at lower levels. This pertains to the glass formation of uncomplicated compounds like SiO_2, B_2O_3, P_2O5, GeO_2, As_2S_3 and BeF_2 [5];

- A glass is more likely to be formed by an oxide or compound, if it readily creates polyhedral groups as the smallest building units.
- Polyhedra should not have more than one corner in common
- In simple glasses, anions (e.g., O^{2-}, S^{2-}, F^-) should not connect with more than two central atoms of a polyhedron. Consequently, anions act as bridges between two polyhedra.
- The polyhedra should have fewer than six corners.

- A polyhedron must connect with neighboring polyhedra through at least three corners.

When introducing large cations like Na_2O or CaO into glasses, such as SiO_2 networks, bridges within the structure are disrupted. The accompanying oxygen (or other anions like S^{2-}, F^-) from the large cation occupies the vacant position at the free end of the separated tetrahedron. Simultaneously, the large cation is housed in the expanded cavity resulting from the network break at that location. As illustrated in Figure 1.1, The theory assumes chain network is severed by the placement of large cations in the cavities of the network which increases the ionic character of the system. Zachariasen categorized the cations in a glass in the following manner [5]:

- Elements that contribute to the formation of networks, like Si, B, P, Ge, As, Be typically have a coordination number ranging from 3 to 4.
- Intermediates have the capacity to either enhance the network (with a coordination number of 4) or break it (with coordination numbers ranging from 6 to 8), yet they lack the ability to independently form a glass.
- Network-modifying elements, such as Na, K, Ca, Ba, etc., generally exhibit coordination numbers of approximately 6.

According to theory, the presence of large cations leads to the disruption of bridges in the slag network. This in turn, enhances the mobility of the building units, making it easier for network-modifiers to contribute to the reduction of viscosity and the melting range. Additionally, it results in an increase in electrical conductivity [5].

Relation of ionic size to bond type and therefore glass formation was first explain by Goldschimdt. To form a glass, the radius of cation ($\mathbf{r_c}$) to the radius of anion ($\mathbf{r_a}$) must be in the range between 0.2 to 0.4. This criterion is satisfied in instances such as SiO_2 , B_2O_3, P_2O_5, etc. Dietzel was the pioneer in expanding Goldschmidt's ideas, going beyond the size and polarizability of ions to include their charges. This extension enabled the exploration of the effects of interaction forces between cations and anions in the solidification of a melt. By utilizing the basic physics equation for attraction (or repulsion) (**P**) between electrical

charges (**Q**) at a distance (**a**), Dietzel offered a more inclusive comprehension of the solidification process. (Eq. 1.12).

$$P = \frac{Q.Q}{a^2} \tag{1.12}$$

$$K = \frac{Z_c Z_a e^2}{(r_c + r_a)} \tag{1.13}$$

In this context, (Eq. 1.13) **K** represents, the interacting forces; $\mathbf{Z_c}$ and $\mathbf{Z_a}$ are the valencies of the cation and anion, respectively; **e** denotes the elementary charge; $\mathbf{r_c}$ and $\mathbf{r_a}$ stand for the radii of the cation and anion, where $a = r_c + r_a$. Dietzel introduced the term "field strength" (**F**) in these considerations (Eq. 1.14).

$$F = \frac{Z_c}{a^2} \tag{1.14}$$

Table 1.1 highlights how Zachariasen's categorization of ions into network-formers, network-modifiers and intermediates aligns directly with their field strength. In the case of network-modifiers, the field strength (F) typically falls within the range of 0.1 to 0.4. For network-formers, F is notably higher, ranging from 1.4 to 2, almost an order of magnitude larger. Intermediates on the other hand, exhibit an F value approximately between 0.5 to 1.0.

Table 1.1: Classification of cations according the their field strength (Dietzel's approach) [5].

Element	Valence [Z]	Ionic Radius r in [Å]	Coordination number [CN]	Ionic distance for oxides a in [Å]	Field Strength at distance of O^2 ions [Z/a^2]	Function in the glass structure*
Na	1	0.98	6	2.30	0.19	Network modifier
Ca	2	1.06	8	2.48	0.33	Network modifier
Fe	2	0.83	6	2.15	0.43	Network modifier
Mg	2	0.78	6	2.10	0.45	Intermediate
Al	3	0.57	6	1.89	0.84	Intermediate
Fe	3	0.67	6	1.99	0.76	Intermediate
B	4	0.20	4	1.50	1.34	Network former
Si	4	0.39	4	1.60	1.57	Network former
P	5	0.34	4	1.55	1.57	Network former

*Network modifier is a term that explains the behavior of the element in the network structure. Modifier means that the molecule network is destroyed while "former" means creation and preservation of the network.

From this section it can be concluded that the viscosity and melting temperature of slag can be controlled by adjusting and optimizing the slag composition, by breaking the molecule networks in the slag phase. It is important to mention that the adjusting basicity in a slag is meaningful since the addition of CaO, Na_2O and FeO behave as a network modifier.

1.2.Metal and Slag Seperation

In pyrometallurgical extraction, it is frequent to lose some of metal content to slag phase. In iron and steel production, remnant of Fe or ferroalloys may find their way to slag. The blast furnace slag which is enriched with Fe, can be reintegrated into the steel plant as a secondary source of iron and as a pre-melted flux. Additionally, basic oxygen furnace (BOF) slag holds potential for recycling into the sinter and blast furnace operations, facilitating the recovery of Fe and Mn. Cu slags typically contain a higher metal concentration than ferrous slags, even than the Cu levels found in the sulfide ores. The enrichment of Cu in these slags is often attributed to the entrapment of matte in the slag, a phenomenon that becomes particularly common when the slag melt is quenched. This process restricts the gravity separation of metal-bearing sulfide droplets. Reprocessing Cu slags is a routine practice in certain extraction processes, typically involving comminution in a mill, followed by flotation to recover residual sulfides. These recovered sulfides are then reintroduced into the smelter [7]. Figure 1.2 is a radar chart depicting the possible elements into the slag, gas or metal phase during a given process. This figure serves as an illustration of the metal trapment observed in slags during the pyrometallurgical processing of natural ores. The figure suggests that several valuable metals can be extracted from the slag phase. For instance, Cu-Ag-Au-Pt-Pd-Rh can be obtained from Cu-convertor slags, Cu-Ag-Au-Pt-Pd from BF-Pb slags and Cu-Ag-Au-Pt-Pd from Zn-Pb ISP, indicating the potential for recovering these metals from these specific slag sources [7].

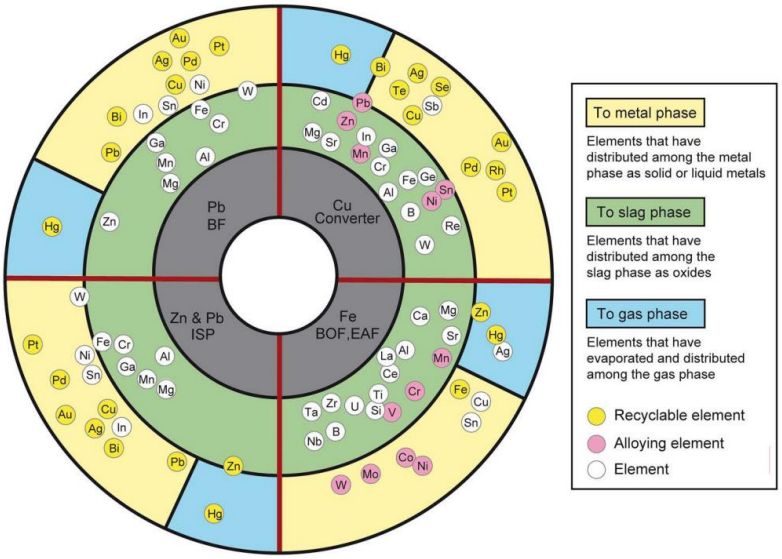

Figure 1.2: An element radar chart illustrates the distributions of elements among phases during pyrometallurgical reprocessing [7].

Slag primarily contains metal oxides from gangue ores which must be seperated from the system in order to remove impurities from the molten metal or matte. In typical pyrometallurgical processes, the slag floats on top of the molten metal due to density difference and in most cases, it is eventually tapped from the furnace. Settling, often a final step before tapping, is a common practice in many pyrometallurgical processes, facilitating the separation of slag and matte/metal as seen in Figure 1.3. This illustration depicts a standard smelting process. In the first step, the furnace is charged with metal-bearing ores and reductants. In the second step, heat is applied to the furnace, causing the metal to melt, while the oxide part remains in a solid state within the melt. To achieve a homogeneous slag, fluxes are introduced to obtain low-melting solid oxide phases. Despite this, certain industrial processes such as Cu smelters, Pb reduction smelting furnaces, ferrochrome smelters, among others, still experience losses of metal-rich droplets in slags due to inadequate phase separation. These losses pose a significant challenge in metal extraction and recycling industries and their mitigation involves optimizing phase separation.

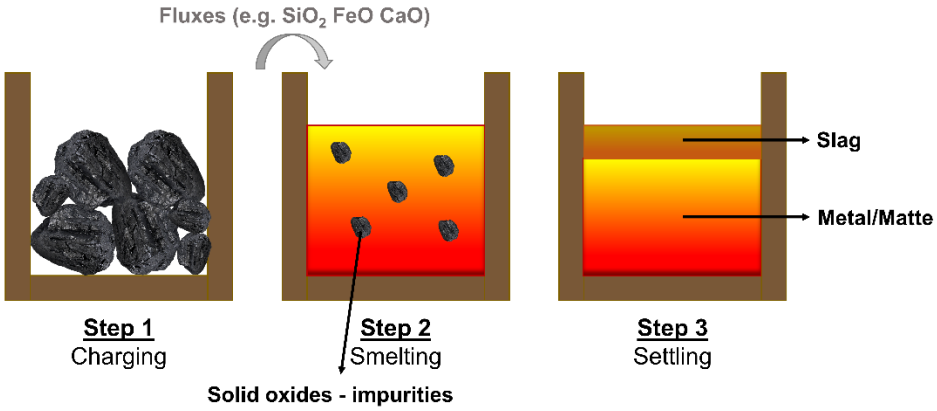

Figure 1.3: An illustration depicts metal/slag seperation in a typical smelting process.

Despite there are variety of sources for metal entrapment such as dissolution of metal in slags, physically entrapped matte or metal can account for up to 65-80% of total metal loss. Thus process parameters such as furnace operation, slag viscosity, fluid motion in the slag, settling time, SO_2 generation and the presence of solid particles directly influence the efficiency of matte-slag seperation [8].

Loss of metal or matte droplets in slag phase are associated with inadequate settling of droplets. These physical losses involve particles with diverse sizes, ranging from several millimeters to a few micrometers. In general, the settling of droplets of a certain phase in another phase can be described by Stokes' equation (Eq. 1.15) [9]:

$$\nu = \frac{(\rho_m - \rho_s) g d^2}{18\eta} \tag{1.15}$$

The settling rate (**ν**) can be calculated using Stokes' equation, where [9]:

ρmetal and **ρslag** represent the density of the metal droplets and the slag, respectively (kg/m³)

d is the diameter of the droplet (m)

g is the gravity constant (m/s²)

η is the viscosity of the slag (Pa·s)

This equation is suitable under conditions of laminar flow, which is marked by a low Reynolds number. It is particularly applicable to rigid spheres or drops/bubbles and remains

approximately valid for liquid droplets rising or settling in an immiscible medium with a stationary surface.

Nevertheless, in industrial processes where larger metal droplets are present in slags, these droplets may not be inherently rigid and might not retain a spherical shape. When the viscosity of the droplets is notably lower than the viscosity of the slag, internal tensions within the droplets emerge. In such cases, Stokes' equation needs to be corrected and the Hadamard-Rybczinski equation (Eq. 1.16) becomes more appropriate [8]. In the context of the Hadamard-Rybczinski equation:

$$v = \frac{gr^2 \Delta p}{3\eta} \tag{1.16}$$

Δρ denotes the density difference between the sphere and the fluid. Preliminary experiments have suggested that small drops with a diameter below approximately 0.01 cm exhibit behavior similar to rigid spheres and their velocity can be precisely described by Stokes' equation On the contrary, drops of a size that is adequately large conform to velocities described by the Hadamard-Rybczinski equation. Both the Stokes and Hadamard-Rybczinski equations underscore the significance of slag viscosity, the size of sinking droplets and the density difference [8], [10]. For lowering the metal losses in slag phase, the following considerations should be pursued;

• To enhance the density differential, the density of iron silicate slags diminishes with rising silica content, decreasing temperature and elevated levels of basic oxides. Typically, FeO tends to increase slag density, whereas SiO_2 and CaO exert the opposite influence.

• Increase droplet size to its maximum by promoting coagulation or facilitating the growth of smaller droplets. This method enhances the surface-to-volume ratio, influencing the interfacial energy between the droplets and the slag. Additionally, droplets may undergo growth or reduction due to oxidation or reduction reactions.

• Within the liquids with high viscosity, small particles may be trapped for prolonged durations [8], [11]. It's important to highlight that the viscosity of the slag is influenced by the fraction of solid particles, a phenomenon referred to as the "slurry effect," elucidated by the Einstein-Roscoe model equation (Eq. 1.17) where:

$$\eta = \eta^0(1 - af)^{-n} \quad (1.17)$$

η is the viscosity of the molten slag with dispersed particles (Pa·s),

η^0 is the viscosity of molten slag without dispersed particles (Pa·s),

f is the ratio of solid particles in the slag

a is the inverse maximum ratio of solid particles

n is geometrical shape constant, assumed to be 2.5 for spherical particles [12].

The efficiency of the sedimentation process is significantly influenced by the settling rate. A study examining the impact of settling time on metal losses verified the anticipated outcome, revealing a decrease in Cu content in the slag layer with longer settling times. In the Tamano flash smelting furnace, the average settling time for the slag spans 4 to 5 hours, during which particles with a diameter larger than 0.13 to 0.15 mm settle. It is noteworthy that extended sedimentation times have a limited impact on the recovery of smaller particles [8].

The traditional assumption was that phase separations in slag-metal systems were solely driven by the buoyancy effect arising from the substantial density contrast between the alloy and the slag. However in another study, this hypothesis was questioned through an exploration of varying gravity conditions on products synthesized by combustion phenomena. Diverse gravity conditions ranging from 10^{-5} G to 1.7 G were applied to study various systems. The examination uncovered that mechanisms influenced by surface energy could also play a pivotal role in the settling process [49]. Additionally, adhesion of copper matte and metal droplets on the surface of the slag due to surface tension described by Fagerlund [13]. Poggi *et al.* established the critical radius of a droplet capable of resting on the interface by equating the upward force resulting from surface tension with the weight of the particle (or drop) as seen in Eq. 1.18 [11]. It is anticipated that larger drops will sink through the slag/metal or matte surfce, while smaller drops will float.

$$R = \left(\frac{2 * \gamma_{slag}}{\frac{3 * \rho_{particle} * g}{4}}\right)^{1/2} \quad (1.18)$$

R is the critical radius of the sphere (m),

ρ is the density (kg/m^3),

g is the gravity constant (m/s^2),

γ is the surface tension (N/m).

Up to this point, main parameters effecting the metal loss in slag phase is described; Larger metal droplets exhibit a higher tendency to sink and a longer settling time facilitates a higher yield. Slag viscosity decreases the metal/slag separation, having critical impact on metal entrapment.

Moreover, extensive exploration in the literature has focused on the chemical dissolution of metals in slags. Initially, the prevailing assumption was that copper (and other metals) dissolves in slags in the form of oxides, commonly termed 'oxidic' dissolution. The concentration of Cu_2O in a slag is associated with the thermodynamic conditions of the furnace and can be reduced by managing the furnace according to established metal-matte-slag-gas relationships. The solubility of Cu_2O decreases at lower temperatures as depicted in Figure 1.4A. Additionally, at higher pO_2 Cu solubility increases as seen in Figure 1.4B.

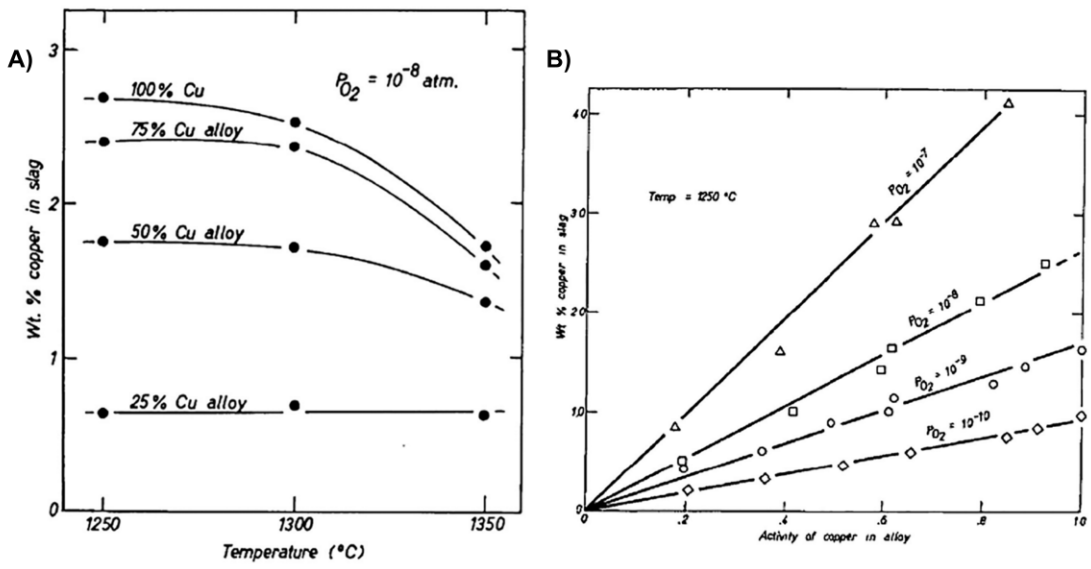

Figure 1.4: The impact of temperature on the solubility of copper in slags at a constant oxygen partial pressure (PO_2) of 10^{-8} atm (A).[a] Impact of tempertaure and PO_2, on Cu solubility in slags (B) [14], [15]

[a]In Figure 1.4A, Cu alloy refers to Cu-Au alloy which was investigated in the cited article and the figure shows an increase copper loss in the slag phase with increasing Cu content. Cu-Au alloy was not mentioned in the text to avoid confusion.

The explaination of metal dissolution were explained by Richardson and Billington, for sulphur-free slags [16]. They stated that Cu can only dissolve after oxidation where no solid Cu in present. However, when the slag coexists with a sulphidic matte phase, the iron silicate slag can dissolve Cu. The ionic theory gave rise to the concepts of 'oxidic' and 'sulphidic' dissolutions of copper to explain this phenomenon [17], [18], [19]. Nagamori's experiments showed Cu solubility far exceeding that attributed to oxidic loss in previous studies on sulphur-free slags. This increased solubility was linked to the presence of S in the slag, leading to the development of the concept of “sulphidic dissolution”.

In line with the molecular or ionic theory of slag, a sulfur ion (S ion) may dissolve in the slag, displacing a free oxygen ion (O ion) initially associated with an iron ion. Subsequently, this sulfur ion may have a tendency to replace some of its coordinating iron ions with copper, in accordance with the activity of copper in the matte. The overall dissolved copper in the slag arises from the combined effects of oxidic and sulphidic dissolution and the proportions of each depend on the composition of the slag. Sulphidic

dissolution is typically notable for matte grades up to around 60% Cu, while at lower copper percentages, oxidic dissolution becomes the predominant mechanism as illustrated by Figure 1.5 [1], [17].

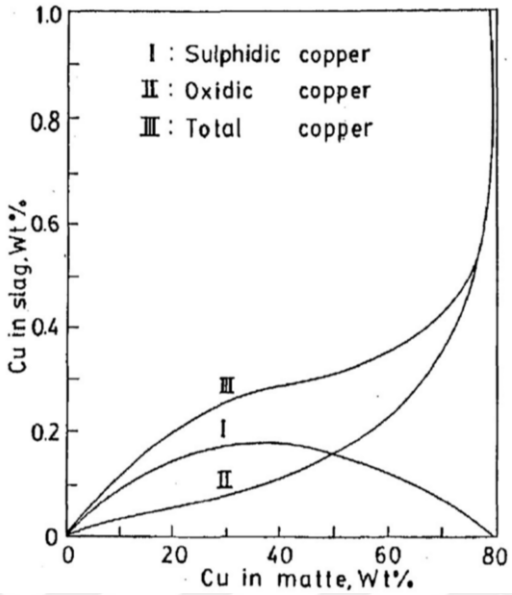

Figure 1.5: Diagram illustrating the calculated values of oxidic, sulphidic and total dissolved copper in commercial reverberatory slag [8].

Nagamori's original data [19] demonstrated a decrease in copper content in slags with an increase in sulfur content. Sridhar et al. [20] highlighted that typical investigations utilize a gas-matte equilibrium to regulate the oxygen potential, mirroring plant practices. Nagamori employed metallic iron in equilibrium with 0-55 wt% Cu mattes to control the oxygen potential, leading to a lower oxygen potential than in copper smelting, thereby increasing sulfur solubility. For Cu grades of mattes exceeding 55 wt%, Nagamori utilized copper metal in contact with matte to stabilize the oxygen potential, resulting in an oxygen potential close enough to that in copper smelting. In the composition range exceeding 55%, Nagamori observed that copper loss is exclusively oxidic.

The findings by Sridhar *et al.* [20] suggest that copper losses in slags can be accounted by the oxidation of copper under varying oxygen potentials encountered during the production of distinct matte grades. Additionally Sridhar *et al.* suggests, the presence of copper sulphide is deemed highly improbable, given that the affinity of sulfur for iron is greater

than for copper. This higher affinity increases the likelihood of sulphide ions being in proximity to iron ions rather than copper ions.

In many slags, the dissolution of metals generally depends on the very same parameters that decreases the physical entrapment of metals. The silica content also plays a role in Cu losses, with optimal copper preservation occurring at approximately 35% SiO_2. This decline is attributed to the dominance of slag-matte interfacial tension over melt viscosity. The addition of SiO_2 boosts viscosity and diminishes surface tension. Silica content influences magnetite formation (with the SiO_2/FeO ratio being crucial) [3]. Various constituents in the slag also play a role in influencing the Cu loss. An increase in FeO by the reduction FeS_2, results in decreased viscosity, lowered density and support magnetite reduction, thereby enhancing Cu solubility in the slag through the formation of SO_2 bubbles [8].

1.3.Typical Ferrous and Non-Ferrous Slags

Slags can be categorized based on their metallurgical processes as in Figure 1.6; Ferrous slags are created as side products during various iron and steel smelting and refining procedures. Non-ferrous slags are generated in the process of extracting non-ferrous metals commonly from natural sulfide ores. These slags cover various types, such as Cu slag, Zn smelting slag, Sn slag, Ni converter slag, SiMn slag, V slag. A typical non-ferrous metal from sulfide ores involves three essential steps; concentration, roasting and smelting; ultimately resulting in the production of non-ferrous slags [21]. In addition to ferrous and non-ferrous slags, various slags find application in metallurgical and recycling industries. One such example is salt slag, which originates from the secondary aluminum industry. During the smelting process of recycled aluminum scraps in a reverberatory or rotary furnace, fluxes containing NaCl and KCl are introduced into the molten bath. Incineration slag, formed from the incineration of municipal solid waste (MSW). After burning,

remaining solid is terms as bottom ash whereas dust collected from air filters is called fly ash.

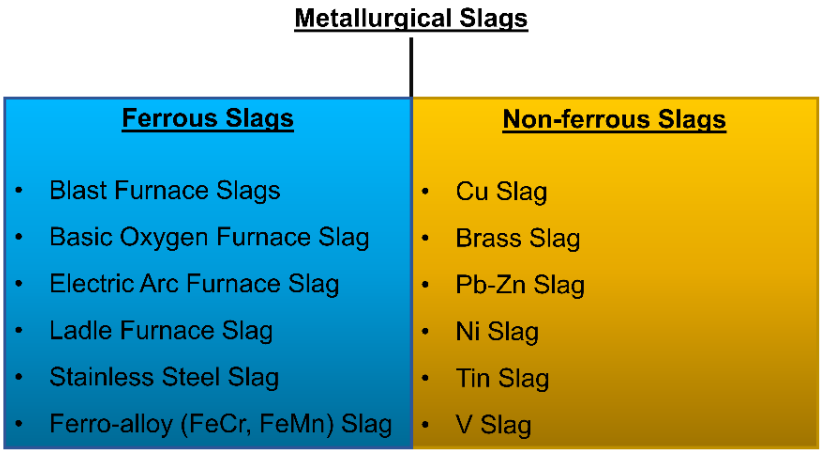

Figure 1.6: Classification of typical metallurgical slags.

1.3.1. Ferrous Slags

According to the World Steel Association (2012), over 400 million tonnes of iron and steel slags are generated annually. The primary categories of slags resulting from these unit processes can be broadly classified into two groups: Blast furnace slag (iron slag) and steelmaking slags. Steelmaking slags can be further categorized based on the specific unit process from which they originate, namely, BOF (Basic Oxygen Furnace), EAF (Electric Arc Furnace) and ladle furnace slags [22]. Slag composition of ferrous processes were given in $CaO/MgO\text{-}SiO_2\text{-}Al_2O_3/FeO_x/CrO_x$ slag system.

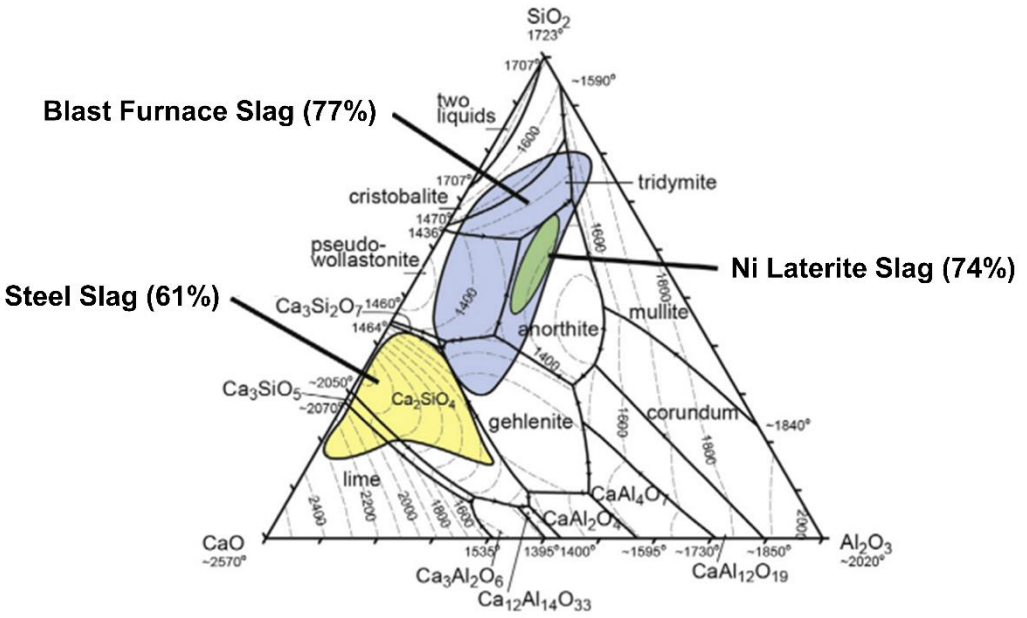

Figure 1.7: Common slag composition used in iron production (blast furnace slag), steel manufacturing (steel slag) [22].

As seen in Figure 1.7, All ferrous slags generally in the region close to SiO_2-CaO line, due to high SiO_2 content which arises from the gaunge while CaO is introduced as a flux during the processes. Blast furnace slags is generated from Fe production through thermochemical reduction in the blast furnace. Numerous researchers have examined the standard chemical composition of slags in iron and steelmaking and their discoveries are summarized in Table 1.2 [22]. Blast furnace slags are part of the CaO–SiO_2–Al_2O_3–MgO system and may include minor components like MnO, FeO, Na_2O and K_2O among others. Generally, blast furnace slags exhibit liquidus temperatures ranging from 1350°C to 1400°C and a basicity ratio (CaO/SiO_2) typically falling between 1.2 and 1.3. The mineral composition of slow-cooled blast furnace slags contains crystallized Ca–Al–Mg silicates, particularly melilite ($Ca_2MgSi_2O_7$–$Ca_2Al_2SiO_7$) and merwinite ($Ca_3MgSi_2O_8$) [22].

Table 1.2: Typical blast furnace slag composition taken from various works [23-27].

Typical Composition [%]							Ref.
SiO_2	**CaO**	**Al_2O_3**	**MgO**	**MnO**	**FeO**	**S**	
36–45	33–42	10–16	3–16	≤2.0	-	-	[23]
34.7	35.5	9.9	14.6	-	0.6	1.6	[24]
35–42	35–40	8–15	8–9	0.3–1.0	0.5–0.8	0.7–1.5	[25]

35–42	33–38	10–15	7–12	≤1.0	≤1.0	1–1.5	[26]
41.7	33.8	13.4	7.4	0.3	0.5	0.8	[27]

In the BOF process, the blast furnace's hot metal, steel scrap and fluxes in the form of lime and dolomite are introduced into the furnace. Impurities dissolved in the liquid metal, including Si, P, Mn and S undergo oxidation and combine with the lime and dolomite fluxes, resulting in the formation of BOF slag. Because of the impurities present in the crude liquid steel and the refining needs in the BOF process, the slags typically exhibit a high basicity ratio ($2.4 < CaO/SiO_2 < 4.0$). They also have a higher FeO content due to oxidizing conditions and specific blow regimes (as seen in Table 1.3). In comparison to blast furnace slags, their chemical composition tends to be more variable.

Table 1.3: Typical basic oxygen furnace slags taken from various works.

Typical Composition [%]							Ref.
CaO	**SiO_2**	**Al_2O_3**	**MgO**	**FeO**	**Fe_2O_3**	**MnO**	
45-60	10-15	1-5	3-13	7-20	3-9	2-6	[28]
39.4	11.97	2.16	9.69	30.23	-	2.74	[29]
47.7	13.25	3.04	6.37	-	24.36	2.64	[30]
47.9	12.2	1.2	0.8	26.3	-	0.3	[31]
45	11.1	1.9	9.6	10.7	10.9	3.1	[32]
30-55	8-20	1-6	5-15	10-35	-	2-8	[33]
42-55	12-18	≤3	≤8	-	-	≤5	[23]

The increased FeO content in basic oxygen furnace (BOF) slag stems from the challenge of recovering some iron in hot metal as steel. Primary components of BOF slag include FeO, CaO, SiO_2, Al_2O_3 and MgO. In the case of electric arc furnace (EAF) slag, formed during the recycling of steel scraps, its chemical composition is significantly influenced by the chemical properties of the recycled steel scraps. Major components of EAF slag consist of FeO, CaO, SiO_2, Al_2O_3 and MgO with trace elements such as MnO, P_2O_5 and SO_3 present in minimal quantities. In certain instances, the FeO content in EAF slags is reported to be very low, i.e., <3% [21].

The EAF process depends on solid steel scrap, fluxes, slag formers and ferroalloy charges, which are melted by passing an electric current through the charge mixture using graphite electrodes. In situations where EAF serves both smelting and refining functions, oxygen and other oxy-gas mixtures are injected into the molten steel through specially designed

lances. This is done to oxidize the impurities dissolved in the crude liquid steel. In such cases, the oxidation products react with fluxes and slag formers, ultimately forming the final EAF slag [21]. Composition of EAF slag is given in Table 1.4.

Table 1.4: Composition of EAF slag taken from various works.

Typical Composition [%]								Ref.
CaO	**SiO_2**	**Al_2O_3**	**MgO**	**FeO**	**Fe_2O_3**	**MnO**	**Cr_2O_3**	
30-50	11-20	8-13	8-22	5-6	-	5-10	-	[28]
45.5	32.2	5.2	3.3	1	-	2	0.05	[32]
46.9	33.5	6.22	1.07	0.36	1.56	2.6	2.92	[34]
39-45	24.32	8.15	1-6	-	-	0.4-2	29.2	[23]
25-40	10-17	4-15	-	-	-	≤6	≤3	[35]

During the ladle refining process, desulfurization agents (such as Mg, CaSi and CaC_2) and deoxidation agents (such as Si and Al) are introduced into the steel bath. The reaction products, including substances like CaS, $3CaO \cdot P_2O_5$, SiO_2 and Al_2O_3 either dissolve into or are absorbed by carefully engineered slag. The slag is eventually removed from the surface of the liquid steel. However, limited knowledge exists regarding the chemical composition of ladle furnace slags thus, it tends to vary based on the quality of the steel produced. Various alloys are injected into the ladle furnace to achieve steel of the desired quality. According to some experiments, ladle slag is anticipated to have a very low FeO content (<10%) as indicated in Table 1.5, while concentrations of CaO and Al_2O_3 are higher for ladle slags [21]. Argon oxygen decarburization (AOD) slag also exhibits a similar composition with lower SiO_2 content.

Table 1.5: Slag compositions from ladle furnace and AOD furnace taken from various resources.

Typical Composition [%]									Ref
Slag type	**CaO**	**SiO_2**	**Al_2O_3**	**MgO**	**FeO**	**Fe_2O_3**	**MnO**	**TiO_2**	**Cr_2O_3**	
Ladle	55	15	12.5	7.5	-	2.1	0.36	0.33	0.01	[35]
Ladle	42.5	14.2	22.9	12.6	0.5	1.1	0.2	840 ppm	2700 ppm	[32]
AOD	54.10	26.5	4.91	6.3	1.18	0.63	1.02	0.98	1.83	[34]
AOD	47.6	31.24	1.66	3.65	-	-	1.6	0.22	5.07	[36]
AOD	45.5	26.3	9.7	7.3	-	-	2.1	-	6.3	[36]
AOD	46-48	26-31	1.7-10	3.7-7.3	-	-	1.4-2.1	0.2-1.1	3.6-6.3	[37]

Charge chrome slag is a byproduct of submerged arc furnaces, consisting mainly of MgO, SiO_2, Al_2O_3, Cr_2O_3, CaO and FeO. Recently, charge chrome slag has attracted considerable attention due to its high concentration of the Cr. There is a growing emphasis on the treatment and recovery of chromium owing to environmental concerns. In contrast to steel slag (BOF, EAF), the Fe and SiO_2 percentage of charge chrome slag are roughly similar, while CaO is much lower. On the other hand, MgO, Al_2O_3 and Cr contents are significantly higher in charge chrome slag compared to steel slags. [21]. Due to the elevated chromium content in charge chrome slag, considerable emphasis has been placed on its treatment and the recuperation of chromium from it. It is approximated that a charge chrome plant generates nearly equal quantities of slag and metals [36].

1.3.2. Non-ferrous Slags

Non-ferrous slags are formed during the production of non-ferrous metals such as Cu, Zn, Pb, Ni, Sn and etc. These metals are commonly found in sulfide ore thus, it is necessary to remove its sulphur content as SO_2 gas. During smelting two immiscible phases occur; a heavier sulfide phase (Cu_2S) containing copper namely, "*the matte*" and the oxide phase, "*the slag*" according to equilibrium of (Eq. 1.19) [38];

$$Cu_2O + FeS \leftrightarrows Cu_2S + FeO \quad (1.19)$$

$$2FeO + SiO_2 \leftrightarrows Fe_2SiO_4 \quad (1.20)$$

$$2Fe_2O_3 + 3Fe_3O_4 + 2FeS \rightarrow 17FeO + 2SO_{2(g)} \quad (1.21)$$

SiO_2 as flux is added to mixture to lower liquidus temperature of FeO thus forming (Fe_2SiO_4) fayalite (Eq. 1.20), a ferrous silicate that constitutes main component of the slag. Fe_2SiO_4 and silicate glasses emerge as the most identified silicate phases in non-ferrous slags, representing volumetrically significant compounds in the materials. Besides Fe_2SiO_4, olivine-group phases with compositions corresponding to kirschsteinite ($CaFe_2$+SiO_4) and forsterite (Mg_2SiO_4) are also frequently observed. Liquid FeS, further reduce to Fe_2O_3 to FeO then again, added to $Fe_2(SiO_4)$ (fayalite) phase as seen in (Eq. 1.21) [38].

Following the separation of matte and slag, the matte or molten metal phase enters the converter. In the conversion process, the melt undergoes additional desulfurization and extra impurities are eliminated by introducing oxygen and fluxes like lime, iron ore or basic slag. The generation of slag takes place throughout the smelting and converting processes, potentially extending to additional refining steps. Certain portions of the slag may be recycled to the smelter due to their high metal content. [21].

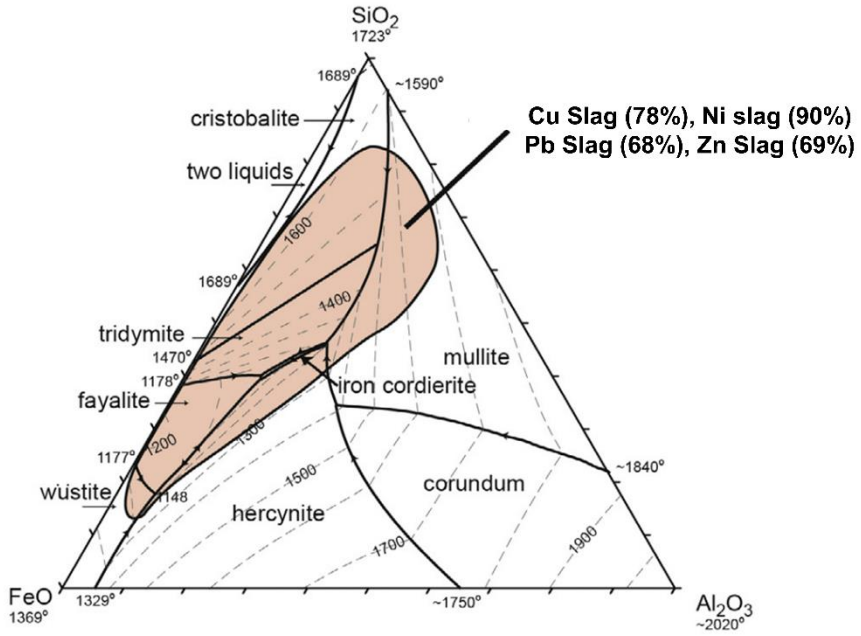

Figure 1.8: Ternary phase diagram of Al_2O_3-SiO_2-FeO. Colored field represents the common slag composition for each slag type [39].

Common phase percentages of non-ferrous slags are depicted on FeO - SiO_2 - Al_2O_3 ternary phase diagram (Figure 1.8) [39]. The chemical composition of Cu slags exhibits variations, depending upon parameters such as ore type, flux additions and additives utilized in the pyrometallurgical process as outlined in Table 1.6. Generally, the primary components in copper slags are iron (Fe) and silicon dioxide (SiO_2), each accounting for approximately 25–50% of the composition [36]. Almost all copper slags exhibit a significant presence of copper (Cu), ranging from 0.5% to 3.7%, which is comparable to or even surpasses the copper content in copper ores. Depending on their origins, certain slags may also contain recoverable levels of Co and/or Ni [40]. They also contain minor percentages of Al_2O_3 and CaO. Other oxides as MgO, K_2O and S are present in much smaller amounts [41]. Other

metals such as Cr and Ni only present in much lower quantities, usually not exceeding 0.1%.

Table 1.6: Chemical composition of copper slags from the literature [36].

Elements[a] [%]	Slag 1 [42]	Slag 2[b] [43]	Slag 3 [44]	Slag 4 [45]	Slag 5 [36]	Slag 6 [46]
Cu	2.60	0.58	3.70	1.22	2.75-3.3	0.6–3.2
Co	0.36	0.21	0.25	-	0.5–0.7	-
Ni	0.045	0.57	-	-	0.9–1.2	-
Zn	0.425	-	0.44	-	-	-
Fe	52.0	38.6	49.99	32.24	45–48	32.7–37.3
SiO_2	-	Si: 17.40	22.45	-	24–26	32.5–37.3
Al_2O_3	-	Al: 2.51	1.14	-	-	2.4–4.0
CaO	-	Ca: 1.11	-	-	-	1.8–7.5
MgO	-	Mg: 1.65	-	-	-	1.6–4.0
S	4.90	0.93	1.56	-	-	0.5–1.0

[a]In this graph, the reported percentages were given in the table to avoid confusion.

[b]for Slag 2, metallic percentages of Si, Al, Ca, Mg were given in the table.

Antimony (Sb) ore also found primarily as jamesonite ($4PbS \cdot FeS \cdot 3Sb_2S_3$). Where typical non-ferrous metal production route is followed during its extaction. Sb slags contains Zn, Pb, Sb and possibly other metal sulfides as seen in Table 1.7.

Table 1.7: Antimony smelting slag taken from literature [47].

Composition [%w/w]	Pb	Zn	Sb	S	Fe	SiO_2	CaO
	1.24	6.58	1.31	1.54	20.59	22.25	19.09

Slag composition from Pb and Zn production are summarized in Table 1.8. It can be seen that the slags belong to $FeO(Fe_2O_3)$-CaO-SiO_2 system containing high amount of Pb and Zn with basicity 0.36-0.4 ($B=CaO\%/(CaO\% + SiO_2\%)$).

Table 1.8: Pb blast furnace and Imperial smelting process (ISP) slag composition [48].

Kivcet Slag [%w/w]	Pb	Zn	Sb	Cu	Fe^{2+}	Fe^{3+}	SiO_2	CaO	Al_2O_3
	15.8	10.2	0.33	0.37	17.4	6.7	21.8	13	1.6

Pb BF Slag [%w/w]	Pb	Zn	Cu	S	Fe	SiO_2	CaO	MgO	Al_2O_3
	2.2	6	0.3	1.54	24	27	15	5	3
ISP Slag [%w/w]	**PbO**	**ZnO**	**S**	**FeO**	**SiO_2**	**Al_2O_3**			
	0.6-1	5-10	1-3	30-42	16-21	5-10			

When low-grade nickel matte is subjected to blowing in a converter for the production of high-grade nickel matte, a substantial amount of slag is generated. From Table 1.9 Ni converter slag contains numerous valuable elements, including Ni, Co and Cu. The FeO_x–SiO_2 slag system comprises the primary component of nickel converter slag, where various metals are present either in a dissolved state or as inclusions. Nickel primarily exists in the sulfide form (Ni_3S_2), with some of it being dissolved in fayalite in the oxide form. Cobalt is predominantly distributed in the silicate as oxides (CoO), while nearly all copper is dispersed in the slag in the sulfide form (Cu_2S).

Table 1.9: Chemical composition of nickel converter slag [wt.%] [49].

Element	Fe	Ni	Co	Cu	S	Fe_2O_3	SiO_2	CaO	MgO	Al_2O_3
Composition [%]	43.2	3.5	0.6	0.9	1.5	3.06	29.20	0.11	0.83	0.48

Nickel ore may undergo processing concurrently with copper ores throughout concentration, roasting and smelting. The resultant copper and nickel matte is subjected to roasting and then either reduced with carbon or leached with acid to separate the copper and nickel. Subsequent refining processes are applied to purify the metals. PbS concentrates undergo roasting and are subsequently reduced in a blast furnace using carbon as a fuel source, along with CaO and FeO as fluxes. Furthermore, additional impurities are eliminated in a reverberatory furnace through selective oxidations. Following these steps, silver is separated using the Parkes process [21].

1.4.Recovery of Metals from Waste Sources Using Metal/Slag Seperation

While the slag phase holds the potential for recovering various metals, it is also possible to to retrieve such metals from secondary wastes with the very same pyrometallurgical procedures. In some cases, the concentrations of these metals in secondary wastes can even exceed those found in primary ores. From them, variety of recovery routes utilizing

metal/slag seperation have been developed due to their complex structure. Despite hydrometallurgical routes were used generally in small or lab scale.

As of 2016, global gold supply from mining amounted to approximately 4570 tons, with gold production through mining activities reaching 3236 tons. The remaining 1334 tons of gold were sourced from electronic waste, scrap jewelry, gold in teeth, bullion and jewelry waste. Given the high value of precious metals like gold and silver, their particulate forms hold significant importance for companies and workshops [50].

Low grade wastes such as floor sweepings, polishing dusts, rags and tissues are an important source of Au and Ag where 848 ppm and 7812 ppm recovery was reported [51]. Whereas, Au concentration in common gold ores ranges varies between 1 to 15 ppm [52].

E-wastes, particularly printed circuit boards (PCBs) that are arising from all electrical equipment is also an important secondary source since it includes, Au, Ag, Cu, PGMs, Sn, Zn, Ni, Pb and many other critical metals [53].

E-wastes, indeed contains significant quantities of copper (Cu) and gold (Au), approximately 13–26 times and 35–50 times higher, respectively, compared to the minerals typically used for extracting these metals. In a report it was mention that if all mobile phones discarded in China in 2008 had been recycled, it could have resulted in the recovery of 1,250 tons of Cu, 13 tons of Ag, 3 tons of Au and 2 tons of Pd. This recovery would have had a market value of around $105 million [54].

Additionally, substantial environmental benefits could have been achieved, particularly in terms of greenhouse gas emissions. The study suggests that mining one ton of gold, platinum, or palladium typically results in the emission of approximately 17.000, 10.000, or 14.000 tons of carbon dioxide (CO_2), respectively [55].

Decreasing tenors of PGM containing ores increases the importance of recovery of PGMs. As an example, in Bushveld complex, South Africa average tenor of PGM deposits were decreased from 2.8 g/t to 0.7 – 1.4 g/t. Thus rapid change in the PGM prices becomes and itch for primary PGM producers [56]. Utilizing secondary sources is a preferable option compared to primary production. This is because secondary sources offer higher concentrations of PGMs and require much less energy - up to 70-100 times less - while

yielding higher recovery rate. Furthermore, using secondary sources helps to minimize the environmental impact associated with mining. All in all, exploiting secondary sources is a more advantageous and sustainable method of obtaining PGMs than relying solely on primary production [57]. Thus, its also crucial for reducing the environmental impact of mining and refining precious metals and to promoting the circular economy by recovering valuable materials from waste streams [58].

1.4.1. Waste Printed Circuit Boards (PCBs)

Electronic waste, or e-waste, possesses distinct chemical and physical characteristics that set it apart from conventional municipal or industrial waste. It comprises both valuable and hazardous materials, necessitating specialized handling and recycling methods to prevent environmental contamination and adverse impacts on human health. Through recycling, it becomes possible to recover reusable components and essential materials, with a particular emphasis on valuable resources such as Cu and Au, Ag and Pd [59].

Waste electric and electrical equipments consist of many items; large and small household appliances, electronic items, accessories and even toys. During recycling, parts are dismantled and seperated from the waste equipment. Despite most part is eliminated, printed circuit boards (PCBs) integrated in the equipment holds the major concern due to metal valuable and toxic metal composition and thus its complex structure which creates diffulties during the recovery. The weight fraction of PCBs in relation to the total device varies, ranging from 2% for large electronic devices to 11% for laptop computers and up to 22% for mobile phones.

Table 1.10: A common average PCB content [%] [60].

PCB content	Composition [% w/w]
Non-metal	<70
Cu	16
Solder	4
Iron, ferrite	3
Ni	2
Ag	0.05
Au	0.03
Pd	0.01
Other (Bi-Sb-Ta)	<0.01

Typical composition of a PCB is given in Table 1.10, the composition of presently employed PCBs is categorized as glass fiber-reinforced epoxy resin (FR-4), commonly utilized in compact electronic devices, or paper laminated phenolic resin (FR-2) that comprises approximately 70% of the PCB. Laminated copper sheets are etched. Recycling poses a challenge due to the complex mixture of polymers (plastics), silicates (Si-based), non-ferrous and ferrous metals. As related to Table 1.10, It is widely acknowledged that the weight composition of WPCB typically includes approximately 30% metallic fraction and 70% non-metallic fraction [59], [60].

The concentrations of metals in Printed Circuit Boards (PCBs) are affected by various factors, including the source, type of board, manufacturer and production timeframe. Manufacturing techniques, specific board designs for devices and the use of various soldering technologies contribute to the wide range of compositions observed in PCBs. As seen in the Table 1.11, The metal fraction typically includes approximately 8-38% Fe, 10-20% Cu, 2-15% Al, 0.5-3% Pb, 0.05-0.5% Ni, 200-3000 ppm Ag, 20-500 ppm Au and 10-200 ppm Pd despite significantly deviates due based on the PCB type [61].

Table 1.11: Metal percentages of variety of E-wastes from literature. [55].

E-waste	Weight [%]					Weight [ppm]			Refs.
	Fe	Cu	Al	Pb	Ni	Ag	Au	Pd	
TV board scrap	28	10	10	1	0.3	280	20	10	[62]
PC board scrap	7	20	5	1.5	1	1000	250	110	[62]
Mobile Phone scrap	5	13	1	0.3	0.1	1380	350	210	[62]
Portable audio	23	21	1	0.14	0.03	150	10	4	[62]
DVD player	62	5	2	0.3	0.05	115	15	4	[62]
Calculator scrap	4	3	5	0.1	0.5	260	50	5	[62]
PC mainboard scrap	12	14.3	2.8	2.2	1.1	639	566	124	[63]
PCB scrap	4.5	10	7	1.2	0.85	280	110	-	[55]
TV scrap	-	3.4	1.2	0.2	0.038	20	<10	<10	[64]
Electronic scrap	8.3	8.5	0.71	3.15	2	29	12	-	[65]
PC scrap	20	7	14	6	0.85	189	16	3	[55]
Typical electronic scrap	8	20	2	2	2	2000	100	50	[55]
E-scrap sample 1	37.4	18.2	19	1.6	-	6	12	-	[66]
E-scrap sample 2	27.3	16.4	11	1.4	-	210	150	20	[66]
Printed circuit boards	5.3	26.8	1.9	-	0.47	3300	80	-	[67]
E-scrap	26.2	18.6	-	-	-	1800	220	30	[68]

E-waste mixture	36	4.1	4.9	0.29	1	-	-	-	[69]

In Figure 1.9, the PCB content (in grams per kilogram) of internet modems, computer motherboards and mobile phones is depicted. The "MIX" content originates from unknown sources. The copper (Cu) content is notably high, reaching almost 300 g/kg, as anticipated, along with other previously mentioned metals. The "MIX" fraction exhibits a significantly elevated lead (Pb) content, highlighting its potential hazard. Silver (Ag) and gold (Au) are also present in substantial amounts, with nearly 1.7 g/kg of PCB. Figure 1.10 also illustrates parts of desktop computer PCB content, revealing that memory modules concentrate the majority of gold (Au), while copper (Cu) is distributed across various parts of the board [59].

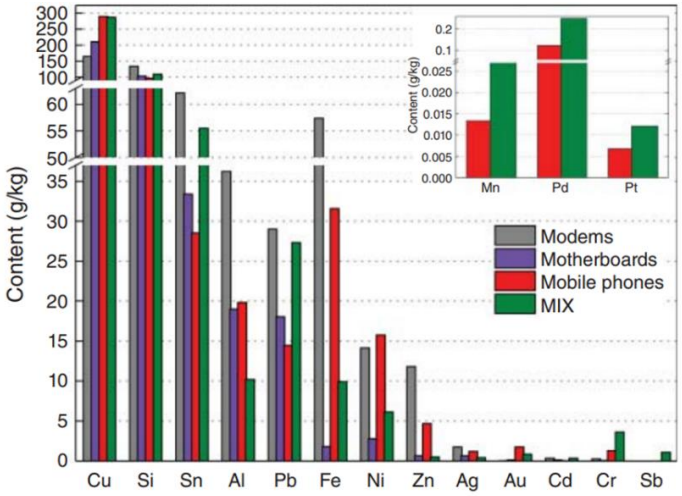

Figure 1.9: Metal composition of PCBs taken from different appliances [70].

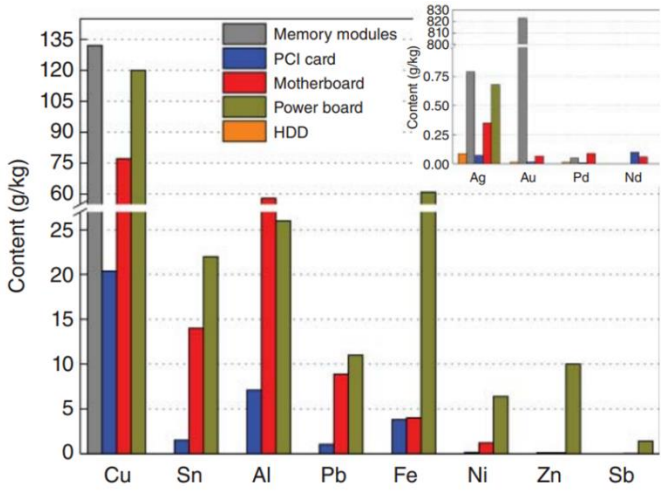

Figure 1.10: From variety of PCBs taken from desktop computer PCB [71].

Pyrometallurgical processing, covers techniques such as incineration, smelting in a plasma arc furnace or blast furnace, drossing, sintering, melting and high-temperature gas-phase reactions, has emerged as a conventional method for recovering non-ferrous metals and precious metals from electronic waste over the past two decades. In this process, crushed and enriched electronic scraps are subjected to combustion in a furnace or molten bath to eliminate plastics and the refractory oxides which creates the slag along with certain metal oxides [55].

In the industry variety of companies embraced a pyrometallurgical approach for metal recovery, as outlined in Table 1.12. In these processes, smelting is employed, utilizing modern equipment such as the Noranda reactor system, Outokumpu flash smelting and Mitsubishi continuous smelter. The treatment occurs at elevated temperatures, typically ranging from 600 to 1200 °C, within the combustion chamber. In this chamber, melting, various reactions and sintering processes take place [70].

Table 1.12: Conventional pyrometallurgical processes employed in the recycling of e-wastes [70].

Technique	Metal Recovered	Reference
Noranda Process	Au, Ag, Pd, Pt, Cu, Ni, Se, Te, Ni	[55]
Boliden Ronnskar Smelter	Cu, Ag, Au, Pd, Ni, Se, Zn, Pb	[55]
Umicore's precious metal refining process at Hoboken	PGMs, Cu-Au-Ag, Se, In, Te, Base metals,	[71]
Kaldo Process	Au, Ag	[72]
Outotec	Au, Ag, Cu, Pb, Zn, In, Ge	[70]

In Noranda process, The materials introduced into the reactor are submerged in a molten metal bath at a temperature of 1250 °C, agitated by a air blowing containing up to 39% oxygen. The cost of energy is minimized through the combustion of organic materials in the scraps. With the oxygen blowing, impurites such as Fe, Pb and Zn, into oxides that are then fixed in a silica-based slag. After cooling and milling, the slag is processed to retrieve additional metals before disposal. The copper matte, housing precious metals, is extracted and transferred to converters. Following an enhancement in the converters, the liquid blister copper undergoes refinement in anode furnaces and is cast into anodes with a purity of 99.1%. The remaining 0.9% contains precious metals such as Au, Ag, Pt and Pd alongside other recoverable metals like Se, Te and Ni. Subsequent electrorefining of the anodes facilitates the recovery of these marketable metals [55].

Boliden Ltd. Ronnskar Smelter in Sweden employs a pyrometallurgical route for metal recovery from e-waste where scraps can be introduced into the process at different stages based on their purities. High-copper-containing scrap is directly fed into the Converting process, while low-grade e-waste is directed to the Kaldo Furnace. [55], [72]

In the Kaldo reactor, a mixed feed containing e-wastes and Pb concentrates are introduced using a skip hoist. Oxygen, supplied through an oil-oxygen burner using an oxygen lance, facilitates combustion. A conventional gas handling system recovers thermal energy through a steam network. The Kaldo Furnace creates a copper alloy that contains Cu, Ag, Au, Pd, Ni, Se and Zn which is sent to copper convertor for recovery. Additional outputs such as Pb, Sb, In and Cd containing dusts are directed to other operations for metal recovery [72]. Despite the varieties in the procedures, general recovery is based on eliminating non-metal part of the PCBs which then subsequently directed to conventional copper production which is then seperated by either hydrometallurgy or electrowinning.

1.4.2. Au-Ag Containing Slags

Gold and silver find well-known use in jewelry production, constituting one of their main applications. During the manufacturing of jewelleries, wastes are produced during every

step of the process such as polishing wastes, floor sweeping wastes, handwashing waste and sewage wastes.

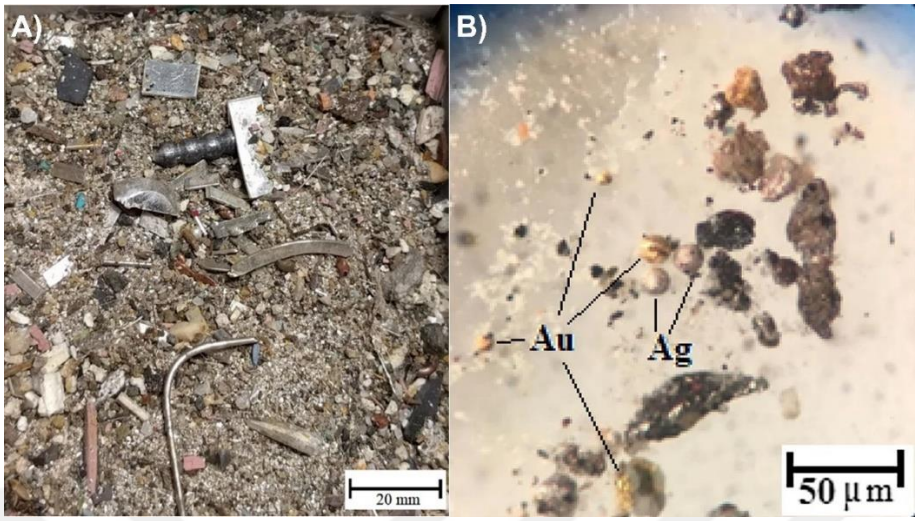

Figure 1.11: A photo of low grade jewellery floor sweeping (A). Au and Ag particles seen from an optical microscope (B) [50], [73].

Polishing waste comprises a mixture of plastic and metal bristles, abrasive paste and metal dust, the latter primarily consisting of gold alloys. Gold particles, combined with substantial amounts of waste dust, debris and larger-sized objects, are referred as floor sweepings waste and seen as in Figure 1.11. Handwashing waste, produced from operator and laboratory clothings thus, contain an organic matrix from which gold particles are separated. This waste also includes additional components, such as soap and even spent coffee powder, making its recovery a challenging process. Finally, small gold particles are ingested by jewelry operators and are subsequently discharged into sewage sludge through the body's natural processes. This waste stream also exhibits a high concentration of organic matrix and as of now, there is a lack of comprehensive studies on the recovery of metals from this particular source [50], [74]. In Table 1.13 variety of jewellery wastes and how much gold is contained within them is summarized.

Table 1.13: Common jewellery wastes and scraps along with corresponding gold contents [50].

Waste	Type of Waste	Gold Content [%]
Old jewelry	Solid	39-73

Bench Scrap	Solid	19-52
Sink trap settings	Slurry	6-8
Carpets and wood floors	Solid	0.1-9
Old crucibles	Solid	0.8-5
Polishing dusts and sweeps	Solid	0.5-5
Watchbands and gold-filled scraps	Solid	0.25-5
Emery papers, floor dirt, brushes	Solid	0.1-4

Scrap and wastes with a high gold content (>20%), including items like old pots, bench sweepings, sand from sandblasting machines, sink muds, polishing machine residue, carpets, door mats, old aprons, swabs, brooms, as well as consumed and expendable molds, are categorized as combustible and non-combustible. These materials are smelted in a graphite crucible using an appropriate flux material to eliminate impurities such as dirt, oxides and refractory abrasives. It is crucial for the viscosity to be low and the melt should be maintained at a high temperature for 30 min. Subsequently, the slag is separated from the cast bar [50].

Meanwhile, low grade wastes (less than 20%) compose of all the other above mentioned wastes. Schematical representation of processing low grade wastes is given in and seen as Figure 1.12. In a controlled environment, floor sweepings, rags and tissues undergo a slow 24-hour incineration process to prevent the escape of fine particles with the flue gas. The resulting ashes are magnetically seperated, milled, screened, sampled and combined with fluxes. Subsequently, the mixture is fluxed and smelted for 2–3 hours before pouring and casting, using the same method employed for high-grade materials. During the smelting, slag phase is produced and thus often further processed to recover remaining precious metals [75].

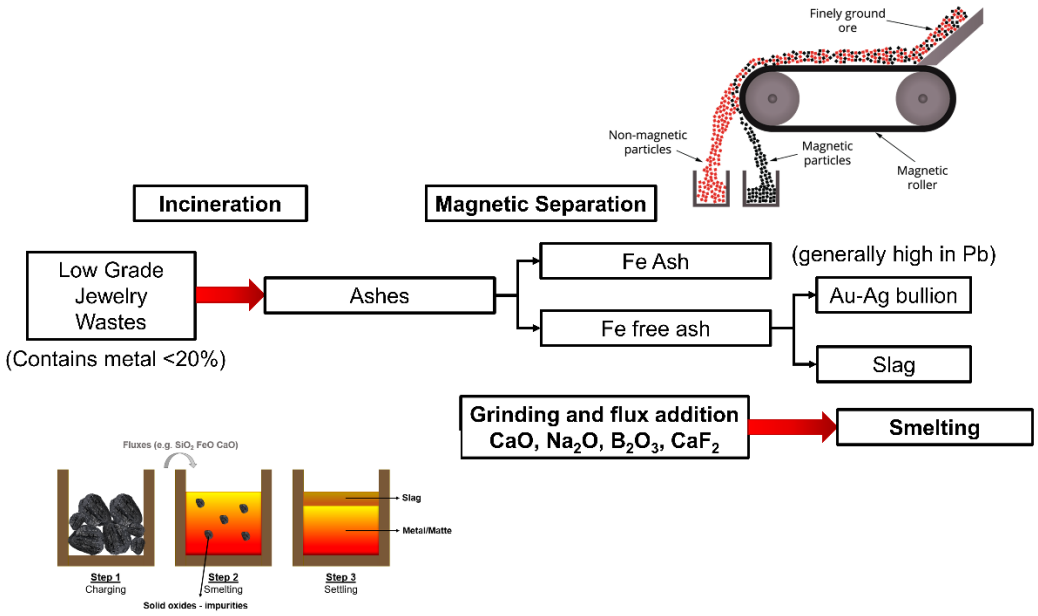

Figure 1.12: Schematical representation of Au and Ag containing low-grade jewelry wastes (modified from [75]).

Even after the recovery process, produced slag contains a part of Au and Ag particles trapped inside the slag phase as seen in Figure 1.13.

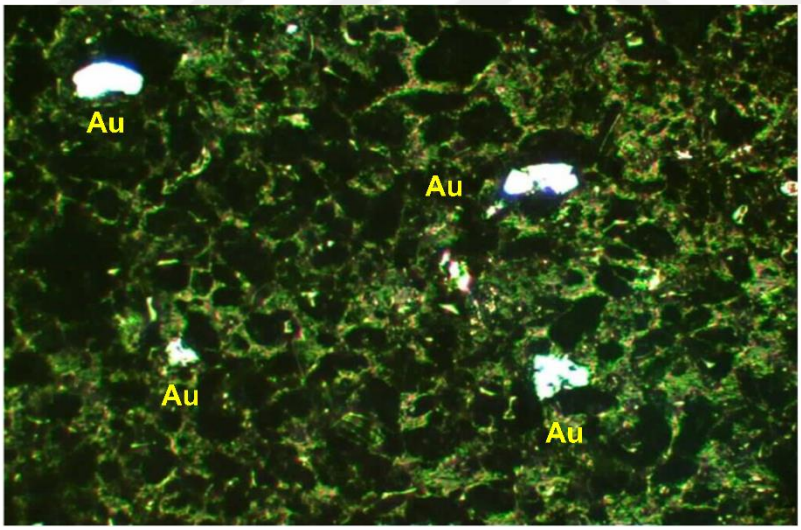

Figure 1.13: An microscope image of Au containing slag [75].

Composition of waste slag, produced during the recovery of Au and Ag from low grade jewelery wastes is given in Table 1.14. The slag contains typical non-ferrous constituents such as SiO_2, Al_2O_3 and FeO thus, primarily originate from polishing processes and dusts

from surfaces, as well as residues generated during polishing stages, abrasives and brush-like materials. Na_2O and B_2O_3 are added as fluxes.

Table 1.14: Composition of Au and Ag containing jewelry waste slag [75].

Element	Na	Si	Al	Ca	B	Fe	K	Cu	Zn	Ni	Ag	Au	O
[%][a]	17.95	8.78	8.01	5.63	5.09	4.83	1.86	0.32	0.29	0.02	5 ppm	33 ppm	47.2

[a]Given composition where retrieved from ONSA Gold Refinery, Turkey.

In both large and small-scale refineries, the cupellation process is predominantly utilized for recovery of metals from slag phase and widely accepted. This method involves mixing Pb with the Au containing metarial. The mixture is heated in open atmosphere in approximately 1000–1100 °C until the material dissolves in the Pb. During this process, all base metals and Pb undergo oxidation, forming a lead oxide slag. Consequently, two distinct phases emerge: slag and metal. The valuable components of the material become enriched in the molten phase, while impurities are discarded in the slag phase. The resulting gold-silver bullion, which may also contain platinum group metals (PGMs), requires further refining steps to obtain pure gold. One drawback of the pyrometallurgical process is the generation of hazardous gases and effluents, leading to atmospheric pollution, along with the loss of metallic values in the slag material [50].

1.4.3. Spent Auto Catalysts (SACs)

PGMs finds extensive use in automotive catalytic converters owing to its exceptional physicochemical attributes. These properties include high catalytic activity, resistance to chemical corrosion and thermal stability. The primary purpose is to reduce the emissions of NO_x, CO and C_xH_y from motor vehicles as shown in (Eq. 1.22 – Eq. 1.24) [76].

$$CO_{(g)} + O_{2(g)} \rightarrow CO_{2(g)} \tag{1.22}$$

$$C_xH_{y_{(g)}} + \left(x + \frac{y}{4}\right) O_{2(g)} \rightarrow xCO_{2(g)} + \frac{y}{2} H_2O_{(g)} \tag{1.23}$$

$$N_{2(g)} + O_{2(g)} \rightarrow NO_{x(g)} \tag{1.24}$$

Figure 1.14A presents the SAC, where a ceramic honeycomb structure is placed within a stainless steel canister, constituting the entire assembly known as a catalytic converter. This unit is then mounted in the vehicle's exhaust system, situated between the engine and the silencer (muffler) [77].

Table 1.15: The weight percentage [%wt] of the main chemical compositions in SAC found in literature [78].

SAC Component [% w/w]	SiO_2	Al_2O_3	MgO	CaO	NiO	Fe_2O_3	Na_2O	Reference
A	31.7	39.1	4.6	0.7	0.2	-	-	[79]
B	34.6	31	8.9	-	-	3.6	-	[80]
C	35.3	37.2	8.5	1.2	-	-	2.4	[81]
D	40	31.7	10.5	-	-	1.3	-	[82]
E	62.1	10.4	0.4	0.3	-	-	-	[83]

SACs composed of 85% carrier (substrate) and 5–15% coating as seen in Figure 1.14B-C-D. Honeycomb ceramic substrate is commonly made of cordierite region of MgO-Al_2O_3-SiO_2 ternary which is approximately (2:2:5) despite the exact composition varies by the company and the vehicle type. On top of the honeycomp structure, there is a (<90%) γ-Al_2O_3 washcoat that contains relevant PGMs to act as catalysts [78], [84] Chemical compositions taken from different SAC sources were given in Table 1.15.

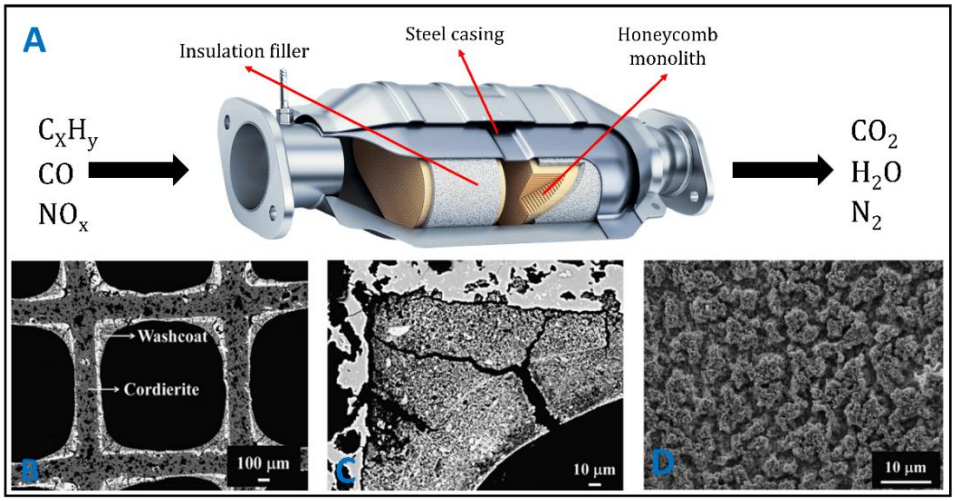

Figure 1.14: (a) Structure of Auto-catalytic convertor, presenting the oxidizing reactions of C_xH_y, CO and NOx to less toxic species as CO_2, H_2O, N_2. (b-c-d) Photos are SEM images of WAC, where PGM containing washcoat is on the cordierite body [83], [85].

The concentrations of platinum-group metals (PGMs) in catalysts exhibit significant variability based on the manufacturer. Moreover, in new car catalytic converters, platinum, typically present in larger amounts compared to palladium and rhodium, shows concentration ranges from 100 to 3000 ppm. Palladium concentrations vary from 5 to 1700 ppm and rhodium concentrations range from 5 to 240 ppm. Consequently, the total PGM content in the samples consistently remains below 0.1%. X-ray powder diffraction is unable to identify phases with such low concentrations [85].

Table 1.16: Typical PGM loadings in autocatalytic converters [86].

Total PGM Loading	PGMs present [ppm]			Reference
	Pt	Pd	Rh	
140	140	-	-	[87]
230	130	76	24	[88]
384.9	380	3.8	1.1	[88]
400	400	-	-	[89]
540	110	360	70	[88]
572	441	-	131	[90]
840	840	-	-	[87]
1160	370	630	160	[91]
1430	1280	-	150	[92]
1940	-	1698	242	[93]
2830	2300	530	-	[94]
3160	1800	1200	160	[95]
12,000	3790	5820	2390	[96]

The pyrometallurgical process provides an efficient approach for the enrichment of Platinum Group Metals (PGMs) from spent automotive catalysts [97]. Base metals such as lead, copper, nickel sulfide and iron are commonly utilized as metal collectors for PGMs [77]. At elevated temperatures, Pt, Pd and Rh are concentrated and enter into an alloy phase. The PGMs alloy and molten slags are separated due to their difference in densities.

Table 1.17: Different metal collectors used in PGM recovery from SACs and corresponding efficiencies throughout the literature [77].

Metal Collector	Temperature [°C]	PGM recovery efficiency			Reference
		Pt	Pd	Rh	
Lead	1130	<98	<98	95	[98]
Copper	1300	<95	<95	<95	[71]
Copper	1550	90	82	82	[99]
Copper	1500	<84	<84	<84	[100]
Copper	1550	-	<97	-	[101]
Iron	>1600	<98	<98	<97	[77]
Iron	1560	<90	<90	<90	[9]
Ni_2S_3 or CuS matte	1050	90	93	88	[102]
Fe matte	950	99	99	97	[103]

Variety of metal collectors and their PGM recovery efficiency from literature were summarized in Table 1.17 Although the collection and cupellation of Pb offer an easy process with a high recovery rate of PGMs, it comes with drawbacks such as a lengthy processing period, high energy consumption and the emission of volatile lead [101]. proposed a method involving the capturing of Pd by molten copper at 1250–1400 °C, achieving a 97% recovery under optimal conditions. Large-scale applications, like those at Tanaka Precious Metals in Japan and Umicore in Belgium, have employed the copper collection method [71]. Jinchuan Group Co., Ltd in China employs nickel matte for capturing Platinum Group Metals (PGMs) from ores. This choice is driven by the close affinity of nickel matte for PGMs and it takes advantage of the unique chemical composition of copper and nickel ore [104]. However, environmental concerns need special attention, especially with melting collection by copper and nickel [105], [106].

Given its non-toxic nature, cost-effectiveness and high affinity with PGMs, iron emerges as a promising collector for concentrating PGMs from spent catalysts [9]. The plasma furnace and electronic arc furnace (EAF) are primarily employed for the iron melting collection process. Industrial-scale applications using plasma melting technology have achieved recovery efficiencies of over 98% for Pt, Pd and Rh [77]. However, the operation temperature in the range of 1600–2000 °C can result in the reduction of Si and the formation of Fe-Si alloy, posing challenges in terms of dissolution and recovery efficiency of PGMs. Furthermore, maintaining the properties of refractory materials at such high temperatures proves to be challenging.

1.5. Direct Current Electric Arc Furnace (DC-EAF)

DC-EAFs, are employed numerous pyrometallurgical recovery routes from waste materials owing to its ability to reach high temperatures in short time with a average crucible temperatures up to 1800 °C. Especially, DC-EAFs became advantageous for treating complex structures such as SACs [9] PCBs [107] and non-ferrous slags [107] which are either difficult to separate or smelt. For this reason, an EAF is designed and constructed due to its ability achieve an adaptable metal recovery process from slag phase by sustaining the high temperature environment to reduce viscosity of melt and provide necessary conditions for reductive environment.

EAFs utilize electric arc to melt metals and create heat for various industrial processes. As seen in Figure 1.15, DC-EAFs are made up from three main part; a furnace hearth with a roof, mechanical equipment and electrical equipment. [108]. Hearth is a closed section of the furnace where the smelting occurs. Hearth includes a steel shell covered by refractory linings from inside, a roof with gas exit and graphite electrodes. Mechanical system is used variety of operations; tilting the furnace hearth, electrode motion, lowering the roof and flue gas systems. Electrical system comprises a power input, a transformer, control unit for electrode movement and power.

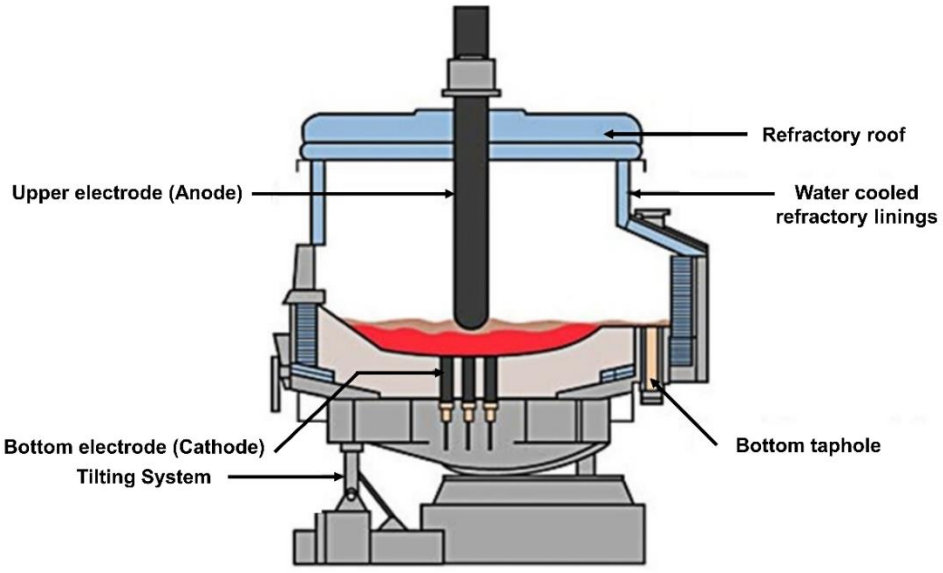

Figure 1.15: Illustration of industrial scale DC EAF [109].

The main furnace body is installed on a tilting system to allow adjustments for proper furnace positioning during tapping operations. Apart from the main body, there is an upper electrode connected to a motion unit, serving to regulate the arc length and enable tilting the main body hearth. The electrode holder is connected with a cooling unit. Electrodes are automatically raised and lowered by the motion unit. Even though, the arc distance between the charge material and the electrodes may change due to melting effects, this positioning system ensures that an approximately constant current and power balance are maintained during the process. Since the electrodes move up and down automatically, water-cooled cables, pipes and arms are constructed adjacent to the transformer and furnace.

1.5.1. Arc Melting

The arc is generated between the upper anode and the bottom cathode. After arc created and the solid mix is started to melt, liquid metal acts as the cathode. The molten metal is heated by the current passing through a highly resistive area, combined with the radiant heat generated by the arc. A plasma arc, is a path of conductive, ionized particles that forms at high temperatures between the cathode and the molten bath. As seen in Figure 1.16, ionization of gas molecules is the formation of both positively charged ions and negatively charged electrons at temperatures above approximately 5000K, creating a neutral but highly conductive plasma. During the arc formation, electrons are released from gaseous molecules. Through collisions with neutral gas molecules, these electrons generate additional free electrons. The newly formed electrons acquire high kinetic energy, enhancing their mobility.

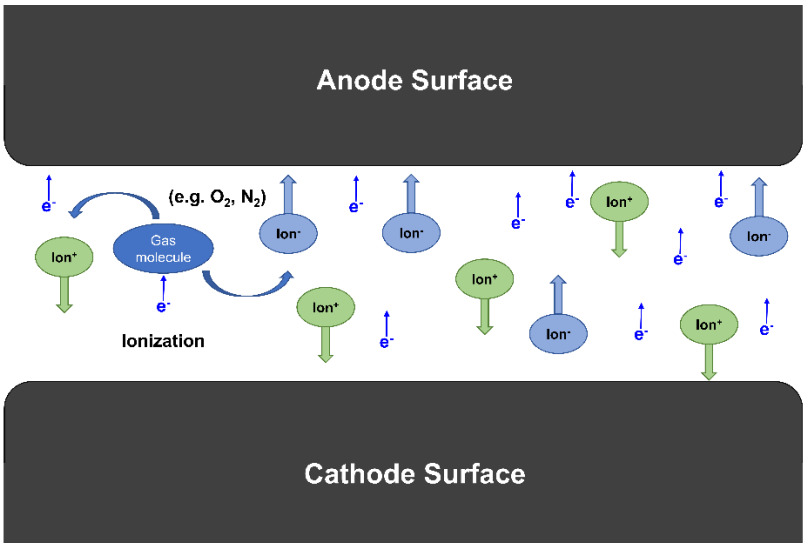

Figure 1.16: Illustration of an arc formation in the ionized gas phase.

The arc is effective on the anode; accelerated electrons collide with it, heating and raising it to very high temperatures (anode effect). Positive ions are accelerated in the opposite direction and collide with the cathode; these positive ions transfer their energies to the cathode, providing continuous thermo-electronic emission and increasing the electric field (cathode effect). These collisions keep the cathode incandescent and lead to the vigorous acceleration of electron deficiency [110].

This conductive medium allows the flow of electric current from the graphite electrode to the furnace bath, completing the circuit. The electromagnetic forces exert a powerful downward drive on the plasma flow within the arc column, creating a jet that extends from the electrode to the molten bath. The flow of plasma in the arc column is directed downward in a powerful jet towards the molten metal bath from the electrode due to electromagnetic forces. Most of the energy from the arc is transmitted to a localized region directly beneath the arc, which proves to be an efficient way of heating the material [111].

In EAF, heat which arises from the arc transferred to smelting hearth radially, as schematically depicted on Figure 1.17. During the arc formation, temperature increases almost instantaneously at the arc region and heat decreases radially. it can also be observed that the gas volume along the arc axis is cylindrical in the initial isothermal layer at 10000°C. Subsequently, in the isothermal gas layers ranging from 8000°C to 3000°C, the anode exhibits a conical shape [110], [112].

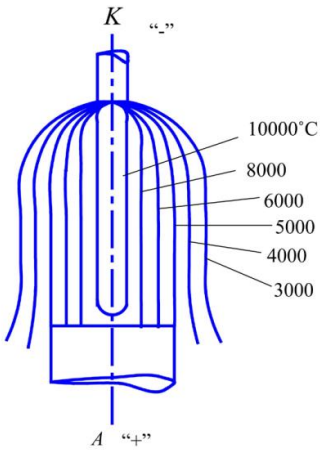

Figure 1.17: Isothermal co-axial layers formed during arc melting (200 A current, 50 mm arc length, carbon electrodes) [110], [112].

The power supplied by the arc can be controlled by adjusting the arc length and current [111]. The electrodes are automatically raised and lowered by a positioning system. Despite variations in the arc distance due to the effects of melting between the charge material and the electrode, this positioning system ensures the maintenance of approximately constant current and power balances throughout the process. Because the electrodes move up and down automatically, water-cooled cables and pipes, as well as transformers, are constructed adjacent to the furnace [113].

Arc is defined by the voltage drop and current across a pair of electrodes. It is commonly recognized that an arc occurs when electrical discharge currents surpass values within the range of 100 mA to 1 A between two polished electrode surfaces. The associated voltage drop typically falls within the range of a few volts to a few tens of volts. The upper limit for current in an arc is often unspecified but is generally substantial, reaching into the order of thousands of amperes. Figure 1.18 shows currents below this specified threshold range, two other discharge types are observed: glow discharge (current ~100 μA to 100 mA; voltage ~100 to 300 V) and dark discharge (current <1 μA; voltage ~1–2 kV). The transition from glow discharge to arc discharge occurs abruptly with an increase in voltage alongside increasing current, followed by a rapid drop in voltage and the passage of higher currents through the arc (up to ~1 kA or higher) [114].

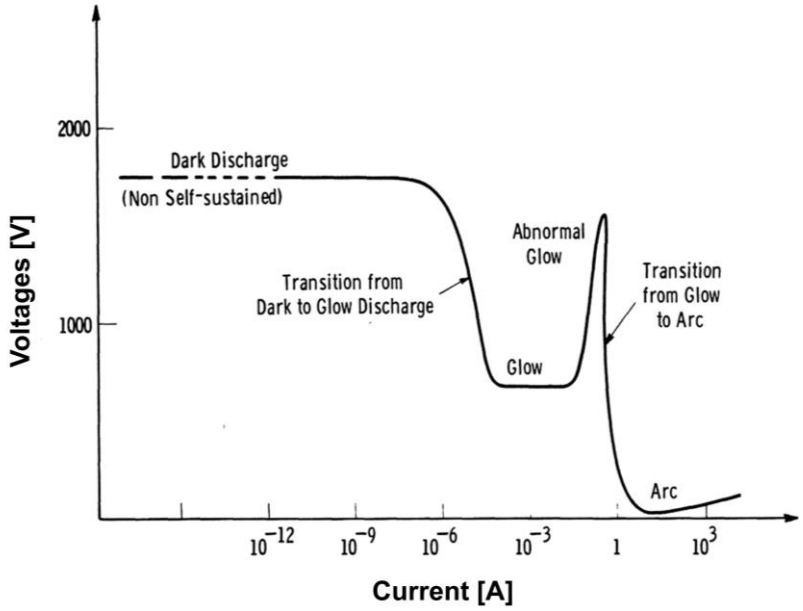

Figure 1.18: Approximate voltage vs. current characteristic of the electrical discharge without tips or edges [114].

The classification of an electric arc into high-pressure arc and low-pressure arc is contingent upon the gas pressure surrounding the electrodes. While there are no clear-cut distinctions between these categories, it is generally acknowledged that arcs formed under gas pressures below 1 mm Hg are considered low-pressure arcs, whereas those formed at gas pressures exceeding 100 mm Hg are classified as high-pressure arcs.. The region between 1 and 100 mm Hg is considered a transition region. In the case of low-pressure arcs, the ion temperature (T^+) and gas temperature (T_g) are comparable (~few hundred Kelvin), while the electron temperature (T^-) is significantly higher (10^4 –10^5 K). Conversely, in the high-pressure arc region, all three temperatures are reasonably close to each other ($T^+ \sim T^- \sim T_g \sim 10^4$ –10^5 K) . Each temperature is defined in terms of the kinetic energy of the component (Eq 1.25);

$$\frac{3}{2}kT = \frac{1}{2}mv^2 \tag{1.25}$$

where (**k**) represents Boltzmann's constant, (**m**) is the mass of particles and **(v)** is the root mean square velocity [114]. Arc melting furnaces operating at ambient pressure or above

are considered high-pressure arc-type systems and the arc plasma is deemed to be in a state of local thermodynamic equilibrium.

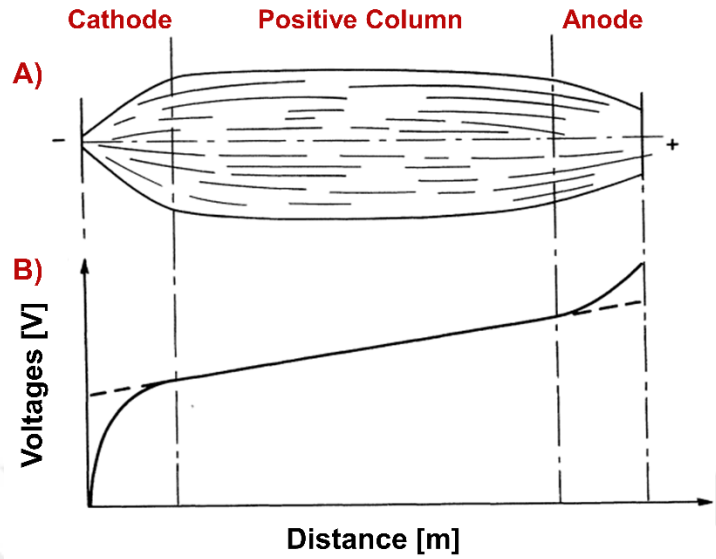

Figure 1.19: Illustrations of arc regions. (a) Corresponding voltages. (b) (Figure modified from [114].)

Both low-pressure and high-pressure arcs are conventionally divided into three regions. Figure 1.19a provides a schematic representation for general applicability. The cathode is positioned on the left, while the anode is on the right. The discharge seems constrained at both ends, with a significant constraint at the cathodic end. This configuration allows for the division of the arc into three distinct regions: the cathodic region, the positive column (with the term "positive" holding a historical significance) and the anodic region.

Arc voltage ($\mathbf{V_{arc}}$) is defined between the voltage drop ($\mathbf{\Delta V}$) between the cathodic region (+) and the anodic region (-). As shown in Figure 1.19b, The cathode region is the area adjacent to the cathode where the current is partially transferred from the plasma arc column to the cathode through slowly bouncing positive ions. The anode region, similarly, is the area adjacent to the anode where a voltage drop occurs due to the electric field (E) created by the electron cloud [114], [115].

In a continuous arc, a balance is established between power input and output and when this balance is disrupted, the arc becomes discontinuous. The arc column is the ionized gas region where there is approximately an equal positive and negative charge density and a

relatively low axial electric field compared to that of neutral gas molecules. The heat generated by I^2R losses in the arc column facilitates ionization, radiating axially towards the electrodes and radially outward from the arc. The energy emitted in the arc preserves ionization in the arc column.

An electric arc is a plasma composed of ionized particles, electrons and gas molecules in thermal equilibrium, forming a heat source for melting process [115]. The arc is emitted from the cathodic electrodes (with negative polarity). Electrons accelerate due to the cathodic potential drop. In this region, these electrons exert a force **F** (as seen Eq. 1.26) under the influence of the predominant electric field strength E.

$$F = e.E = e.dV/dx \tag{1.26}$$

During arc, electrons gain significant kinetic energy, enabling them to dissociate from gaseous molecules and subsequently ionize neutral atoms through collisions. This process generates additional free electrons. The resulting arc plasma comprises ionized particles at exceedingly high temperatures, creating a conductive path between the electrodes [115]. The plasma column, formed by ions and electrons, constitutes the arc. Ionized gases are schematically illustrated in Figure 1.16.

Arc length

Equation 1.27, has been formulated to describe the static arc nature (specifically capturing the decrease in arc voltage as a function of arc current) for carbon electrodes in an open-air (atmospheric) environment where:

$\mathbf{V_{arc}}$ is voltage

$\mathbf{L_{arc}}$ is arc length

I is the arc current

$$V_{arc} = 30 + 12L_{arc} + \frac{120L_{arc}}{I} \tag{1.27}$$

The general behavior of electric arcs was described by Browne in 1955 [5]. Figure 1.20 illustrates the characteristic behavior of arcs with lengths of 1, 10 and 100 cm.

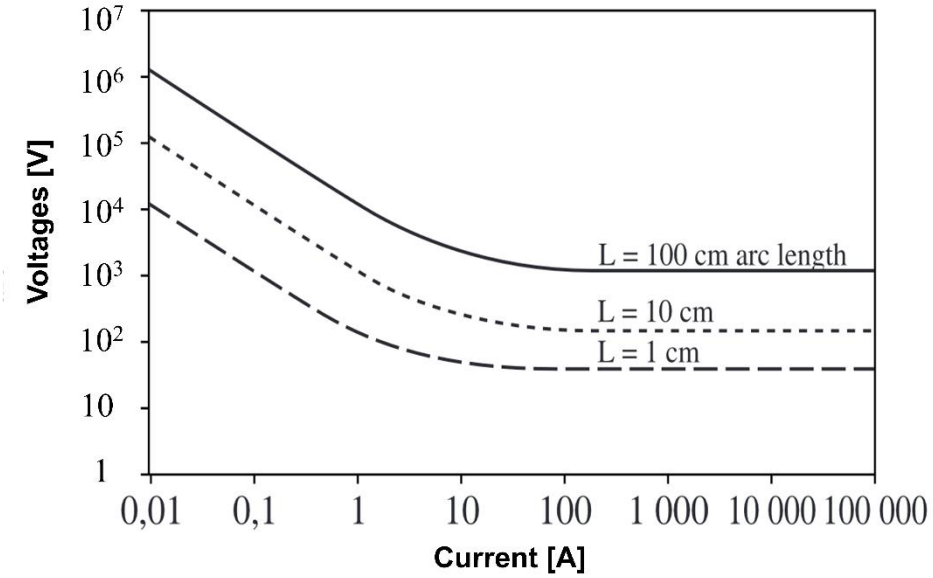

Figure 1.20: In open air, the static property of the arc, specifically the arc length, is expressed as $V_{arc}=f(I_{arc})$ [115].

As the current (I) increases, the arc voltage decreases. The constant term of 30 V accounts for the combined cathodic and anodic drops. The electric field's order of magnitude in the cathodic fall zone is 10^6 V/cm. The second term, 12 V/cm, establishes the connection between arc voltage and arc length. Beyond arc currents of 100 A, the static arc characteristic is diminished to (Eq.1.28):

$$V_{arc} = 30 + 12L_{arc} \quad (1.28)$$

In electric melting furnaces, operating with currents of 10−20 kA and voltages between 100 and 270 V, with open-arc lengths of 6−30 cm, the arc voltage gradients ranging from 4−6 V/cm are significantly lower than those observed in open-air arcs (11−12 V/cm). This difference is due to the high temperature of the atmosphere where the arc is produced (1600 °C) and to the composition of the gas in the arc (CO/CO_2). The presence of metallic fumes also leads to a decrease of the arc voltage gradient. Conversely, for an arc submerged in a foaming slag, the gradient is higher due to a cooling effect of the arc. It is equal to 13 V/cm for an arc operating with a continuous current and 9 V/cm with an alternating current [115]

2. EXPERIMENTAL

The main objective of this thesis is to formulate a slag treatment process for the enrichment of metals from non-ferrous slags, together with secondary sources such as SACs, jewelry wastes and PCBs. The work involves the design of an electric arc furnace (EAF) and a slag optimization methodology that could be adapted to non-ferrous slags and various secondary sources.

2.1.Direct Current Electrical Arc Furnace (DC-EAF) Design

To provide an efficient metal/slag seperation, high temperature environment that could easily reach temperature as high as 1800 °C which even could be used to smelt cordierite phase from auto-spent catalysts. For this reason, an electric DC arc furnace (DC-EAF) was chosen for its capability to reach and maintain high temperatures rapidly. To ensure a continuous and stable arc within the furnace, an electrode motion unit with automation was developed. In the design of the crucible, careful consideration was given to both heat transfer and phase solubility of the chosen refractories.

Power Source and Cables

Power Transformer and Rectifier were retrieved from SONMEZ Trafo Inc. Transformer were connected to bridge rectifier to obtain DC current. Main parameters of transformer system were given in Table 2.1.

Table 2.1: In and output parameters of power source and matching rectifier.

Input parameters		**Output parameters**	
Connection mode	Triangle/Star	Rectifier mode	Triangle/Star
Input Voltages	AC - 380 V	Output voltage	DC - 60 V
Input Current	AC – 70 A	Output Current	DC - 200 A

Cables were selected by considering the maximum current that used in the EAF system, in this regard selected cables must withstand minimum current of 200 A which the maximum current output of the power source. For this reason, AWG 3/0 copper cable having approx.

1 cm diameter and multiple cores were selected to add flexibility. The complete electrical schematic was given in Figure 2.1.

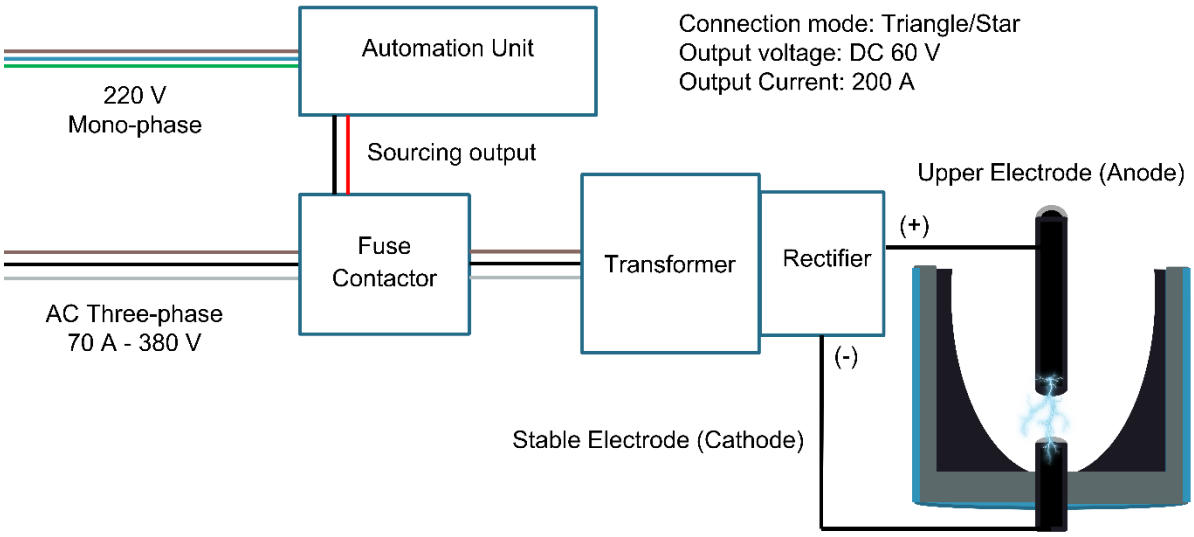

Figure 2.1: Electrical schematic of lab scale direct-current electrical arc furnace system.

Electrode Motion System and Automation

An automation system for control of electrode position and electrode current have established in order to obtain continuous arc melting and precise results. Moreover, the automation system provided autonomous operations for longer working periods and minimized the safety risks. The automation system can be explained under two subsections: "Automation System Hardware" where the infrastructure examined and the "Control Software" where the algorithms and control methods examined.

Automation System Hardware

The hardware of automation system has chosen from industrial control devices in order to keep track in industrial standards and obtain robust infrastructure. The Allen-Bradley Micro820 programmable logic controller (PLC) is the main controller of the system. The system's automation algorithms and control software are implemented on this device. The PLC has a built-in serial communication port that supports RS485 protocol. Additional modules can be added to the PLC to enable analogue sensor readings. Double stepper motors have used in order to obtain the force that moves the electrode table. The frequency reference of the stepper motors has generated with the PWM (pulse width modulation) module of the PLC which is the actual control signal of the position control system. An amperemeter that measures DC current occurring on the shont resistance and a linear

position potentiometer that measures linear vertical position of electrodes have used as feedback sources in the system. These feedback sources have used in accordance with control software and algorithms that ensures expected process outputs. The dynamic system diagram is as seen in the (Eq.2.1). where the *F* is the force applied from the motors and *x(t)* is the position measurement obtained from the position sensor. m represents the mass of the electrode table, *g* represents the gravity, B_1 and B_2 represent viscous friction constants.

$$F(t) = m\ddot{x}(t) + (B_1 + B_2)\dot{x}(t) + mg \tag{2.1}$$

The differential equation represents the system dynamics between the force applied and position obtained is as seen in the (Eq.2.1). The control software of the system has developed according to the dynamical system model in the (Eq.2.1).

System Software

The control software of the system has developed in order to obtain the highest precision on the electrode position and to establish process commands. The control software consists of two parts as the closed loop control loop and automation algorithm.

Two closed-loop systems with P and PV controllers have been developed utilizing the position feedback measured from linear vertical potentiometer and current feedback measured from amperemeter. The inner closed-loop control system consists of PV controller and is used for position control. The outer closed-loop control system consists of P controller and is used for arc occurance control. Control signal is limited to prevent any mechanical damage to the system and ensure that motors function properly. The block diagram of the closed loop control structure is as seen in Figure 2.2.

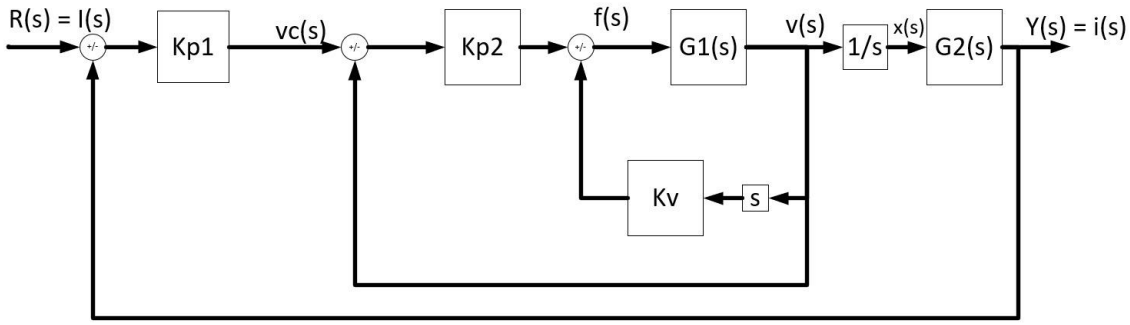

Figure 2.2: The diagram of that closed loop control structure with PV controller.

Here, $\boldsymbol{R(s)}$ is the current reference, $\boldsymbol{K_{p1}}$ is the P controller gain, $\boldsymbol{V_c(s)}$ is electrode velocity reference, $\boldsymbol{K_{p2}}$ and $\boldsymbol{K_v}$ are the PV controller gains, $\boldsymbol{F(s)}$ is the control signal is in terms of PWM signal frequency as Hz, $\boldsymbol{G_1(s)}$ is the transfer function that is the relation between electrode velocity and motor frequency, $\boldsymbol{V(s)}$ is electrode velocity, $\boldsymbol{X(s)}$ is the electrode position, $\boldsymbol{G_2(s)}$ is the relation between the current and electrode position. The PV controller calculates the frequency control signal in (Eq.2.2).

$$C(t) = \Big(\big(r(t) - y(t)\big)K_{p1} - v(t)\Big)\,K_{p2} - \frac{dv(t)}{dt}K_v \tag{2.2}$$

In the equation given; $\boldsymbol{r(t)}$, $\boldsymbol{y(t)}$ and $\boldsymbol{v(t)}$ are current reference, current output and electrode velocity in time doman, respectively. If error $\boldsymbol{e(t)}$ is defined as $\Big(\big(r(t) - y(t)\big)K_{p1} - v(t)\Big)$, the Laplace transform of the control signal can be shown as:

$$C(s) = K_{p2}e(s) - K_v(sY(s)) \tag{2.3}$$

The control signal presented in (Eq.2.2) and (Eq.2.3) has programmed into the control software-using discrete difference equations with sampling time of 100 milliseconds in a timer interrupt of the controller. The reference and output signal obtained from the system in closed loop control are as seen in the Figure 2.3.

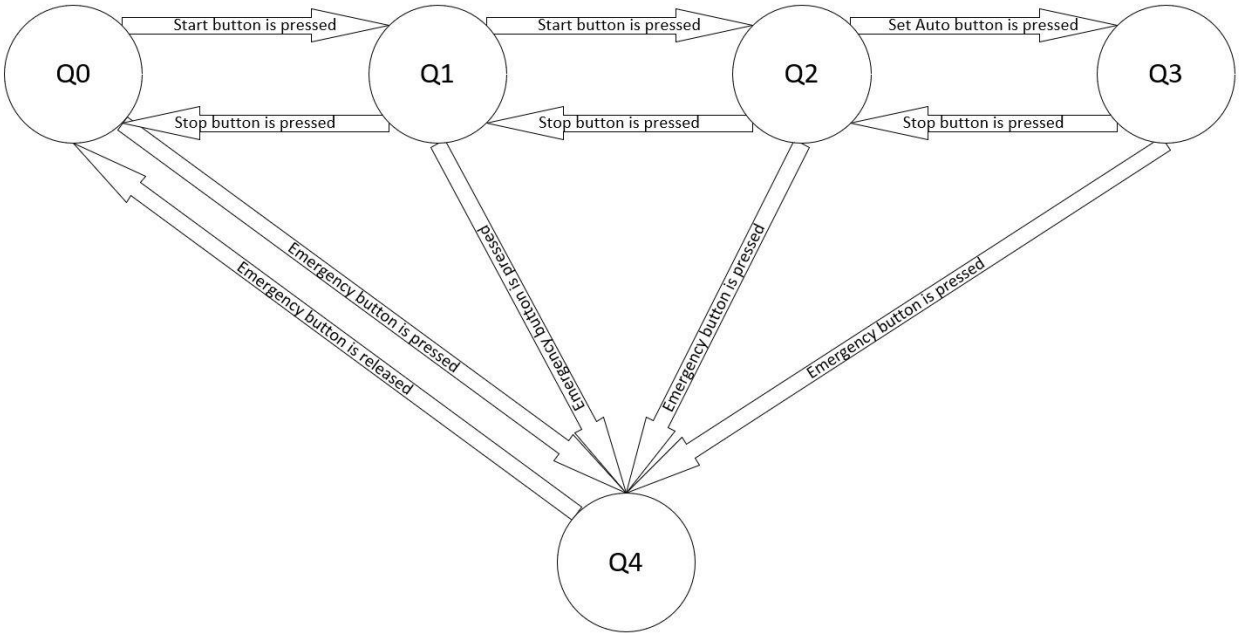

Figure 2.3: The reference and output signal obtained from the system.

Q0 represents the default state where only the PLC is powered on. Moving to Q1 state involves powering on the motor driver along with the PLC. However, in this state, the motors and the arc relay remain inactive, preventing the motors from functioning and the arc from firing. Advancing to Q2 state enables motor operation, allowing adjustment of the upper electrode. Q4 state indicates an emergency situation. If something malfunctions, pressing the Emergency Button triggers an immediate shutdown of all operations. Exiting this state requires releasing the EmergencyButton, returning the system to its default state, Q0. The automation software has developed using finite-state diagrams where every state represents a command expected to occur. There are two different main algorithms in automation software. First one is the state algorithm that determines the flow of the manual process and second one is the state algorithm that determines the automatic mode process. The automatic mode is a sub-algorithm in the main state diagram that activates if several conditions occur. The manual process algorithm which is the main state algorithm is as seen in the Figure 2.4.

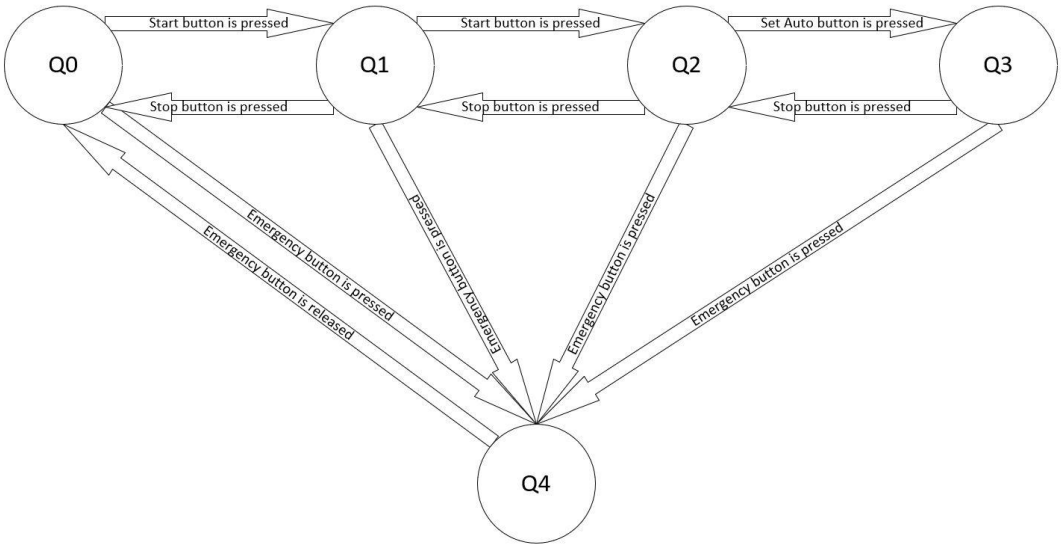

Figure 2.4: The finite-state machine diagram of main process.

The automatic state algorithm actives if auto-button is pressed while the state 3 is on. The automatic mode is consisting of two position reference commands which define the presence of arc current and generation of arc current respectively. The finite-state machine diagram of automatic algorithm is as seen in the Figure 2.5.

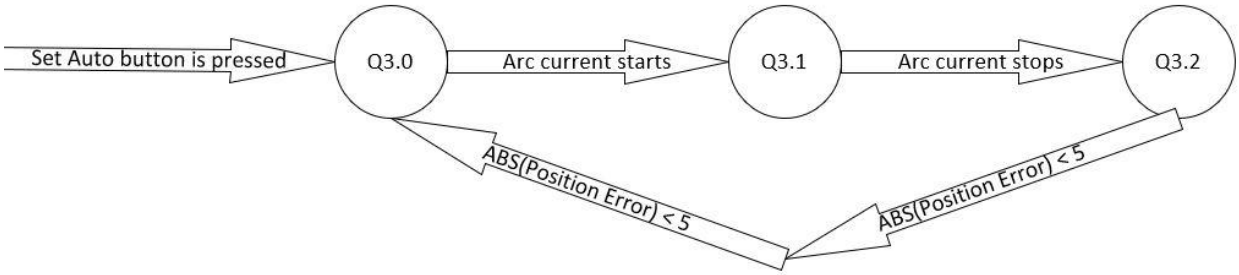

Figure 2.5: The finite-state machine diagram of automatic algorithm.

Crucible Design and Refractory Selection

Refractory phases were selected after considering possible reactions and phase solubility between the refractory and the slag phase. FactSage™ was utilized to determine phase diagrams and equilibrium phases under arc-smelting conditions. Refractory materials must withstand the maximum operating temperature. Therefore, heat transfer analysis was done using ANSYS™ to determine thickness of the selected refractory phases.

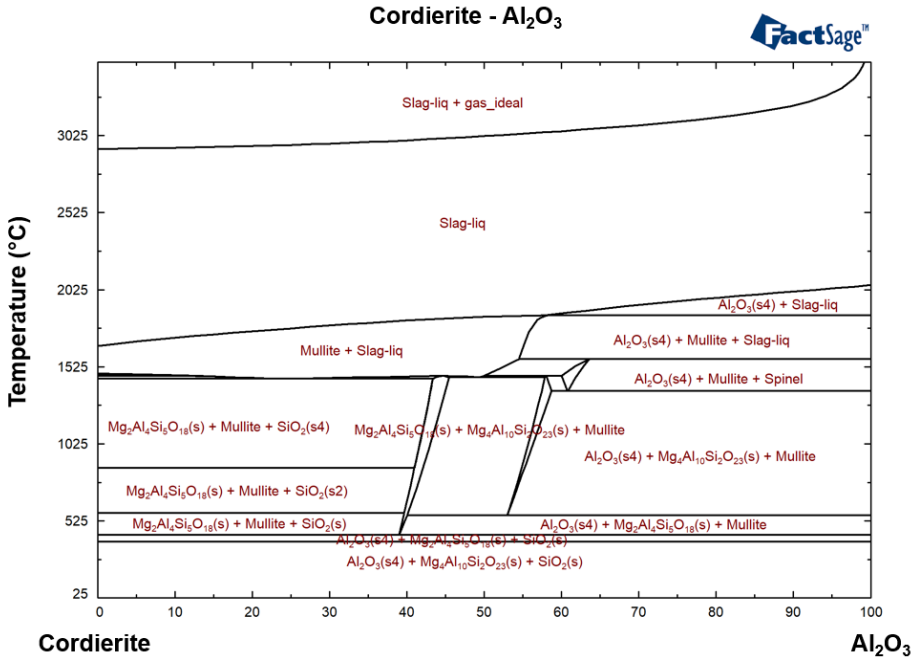

Figure 2.6: Phase diagram of Cordierite phase (SiO_2 54.46%, Al_2O_3 30.84% and MgO 5.57%) and Al_2O_3.

As seen in Figure 2.6 without any flux addition Cordierite phase have a melting point approximately between 1450 °C to 1500 °C. Crucible must withstand higher temperature range than operating temperatures to ensure refractory system could sustain temperature

near 1800 °C. Figure 2.6 shows cordierite to Al_2O_3 phase diagram depicting, even if the melted slag dissolve some of the Al_2O_3 on the crucible surface, melting temperature does not decreased, even increased with the increasing content of the Al_2O_3 due to having a melting temperature of 1840 °C. Therefore in crucible design, Al_2O_3 is selected as as repairable inner refractory due to phase diagram does not consist any eutectic points, relatively withstandable temperature and low cost to repair as the crucible deteriorate overtime. REMCAST HA-95 castable alumina, composition summarized in Table 2.2 retrieved from Remsan Inc. was used.

Table 2.2: Phase percentages of used castable refractory (REMCAST HA-95) determined of XRF for inner crucible section.

Phases	**Al_2O_3**	**TiO_2**	**SiO_2**	**Fe_2O_3**	**CaO**	**Others**
[% w/w]	95.2	0.1	2.9	0.1	1.7	0.2

Magnesite bricks were used to construct the outer section, bonded together with a mixture of ZrO_2:Al_2O_3 (1:2) and 10% Na_2SiO_3. The inner section was cast into a crucible using a wooden template thus crucible prepared by heating first 120 °C for 12 hour and then 560 °C for 2 h. In Figure 2.7a, an illustration of furnace hearth was given. Although the electrical arc can generate temperatures as high as 5000 K, the heat decreases radially in relation to the diameter of the hearth, as discussed in the arc formation chapter. For this reason insulation becomes crucial to preserve heat. Moreover, the configuration of crucible shape also holds a particular importance, when it comes to collection of metals from the slag phase. The design of the crucible's shape must allow high density metals to settle and enrich in the metal collector phase. This need led to adoption of arc-shaped bottom for the crucible as seen in Figure 2.7c.

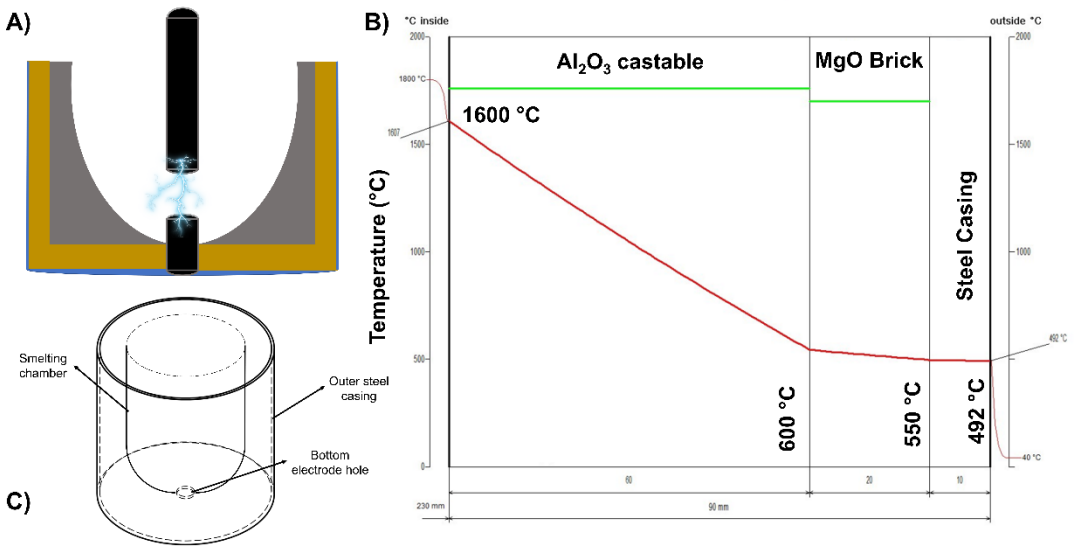

Figure 2.7: Illustration of refractory part of EAF crucible. (a) A graph showing the heat transfer produced from the arc to outer steel casing. (b) Technical drawing presenting the morphology of the crucible. (c)

Vast amount of heat is generated from the arc during smelting where the crucible must be able to withstand this increase in temperature over time. Equally, it is important to control the temperature in the system to avoid any heat loss. For this reason, selection of propriate refractory lining and thickness is important. The arc smelting will take place at the temperatures high as 1800 °C in the hearth therefore heat transfer analysis (Figure 2.7b) were made when at inner surface temperature taken as 1600 °C. The results showed that at 6 cm Al_2O_3 2 cm MgO, 1cm steel casing is selected for refractory thickness, the final temperature could reach temperatures up to 500 °C. In this study, a cooling system was developed to protect cables by cooling the anode, as opposed to the furnace hearth. Where the heat is convectionally transfered to upper electrode. This choice was made because the DC-EAF setup is specifically designed for experimental studies rather than continuous smelting operations.

Electrode Design

In electrode selection, graphite electrodes were chosen due to their high conductivity and heat resistance which is also the most common selection in the EAFs. Electrodes carry the current while produces heat. The resistivity of the system varies with the electrode diameter ultimately, heat is produced by the current flowing through the electrode. Therefore, it's

crucial to choose the proper electrode diameter. Minimum electrode diameter determined by the (Eq. 2.4) [116]**.**

$$d_{electrode} = \sqrt[3]{\frac{0.406 I^2 \rho}{K}} \tag{2.4}$$

$\mathbf{d}_{electrode}$ = Diameter of electrode

I = Average electrical current (A)

ρ = Resistivity of graphite electrode ($\Omega\ mm^2 \cdot m^{-1}$)

K = Coefficient of heat transfer ($W \cdot m^{-2}.K^{-1}$).

To calculate the electrode diameter is calculated by taking I = 200 A as a maximum current of the transformer. ρ and K of graphite electrode is 10.5 $\Omega\ mm^2 \cdot m^{-1}$ (at 500 °C) and 2.1 x 10^4 $W \cdot m^{-2}$ respectively [116].

$$d_{electrode} = \sqrt[3]{\frac{0.406 * 200^2 * 10.5}{2.1 * 10^4}} \tag{2.5}$$

$$d_{electrode} = 2.00995\ cm \tag{2.6}$$

According to (Eq. 2.4), the diameter that withstand the current flow must be longer than 2 cm thus 3 cm graphite electrodes were chosen to ensure safety and heating of the electrodes.

Photo of DC-EAF constructed during this study is shown in Figure 2.8. System consist of a power source, automation control panel, a mechanical tilting system that holds a refractory crucible and an electrode motion system that carries anode as seen. Insulators were used to connect the cathode to the bottom of the crucible, preventing short circuits. The DC-EAF system was grounded at multiple points and the electrode connections were designed to facilitate straightforward electrode renewal.

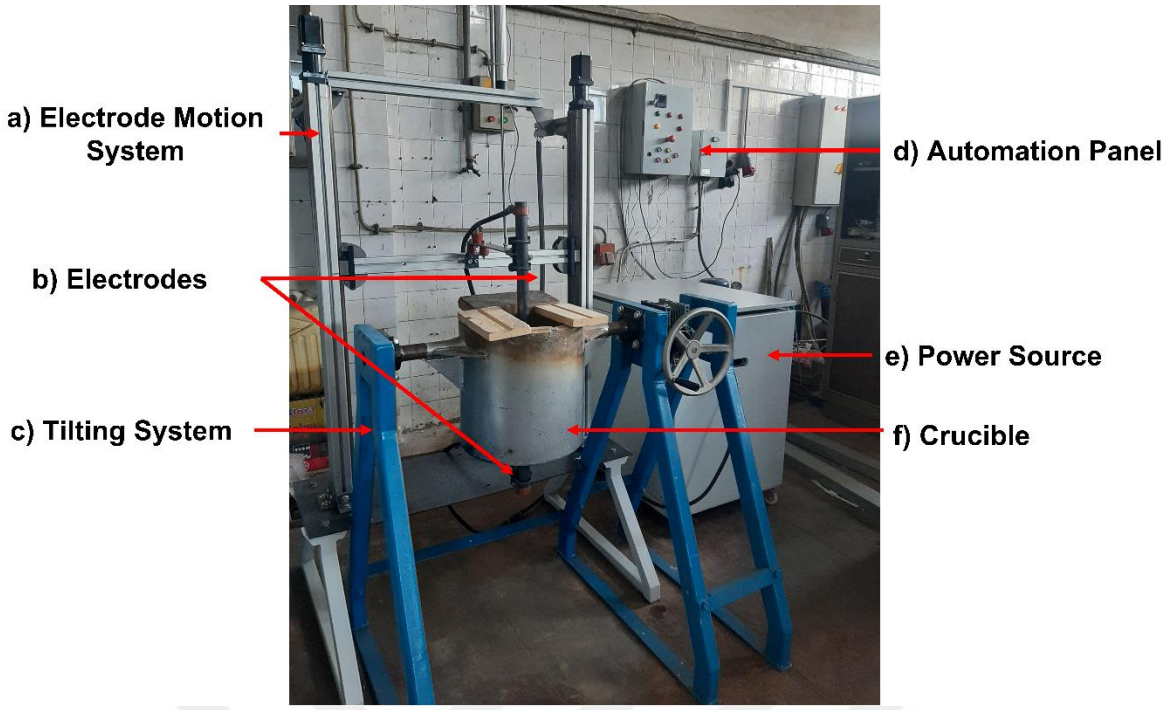

Figure 2.8: A photograph of lab-scale electric arc furnace.

2.2. Thermodynamic Slag Optimization and Arc Smelting Experiments

For slag optimization and arc smelting experiments, 3 types of slag were used; SACs were taken from Vessem Recycling Co. Cu flash furnace slag was retrieved from Eti Bakır Inc. and jewelery waste slag from Nadir Metal Co. Phase investigations of slags were done by a Bruker D8 Advanced Series X-ray diffraction (XRD), with Cu-K_α radiation (λ = 0.154 nm, 35 kV and 40 mA), 2θ range of 20–90°, step size of 0.02° and rate of 2°/min. Crystalline phases with crystal structures and lattice parameters were identified using The International Center for Diffraction Data® (ICDD) powder diffraction files. Phase percentages of slag phases were determined by Panalytical Axios® X-ray fluorescence (XRF). Leica optical stereo microscope was used to present metal entrapment within the slags.

For slag optimization experiments were done using, medium frequency induction furnace (50 kHz, 30 kW, 40 A) in F3 scale graphite crucible. Samples were heated 1 h. at 1250 °C. All slag experiments done in induction furnace. To assess metal recovery efficiency, 5% copper was introduced during the smelting process. Recovery efficiency was determined by the difference between initial and final metal concentrations in the slag.

Binary phase diagrams of SiO_2-Al_2O_3-FeO-Na_2O-B_2O_3-CaO, phase equilibrium diagrams, viscosity calculations and Gibbs free energy (ΔG^{θ}) of reactions were made using software FactSage™ version 8.3. In this paper, the basicity (R) was defined as the mass ratio of CaO+MgO+Na_2O and SiO_2-Al_2O_3-B_2O_3 while the enrichment coefficient of PGMs was the mass ratio of concentrations in iron alloy and spent catalysts. Slag density were determined using an archimedes' equipment for density measurement.

Thermal behavior of the slag samples were analyzed through dynamic scanning calorimeter (DSC). The samples underwent heating at a rate of 10 °C/min, reaching temperatures between 900 - 1500 °C. Additionally, the samples were held at 1400 °C for a duration of 10 min. during the analysis.

During arc smelting experiments, 5% copper was used as a metal collector phase and 5% carbon was added to create a stable arc environment. Smelting was continued until a homogeneous melt was achieved.All materials were charged to furnace copper, coke, mixed slag+flux powder respectively. For fluxes, $CaCO_3$, Na_2CO_3, H_3BO_4 (analytical grade, Merck™) and $Na_2B_4O_7$ (technical grade, obtained from ETI MADEN) were used.

3. RESULTS AND DISCUSSION

3.1. Characterization of Slags

Figure 3.1 displays the XRD pattern of SAC. Predominantly, SAC consists of cordierite ($Mg_2Al_4Si_2O_{18}$) phase however, $Ce_2Zr_3O_{10}$ and TiO_2 were also detected. This results aligns with the common convertor structure where cordierite used in the honeycomb monolith structure whereas Al_2O_3 serves as a substrate for PGMs, ZrO_2 and CeO_2 particles called the "washcoat".

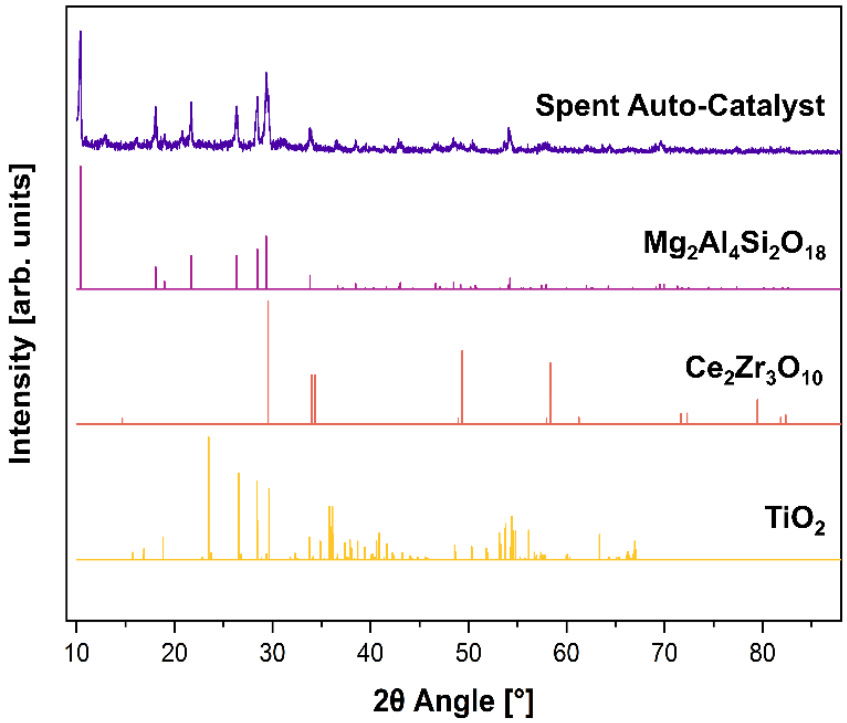

Figure 3.1: X-ray Diffraction pattern of spent catalyst used in the slag experiments.

Table 3.1 shows the cordierite composition used in this study where high percentage of SiO_2 (54.49%), Al_2O_3 (30.84%) and MgO (5.57%) present it the structure which corresponds to ~85% of the total metal oxides thus, XRF results are related with the detected phases from XRF since, CeO_2 and TiO_2 also observed in low concentration – approximately 2% of total weight. These substances are used in SAC as oxygen storage promoters to enhance catalytic activity [117]. While ZrO_2 is utilized in the structure for the

same purpose, the specimen contains only 0.12% of this component. 5.04% loss of ignition (LOI) is attributed to combustion products and other impurities [118].

Table 3.1: XRF quantitative analysis of SAC.

Phases	SiO_2	Al_2O_3	MgO	TiO_2	Fe_2O_3	CeO_2	CaO	CuO	Na_2O	ZrO_2	LOI
% [w/w]	54.49	30.84	5.57	1.16	0.95	0.82	0.21	0.18	0.13	0.12	5.04

XRD of Cu flash furnace slag Figure 3.2, shows the present phases in the structure. As described earlier, in the introduction section, Cu slag mainly composed of $2FeO.SiO_2$ type fayalite slag that have the highest intensity relative to SiO_2 and other phases.

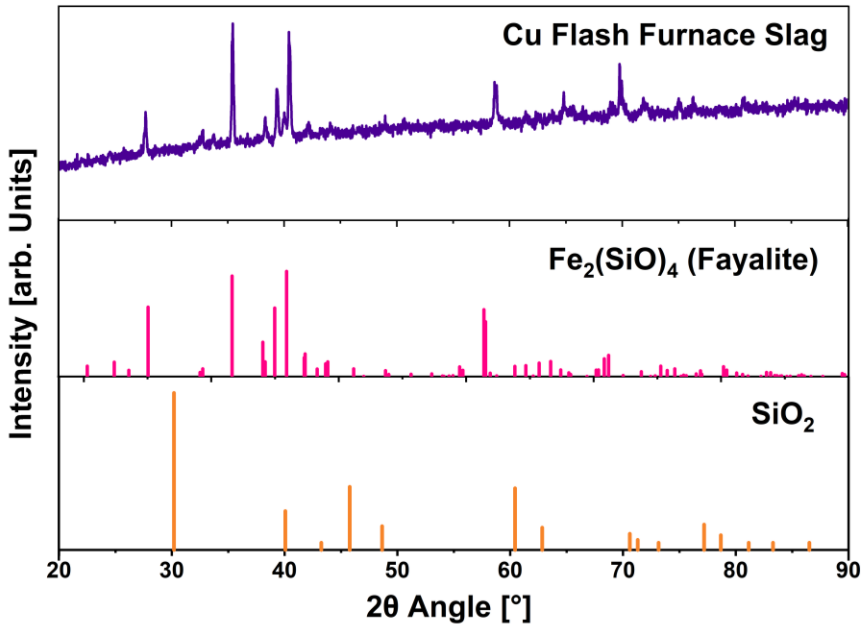

Figure 3.2: X-ray diffraction pattern of Cu flash furnace slag.

XRF data Table 3.2, is correlated with XRD data where high amount of Fe_2O_3 (64%) and SiO_2 (4.26%) also found in the system. In XRF characterization, the oxide mode was utilized for determining the phases. Therefore, it is essential to note that the slag also contains FeS content rather than SO_3, which is originating from the matte. Cu content in the fayalite slag could either be attributed to Cu or Cu_2O

Table 3.2: Oxide composition of Cu flash furnace slag determined by XRF.

Element	Fe_2O_3	SiO_2	SO_3	Al_2O_3	CuO	ZnO	CaO	Na_2O	Other oxides
% [a] [w/w]	64.0	26.3	4.26	1.59	1.39	0.793	0.372	0.279	1.67

[a]In the XRF analysis, oxide mode were used to accurately determine the oxide composition.

The average Cu content in the Cu flash furnace slag was determined using XRF. In Figure 3.3, optical microscope image shows the entrapment of Cu metals by the reflection of light.

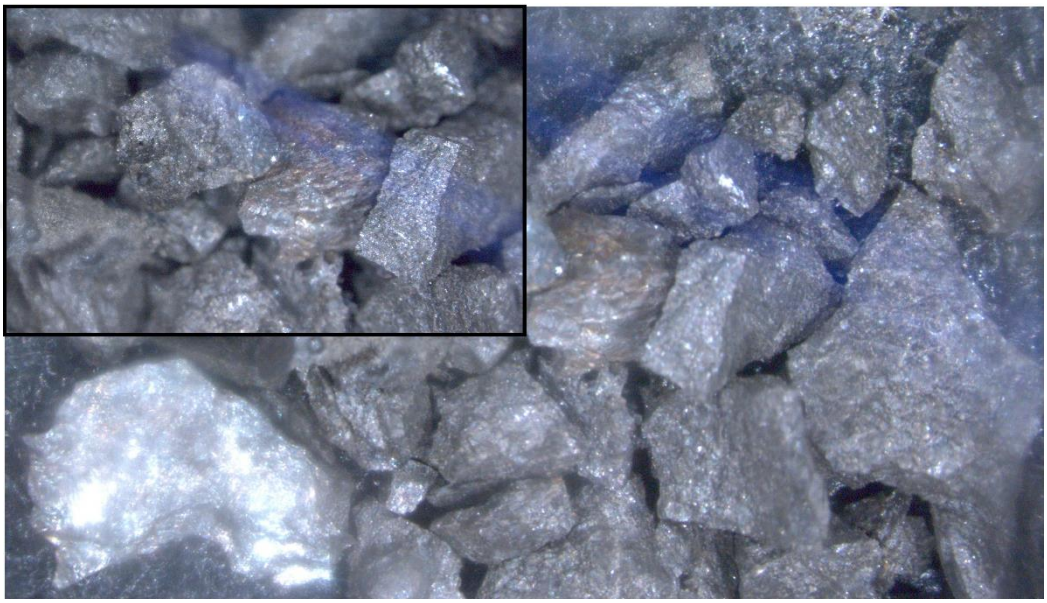

Figure 3.3: Optical microscope image of fayalite slag at x15 magnification. Inset shows image at x45 magnification.

The third slag utilized in this study is a jewelery slag derived from the smelting of low-grade jewelry waste. XRD graph of jewelery slag Figure 3.4, presents high amount of PbO which possibly arises from the Pb cupellation process [75]. Additionally, CuO was also observed.

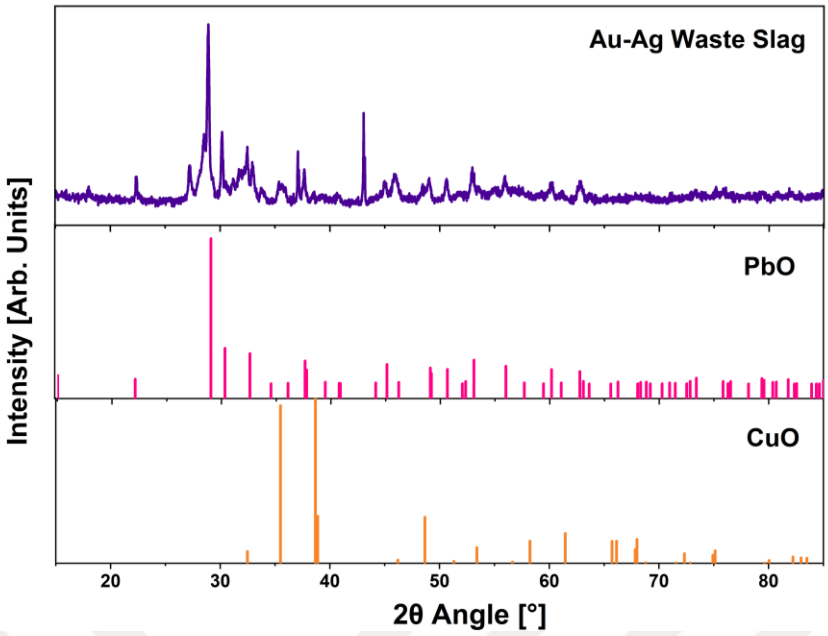

Figure 3.4: X-ray diffraction pattern of jewelery slag from low grade jewelry waste smelting.

XRF analysis of jewelery slag using oxide mode (Table 3.3), also further proves the presence of PbO and CuO, despite CaO and SiO_2 were not observed from phase analysis. Figure 3.5 shows optical microscope image of the jewelery waste slag. Due to high Cu and Ag content metallic particles are dominantly seen from the images.

Table 3.3: Oxide composition of jewelery slag determined by XRF.

Element	PbO	CaO	CuO	SiO_2	SeO_2	SnO_2	SO_3	Al_2O_3	Ag_2O	Other oxides
% [a] [w/w]	55.6	13.1	11.2	6.01	2.44	2	1.86	1.80	1.45	4.54

[a]In the XRF analysis, oxide mode were used to accurately determine the oxide composition.

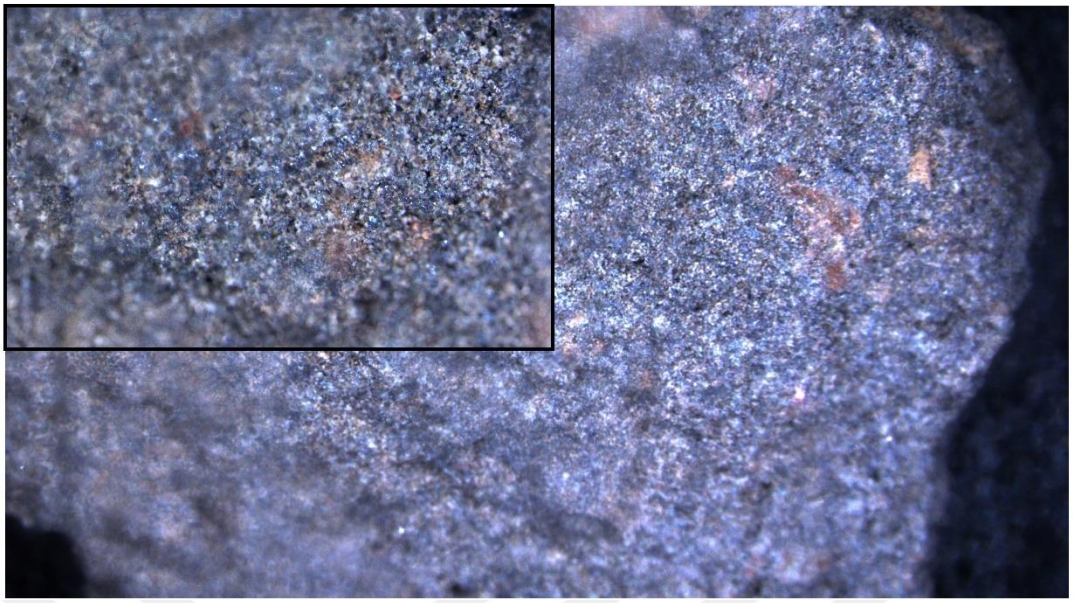

Figure 3.5: Optical image of gold waste slag taken at 15x magnification. Inset shows image at 40x magnification.

According to characterization of above mentioned slags, SAC composition was used in both thermodynamical calculations and thermal behaviour investigations for slag optimization studies due to high melting temperature of cordierite phase (SiO_2-Al_2O_3-MgO) which is 1453 °C and its highly acidic content. Whereas, common non-ferrous slags are fayalite based (SiO_2-FeO) and melt in the range of 1200-1300 °C. In the second part of the study, a generalized slag optimization approach derived from current work will be used and adapted to Cu flash furnace slag and waste jewelry slag thus their recovery efficiency will be determined.

3.2. Slag Optimization Studies

For optimal recovery of metal from the slag, it's essential to create a homogenous slag that incorporates all the oxide constituent in the structure. Moreover, minimizing the viscosity and glass transition temperature (T_g) are important objectives to prevent any loss of metal within the slag, enhancing overall recovery efficiency.

To attain these objectives, behavior of the SAC during the melting process was investigated. Initially, phase equilibrium diagram (Figure 3.6) shows that the composition starts to melt at 1450 °C and incorporated to slag despite, 25% mullite ($3Al_2O_3 \cdot 2SiO_2$) and 10% SiO_2 still present as solid in the structure.

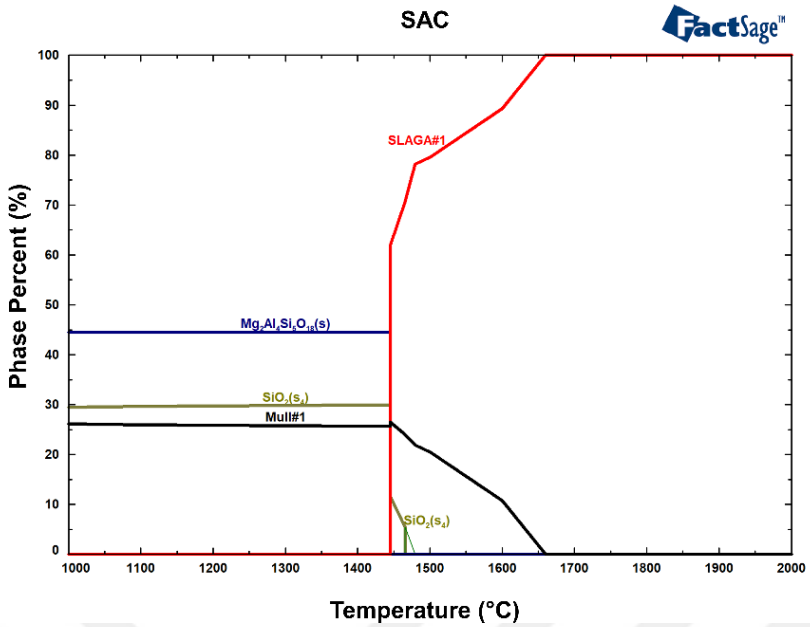

Figure 3.6: Phase equilibrium diagram of SAC at different temperatures. (Composition determined from XRF were used in the diagram.)

Phase equilibrium diagram presents two main objective;

- Obtaining a homogenous melt by forming low-temperature phases involving $3Al_2O_3 \cdot 2SiO_2$ and SiO_2 phases (as seen in Figure 3.6)
- The other reason is to decrease viscosity and Tg/Tm of the slag phase which is formed at 1450 °C to attain an efficient metal/slag seperation.

For above mentioned objectives Na_2O, B_2O_3, CaO were selected as potential flux additions. with the addition of Na_2O and CaO to disrupt silica and alumina networks alongside lowered melting temperature. B_2O_3 despite is a network former, it has an ability to decrease viscosity by breaking $[SiO_4]^{4-}$-$[SiO_4]^{4-}$ and $[AlO_4]^{5-}$-$[SiO_4]^{4-}$ as stated in the literature [78].

3.2.1. Homogenous Slag formation

To investigate the formation of low temperature phases and eutectic point to find the optimum flux additions binary phase diagrams of SiO_2, Al_2O_3 and MgO with potential fluxes; CaO, Na_2O and B_2O_3 were were investigated. FeO also considered due to high percentage in fayalite based non-ferrous slags.

CaO addition on Al_2O_3 (Figure 3.7) have an eutectic point at 1362 °C on 0.354 mole $Al_2O_3/(CaO+Al_2O_3)$ which forms both $Ca_3Al_2O_6$ and $CaAl_2O_4$. CaO addition on SiO_2

(Figure 3.8) have an eutectic point at 1700 °C on 0.65 mole $SiO_2/(CaO+SiO_2)$ thus. $CaO.SiO_2$ phase with SiO_2 is present in the structure.

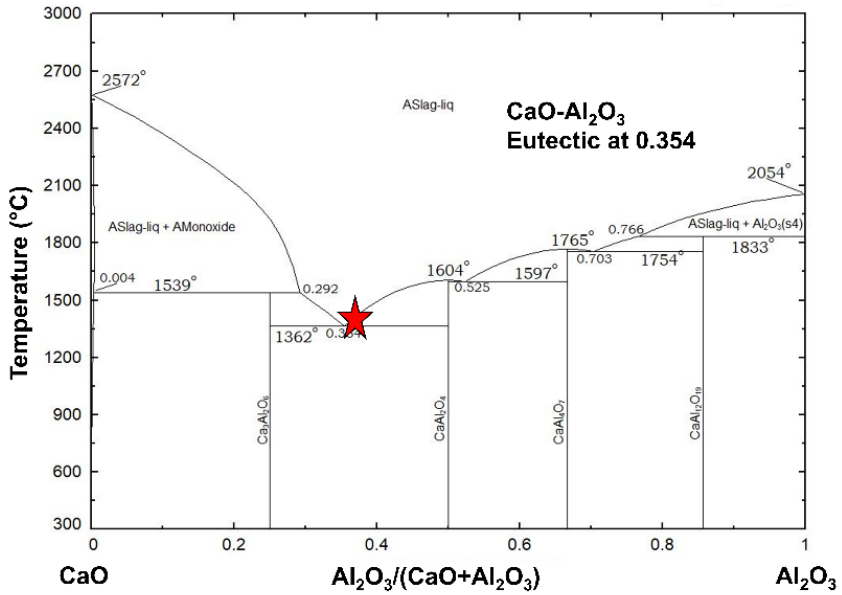

Figure 3.7: $CaO-Al_2O_3$ binary phase diagram.

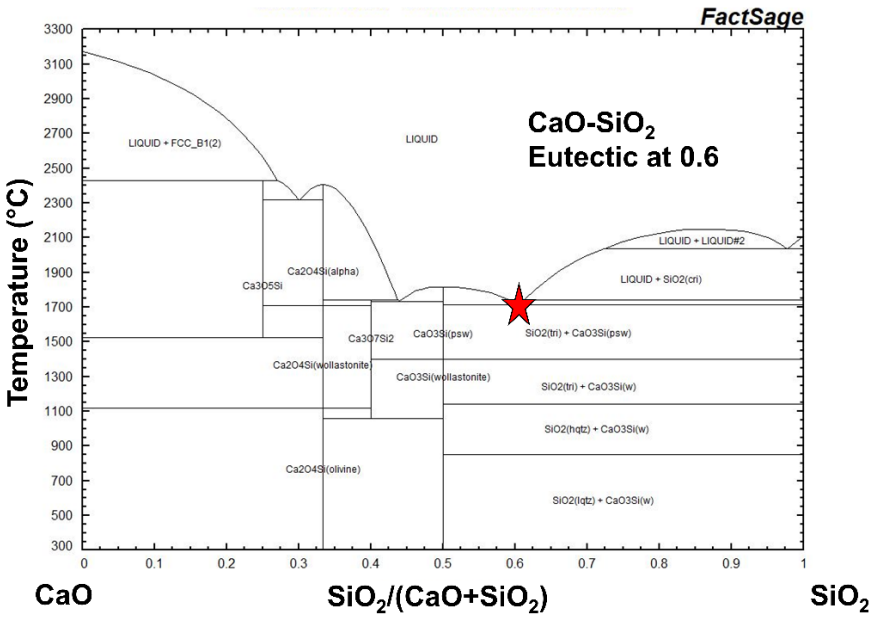

Figure 3.8: $CaO-SiO_2$ binary phase diagram.

As seen in Figure 3.9, Na_2O addition on Al_2O_3 have an eutectic point at 1132 °C on 0.05 mole $Al_2O_3/(Na_2O+Al_2O_3)$ which forms both Na_2O and $NaAlO_2$. Figure 3.10 shows Na_2O addition on SiO_2, which have an eutectic point at 850 °C on 0.75 mole $SiO_2/(Na_2O+SiO_2)$ thus $Na_6Si_8O_{19}$ is present in the structure.

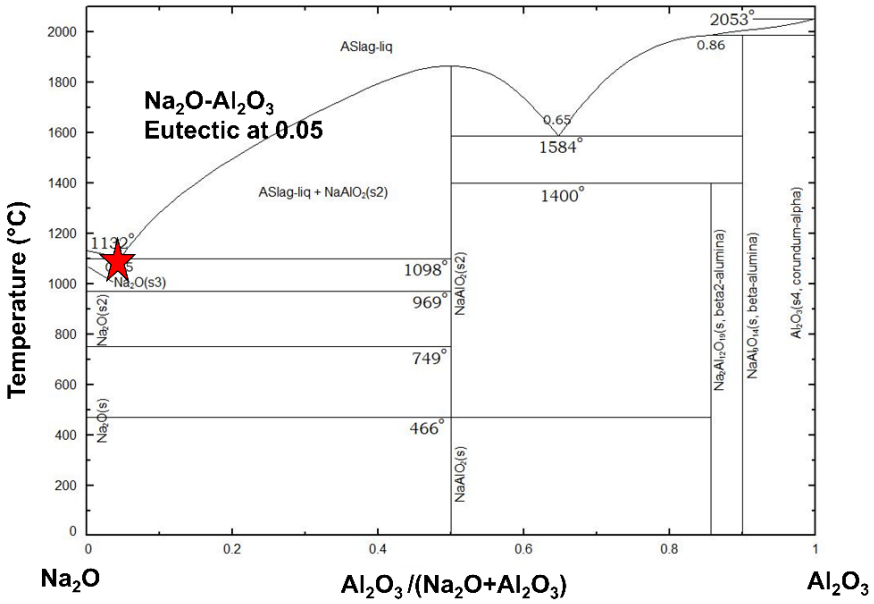

Figure 3.9: Na_2O-Al_2O_3 binary phase diagram.

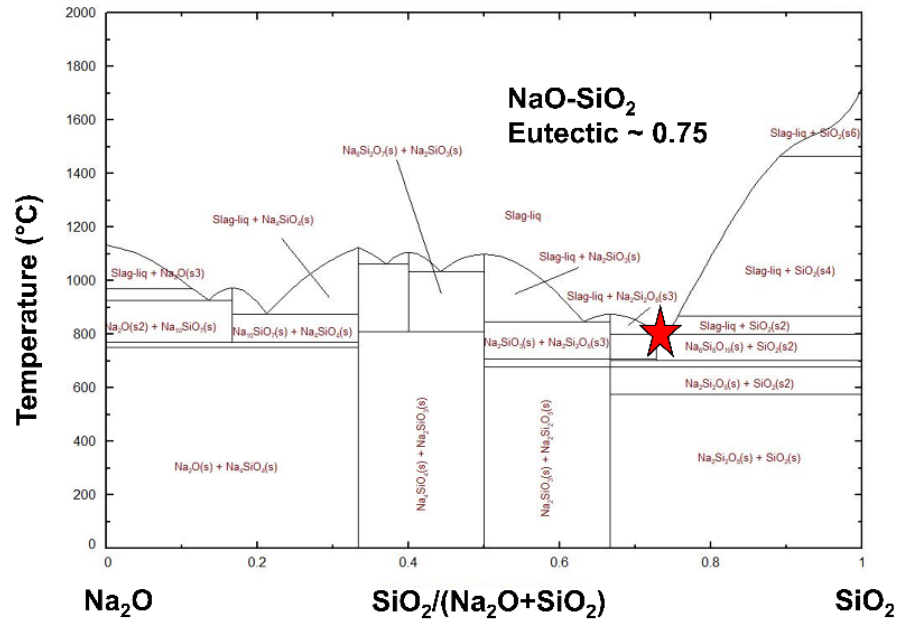

Figure 3.10: Na_2O- SiO_2 binary phase diagram.

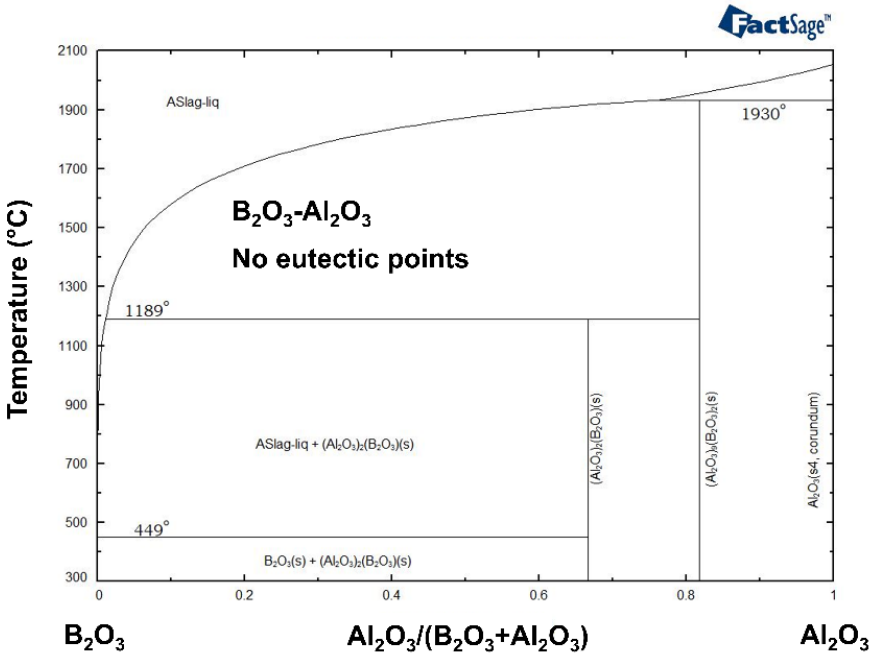

Figure 3.11: B_2O_3-Al_2O_3 binary phase diagram.

When B_2O_3 added to Al_2O_3 system (Figure 3.11), no eutectic point is observed rather, liquidus line constantly decreased with the addition of B_2O_3. Aluminum borates such as $(Al_2O_3)_2(B_2O_3)$ and $(Al_2O_3)_9(B_2O_3)$ are formed in the system. B_2O_3 addition on SiO_2 (Figure 3.12) have a eutectic point at 438 °C on 0.92 mole $SiO_2/(B_2O_3+SiO_2)$ thus, no new phase is observed from the diagram.

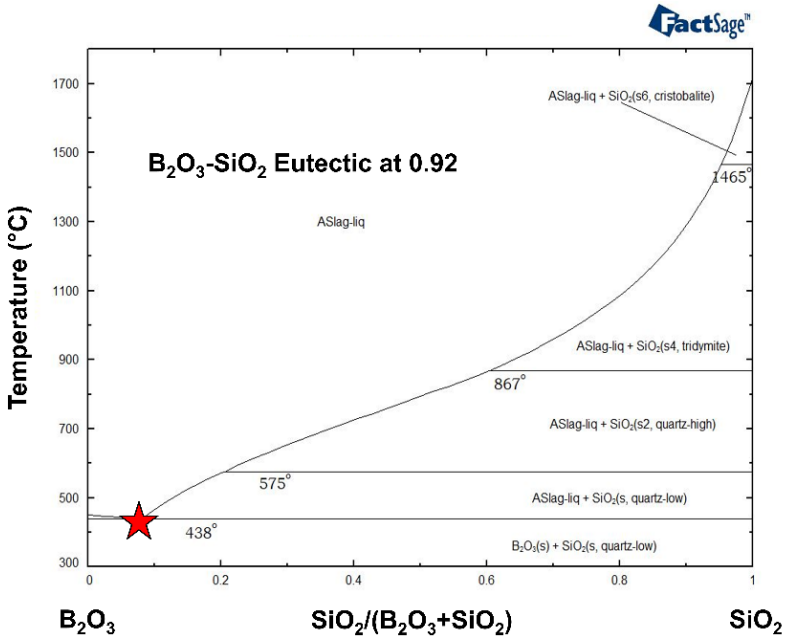

Figure 3.12: B_2O_3-SiO_2 binary phase diagram.

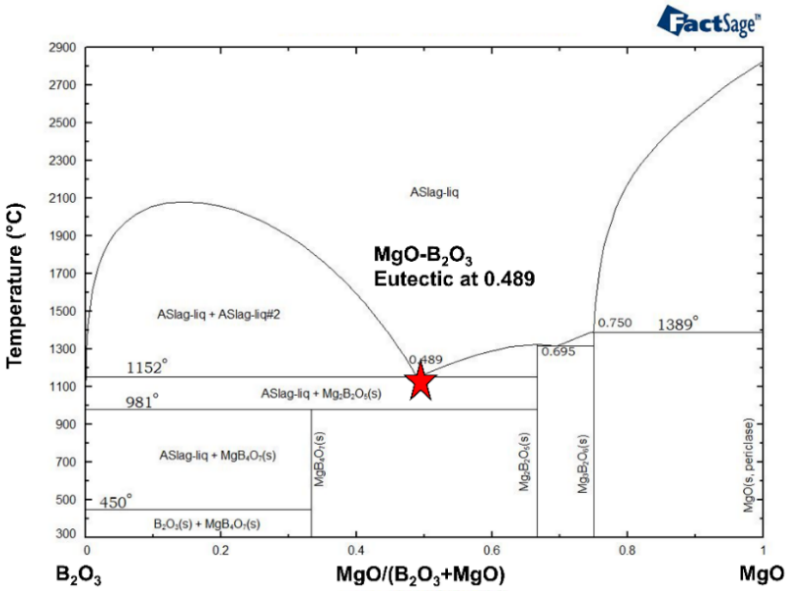

Figure 3.13: $MgO-B_2O_3$ binary phase diagram.

With B_2O_3 addition on MgO, (Figure 3.13) $Mg_2B_2O_5$ phase forms at 0.489 mole $MgO/(MgO+B_2O_3)$ addition having T_{liq} at 1150 °C.

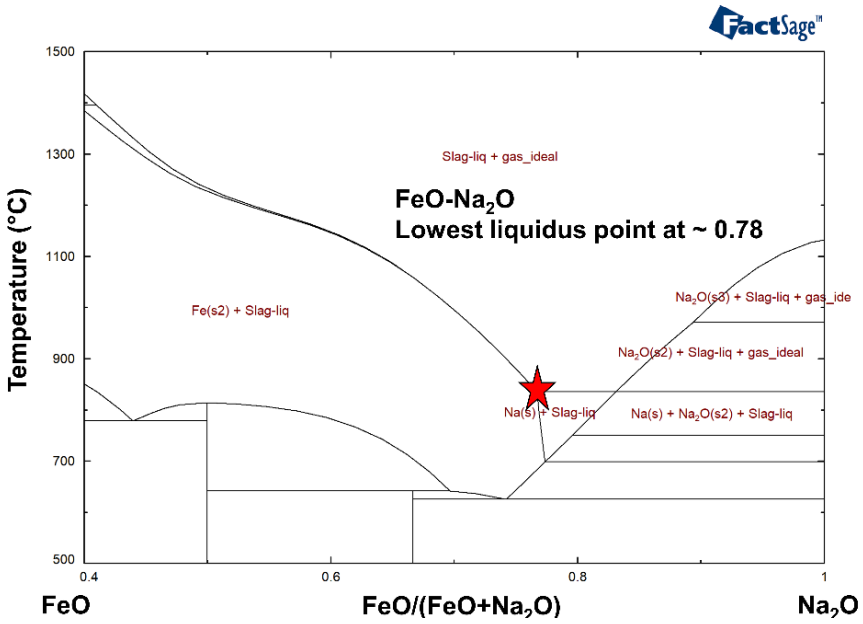

Figure 3.14: $FeO-Na_2O$ binary phase diagram.

Addition of Na_2O, CaO and B_2O_3 were also investigated despite SAC phase does not contain FeO. This choice stems from the fact that numerous non-ferrous slags have FeO as fayalite (Fe_2SiO_4) and therefore its melting behavior should also be considered. Figure 3.14

shows Na_2O addition to FeO phase, where the liquidus line decreased at 880 °C at 0.78 ($FeO/FeO+Na_2O$). Formation of intermetallic near liquidus temperature was not observed.

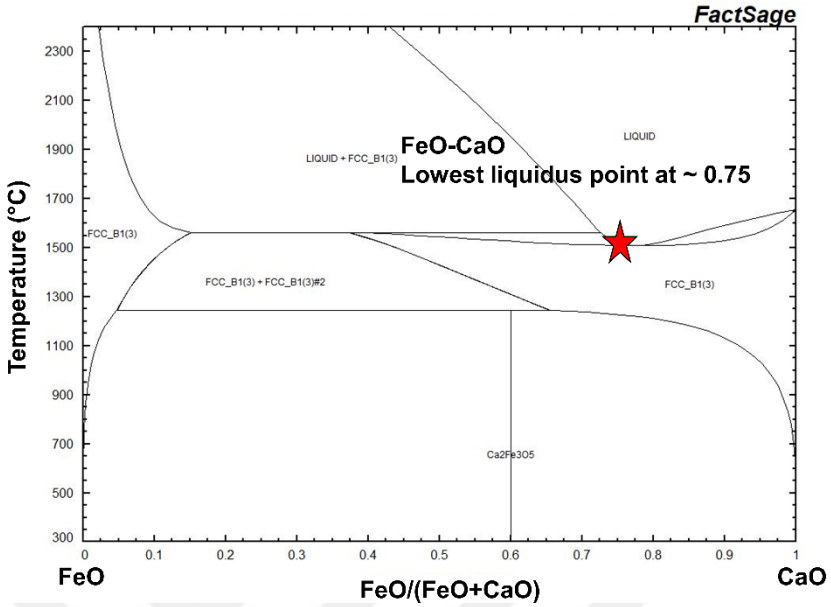

Figure 3.15: FeO-CaO binary phase diagram.

CaO addition to FeO phase (Figure 3.15), liquidus temperature significantly lowered despite the lowest temperature was ~1500 °C at 0.75 (FeO/FeO+CaO).

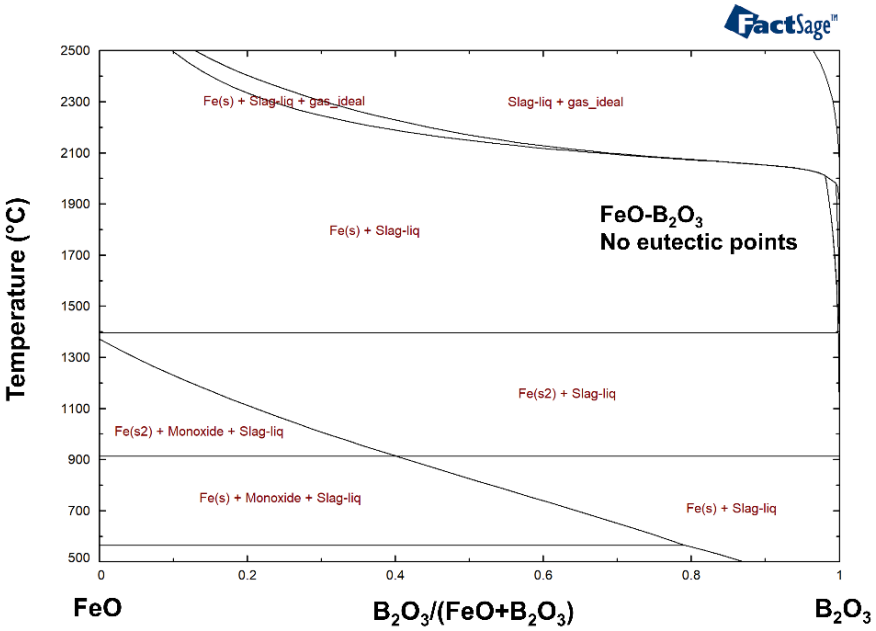

Figure 3.16: FeO-B_2O_3 binary phase diagram.

Addition of B_2O_3 to FeO phase neither any eutectic point nor the formation of intermetallics were observed from Figure 3.16. This is because dominance of covalent character over ionic character where B_2O_3 triangles connects to FeO network.

Based on the information mentioned using the binary phase diagrams, Table 3.4 summarized the eutectic points, melting temperatures and formed phases. Na_2O-Al_2O_3 and Na_2O-SiO_2 eutectics and B_2O_3-MgO eutectic presents the lowest results as 850 ˚C, 1030 ˚C and 1150 ˚C respectively. While CaO have some degree of lowering the liquidus temperature in 0.4 mole for SiO_2 and 0.36 for Al_2O_3. In the case of FeO, both CaO and Na_2O decreased the liquidus temperature where Na_2O at 0.78 (FeO/FeO+Na_2O) was formed despite, no phase formation was observed.

Table 3.4: Summarized information of various flux additions on SAC components of SiO_2-Al_2O_3-MgO-FeO.

System[b]	**Eutectic point[a] [mole%]**	**Lowest Degree [°C]**	**Eutectic phase(s)[a]**
Na_2O-SiO_2	0.75	850	$Na_6Si_8O_{19}$ + $Na_2Si_2O_5$
Na_2O-Al_2O_3	0.05	1030	Na_2O + $NaAlO_2$
Na_2O-FeO	0.22	880	FeO – Na_2O solid solution
B_2O_3-SiO_2	0.92	438	B_2O_3 + SiO_2
B_2O_3-Al_2O_3	No eutectic point	1200-1800	$(Al_2O_3)_2(B_2O_3)$ - $(Al_2O_3)_9(B_2O_3)$
B_2O_3-FeO	-	-	-
CaO-SiO_2	0.4	1700	$CaO.SiO_2$ + SiO_2
CaO -Al_2O_3	0.656	1364	$Ca_3Al_2O_6$ + $CaAl_2O_4$
CaO-FeO	0.25	1550	FeO-CaO solid solution
B_2O_3-MgO	0.5	1150	$Mg_2B_2O_5$

[a]Eutectic points and formed phases were determined from binary phase diagrams. The mole additions given in the table shows how much flux is needed to obtain designated temperature.

[b]FeO systems were also given in the table despite FeO is not present in the SAC structure. However, FeO is mainly utilized in the non-ferrous slags that must be evaluated.

According to Table 3.4, Na_2O-Al_2O_3, Na_2O-SiO_2, B_2O_3-MgO and Na_2O-FeO Eutectic points were selected compared to other systems to eliminate remaining phases in SAC structure, thereby creating a homogeneous slag.

Figure 3.17 shows the phase equilibrium diagram when the eutectic ratios of Na_2O and B_2O_3 added to SAC. Compared to only SAC diagram, $Al_2O_3.SiO_2$ and SiO_2 changes to $NaAlSiO_4$, Na_2SiO_3 and $NaAlO_2$ and $Mg_3B_2O_6$ phases where their corresponding T_m is

nearly 850 °C, 1100 °C and 800 °C respectively. All phases are incorporated into slag at 1100 °C. Whereas slag formation gradually begin at 750 °C.

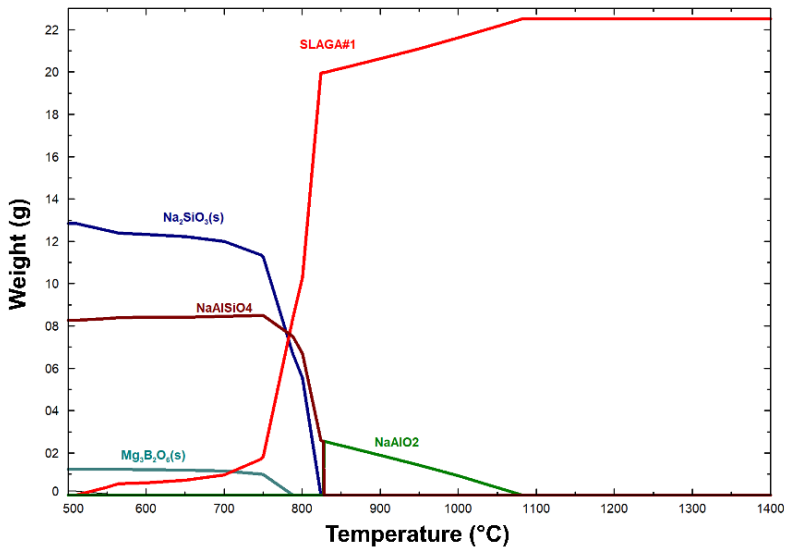

Figure 3.17: Phase equilibrium diagram of SAC at stoichiometric Na_2O and B_2O_3 addition ((0.75 SiO_2/Na_2O+SiO_2) +(0.05 $Al_2O_3/Na_2O+Al_2O_3$) +(0.5 MgO/B_2O_3+MgO)) at different temperatures.

In the case of B_2O_3 addition (Figure 3.18), $3Al_2O_3 \cdot 2SiO_2$ and SiO_2 remain in the melt though, slag formed at temperatures down to 750 °C where weight of the slag gradually increased with the temperature. However, small fractions were incorporated to slag in the range of 760 to 1400 °C. Total slag formation completes above 1400 °C. Presence of $3Al_2O_3 \cdot 2SiO_2$ and SiO_2 while gradual decrease in the slag formation temperature involves the behavior of B_2O_3 where average bond energy of SiO_2-Al_2O_3 network is decreased by the B_2O_3 triangles, lowering the Tg point. On the other hand, since B_2O_3 has not any possible reaction with the main constituent SiO_2 phase, high temperature cordieritic phases are remain the structure.

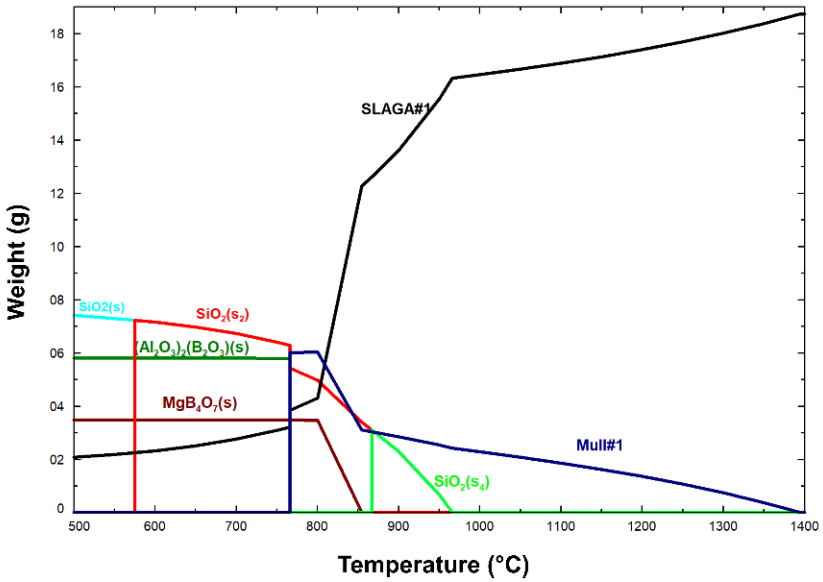

Figure 3.18: Phase equilibrium diagram of SAC and 30% B_2O_3 addition at different temperatures.

CaO addition to SAC (Figure 3.19) show that Ca based silicate and aluminates such as $CaAl_2Si_2O_8$, $Ca_2MgSi_2O_7$, $CaMgSi_2O_6$ and $CaSiO_3$ is formed. These phases are depleted at 1350 °C, 1200 °C, 1180 °C and 1150 °C respectively thus complete slag transformation occurs at 1370 °C.

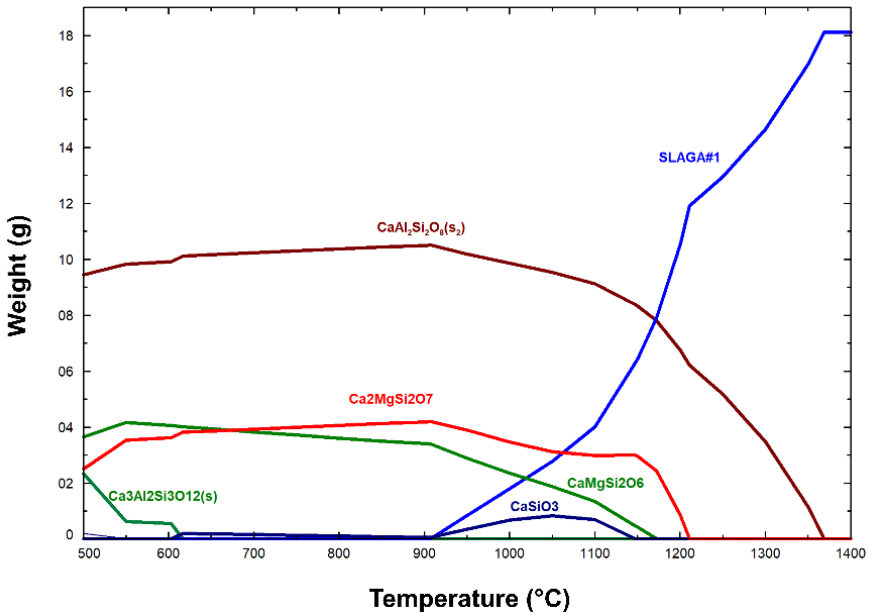

Figure 3.19: Phase equilibrium diagram of SAC and stoichiometric CaO and B_2O_3 addition ((0.6 SiO_2/CaO+SiO_2) +(0.354 Al_2O_3/CaO+Al_2O_3) +(0.5 MgO/B_2O_3+MgO)) at different temperatures.

All of the above mentioned flux additions forms variety of sodium, calcium or borate phases that have lower melting temperature than mullite and SiO_2. From the phase equilibrium diagrams, it is evident that the Na_2O addition showed the best results since no solid oxide phase is present above 1100 °C. However, it is undesireable that if fluxes reacts with one another rather than the present phases in the SAC, high temperature phases remain in the structure. For this reason, possible reactions between slag and the fluxes were calculated to investigate formation of new phases in the slag structure. The possible reactions (Eq. 3.1 – Eq. 3.13) in the system are as follows;

$$3Na_2O + 8SiO_2 \rightarrow Na_6Si_8O_{19} \quad (3.1)$$

$$Na_2O + 2SiO_2 \rightarrow Na_2Si_2O_5 \quad (3.2)$$

$$3Na_2O + B_2O_3 \rightarrow 2Na_3BO_3 \quad (3.3)$$

$$2Na_2O + Al_2O_3 \rightarrow 2NaAlO_2 \quad (3.4)$$

$$CaO + SiO_2 \rightarrow CaSiO_3 \quad (3.5)$$

$$3CaO + Al_2O_3 \rightarrow Ca_3Al_2O_6 \quad (3.6)$$

$$CaO + Al_2O_3 \rightarrow CaAl_2O_4 \quad (3.7)$$

$$CaO + B_2O_3 \rightarrow CaB_2O_4 \quad (3.8)$$

$$2FeO + SiO_2 \rightarrow Fe_2SiO_4 \quad (3.9)$$

$$FeO + Al_2O_3 \rightarrow FeAl_2O_4 \quad (3.10)$$

$$FeO + Na_2O \rightarrow Na_2FeO_2 \quad (3.11)$$

$$2Na_2O + FeO \rightarrow Na_4FeO_3 \quad (3.12)$$

$$2Al_2O_3 + B_2O_3 \rightarrow B_2Al_4O_9 \quad (3.13)$$

As shown in Figure 3.20, within the temperature range of 900–1400 °C, the Gibbs free energy of all reactions were less than zero, indicating all reaction may occur spontaneously under standard conditions.

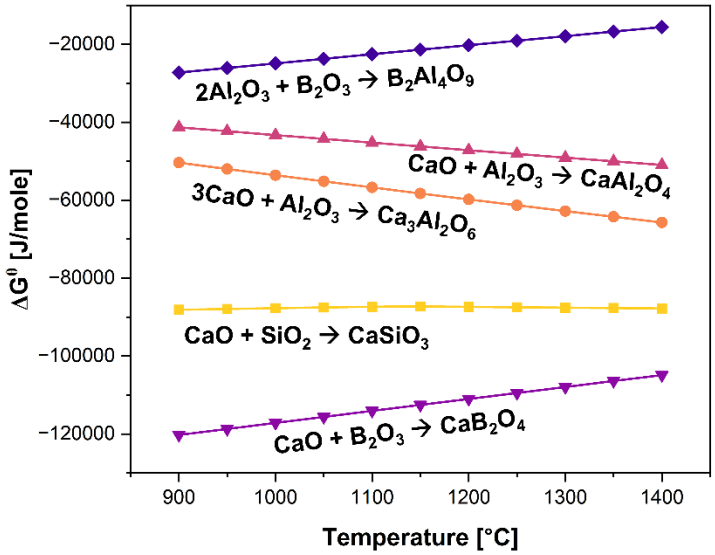

Figure 3.20: Gibbs free energy values of reactions between CaO and various metal oxides.

ΔG^{θ} of reactions between CaO and other oxides (Figure 3.20) shows that the ΔG^{θ} formation of CaB_2O_4 is lower than the $CaSiO_3$ and $Ca_3Al_2O_6$-$CaAlO_4$ that shows formation of CaB_2O_4 is more likely to occur. In other words, Ca^{2+} work as a network breaker for BO_3 triangles rather than SiO_2 tetrahedrons thus, viscosity and heterogenity of the melt will possibly remain. Whereas, in (Figure 3.21) affinity of Na^{+} to SiO_2 tetrahedrons is higher than the BO_3 triangles, which suggests a possible decrease in the viscosity.

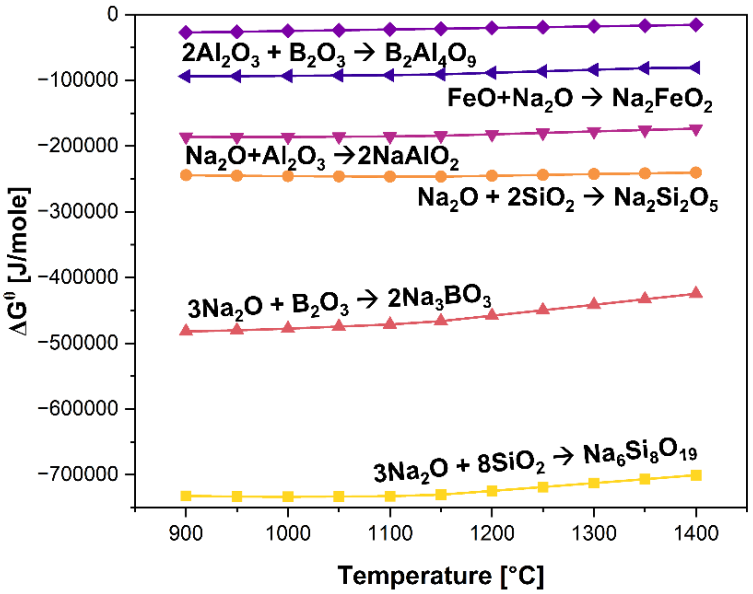

Figure 3.21: Gibbs free energy values of reactions between Na_2O and various metal oxides.[a]

[a]Al_2O_3 added to graph to compare possible depletion of B_2O_3 if Al2O3 present in the structure.

When both B_2O_3 and Na_2O added to slag composition, the affinity of Na_2O to SiO_2 phase is higher compared to B_2O_3. Thus, $NaAlO_2$ formation is more feasible than the $B_2Al_4O_9$. Therefore Na_2O could solely forms sodium based low temperature phases.

As mentioned in the phase diagram investigations, FeO does not react with B_2O_3 and CaO but form a solid solution. Therefore only Na_2O was presented in Figure 3.22. as shown in the figure, formation of Na_4FeO_3 is much higher at lower temperatures but temperature exceeding ~1280 °C, formation of $FeSiO_4$ and $FeAl_2O_4$ became possible. However, Na_2FeO_2 is the most probable phase having ΔG^{θ} of -90 kJ/mole.

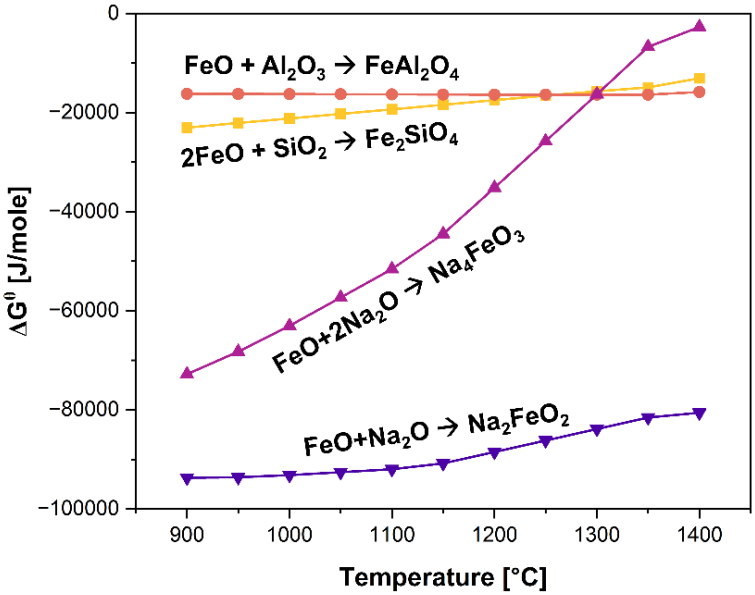

Figure 3.22: Gibbs free energy values of reactions between FeO and various metal oxides.

In the way of creating a homogenous melt, Na_2O showed the highest decrease in melting points for all the constituents (Al_2O_3, SiO_2, FeO), where slag could be made at temperatures higher than 1100 °C. In CaO addition, phase formation was observed however, total melt achieved at 1350 °C thus, using B_2O_3 togather with CaO have a negative synergistic effect since affinity of B_2O_3 is higher to CaO than SiO_2 and Al_2O_3. Where CaO reacts for B2O3 rather than the slag constituents. For this reason Na_2O-B_2O_3 fluxes are investigated further on.

3.2.2. Thermal Behavior of Slags and Viscosity

To further investigate the formation low temperature phases, thermal behavior of the SAC during melting was investigated using simultaneous thermal analysis (STA).

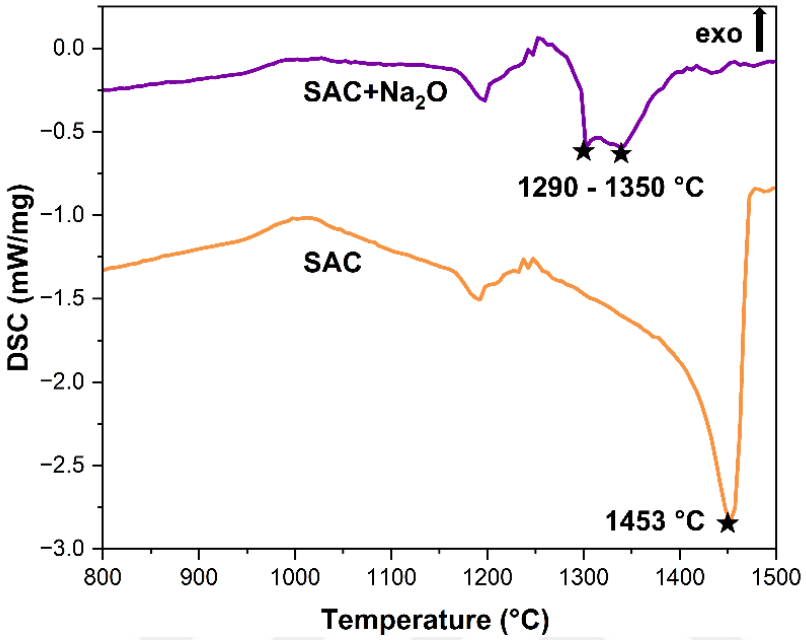

Figure 3.23: DSC curve of SAC and SAC+0.75 SiO_2/Na_2O+SiO_2, 0.05 $Al_2O_3/Na_2O+Al_2O_3$ and 0.5MgO/$MgO+B_2O_3$

DSC curve of SAC (Figure 3.23), shows a small peak at 270.7 °C corresponds to the water loss. Endothermic peak 1200 °C corresponds to melting of phase components except SiO_2, Al_2O_3 and MgO which is not taken into account while calculating phase equilibriums at (Figure 3.6). Endothermic peak at 1453 °C correspond to typical T_{liq} of the SAC which is also related to phase equilibrium diagram (Figure 3.6).

DSC curve of SAC with Na_2O addition (Figure 3.23) shows the peak at 1190 °C corresponds to melting of $NaAlO_2$. Peaks at 1290 °C and 1350 °C suggest that some silicate and aluminate phases still remain in the structure, indicating that not all Na_2O content has been fully available. Mullite and SiO_2 phases started to melt by the available Na_2O from Na_2CO_3 decomposition. Which could be the reason why the melting temperature is lower than that of T_{liq} of SAC (which is 1453 °C).

Thermal behavior of SAC when Na_2O and B_2O_3 added to slag composition in the borax ($Na_2B_4O_7$) phase (Figure 3.24). Wide endothermic peak begins after 900 °C could be related to the gradual softening or melting of different components within the slag by the addition

of B_2O_3. This phenomena occur due to bonding of low energy $[BO_3]^{3-}$ to stable structures of $[SiO_4]^{4-}$-$[SiO_4]^{4-}$ and $[SiO_4]^{4-}$- $[AlO_4]^{5-}$ decreases the overall bonding energy of the slag network. Therefore, variation of Tg value between 1000 to 1200 is clearly seen from the DSC curve of Figure 3.24 [78]. On the other hand, decrease in the melting temperature corresponds to formation of $(Al_2O_3)_2(B_2O_3)$, $NaAlSiO_4$, Na_2SiO_3, MgB_4O_7 having lower T_m than the present phases.

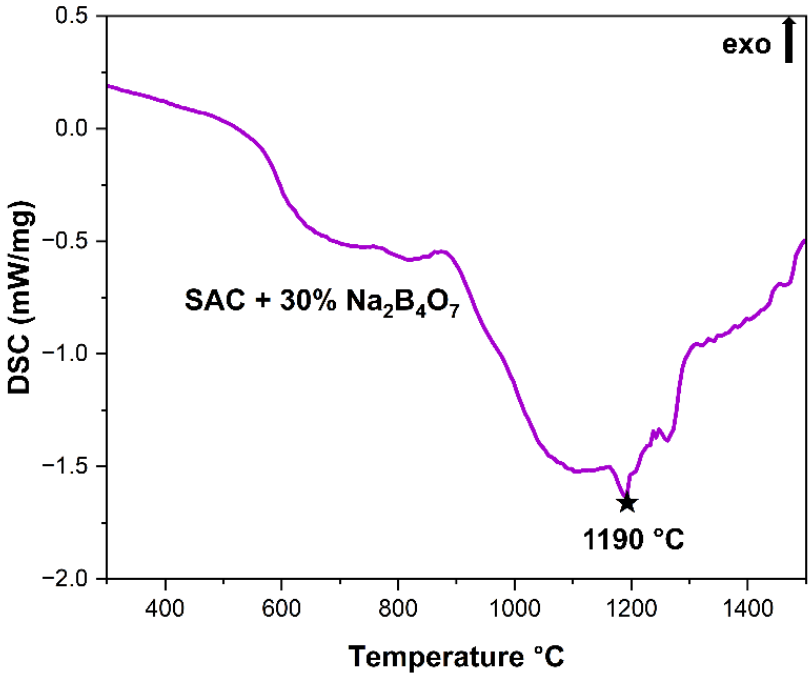

Figure 3.24: DSC curve of SAC 30% $Na_2B_4O_7$ addition.

Effect of fluxes on viscosity were calculated using the thermodynamic software FactSage. As seen from the Figure 3.25, B_2O_3 facilitates the highest decrease in viscosity than CaO and Na_2O respectively. This behavior arises due to bond-former ability of B_2O_3, where bonds are rather than being destroyed, altered by the addition of B_2O_3. Incorporation of B_2O_3 to slag network decreases the heat need to form a slag however, this value depends on the length of the previously broken $[SiO_4]^{4-}$- $[SiO_4]^{4-}$ and $[AlO_4]^{5-}$- $[SiO_4]^{4-}$ bonds by the addition of Na_2O which increased the ionic character of the slag. This behavior is seen from the DSC curves as the Tg value varies in a range of 900 to 1200 °C. This phenomena therefore leading to reduction in viscosity which obliges to use B_2O_3 in the slag composition. However, its important to mention that there are several reports suggesting excessive introduction of boron ions (B^{3+}) in the silicate network lead to the development

of $[BO_4]^{5-}$ tetrahedron structure instead of the $[BO_3]^{3-}$ planar triangular structure within the silicate system, which eventually increasing viscosity of the slag [78].

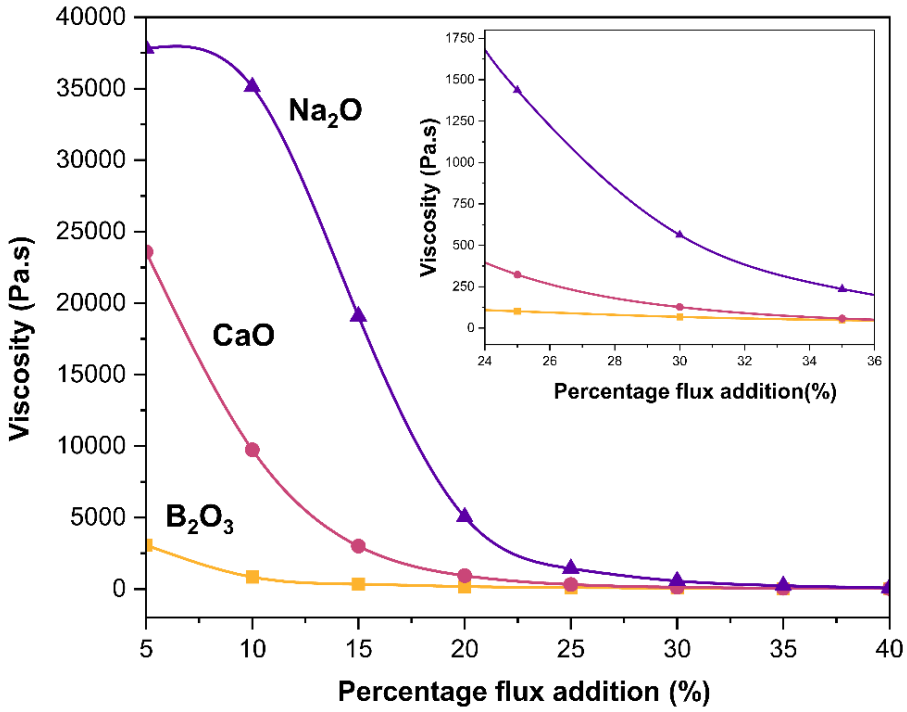

Figure 3.25: Effect of flux addition to spent catalyst composition ($0.55SiO_2$. $0.31Al_2O_3$.0.06MgO) on viscosity at 1250 °C. Inset presenting the part of the graph between flux addition 24% to 36%.

3.2.3. Implications on Slag Optimization

From slag optimization experiments, a schematic representation (Figure 3.26) was made to summarize the implications. When basic oxides such as Na_2O and CaO added to slag system, (Figure 3.26a) low melting temperature phases such as sodium/calcium silicates and aluminates forms thus ionic character of the slag increases. After the Tg has exceeded and homogenous melt is formed, these oxides behave as "network modifiers" which breaks the $[SiO_4]^{4-}$- $[SiO_4]^{4-}$ and $[SiO_4]^{4-}$- $[AlO_4]^{5-}$ bond due to their high oxygen bonding capacity. This breakage results in shorter network lengths that decrease the melting temperature and viscosity of the slag. On the other hand, B_2O_3 is a known "network former" that could join the silica-alumina network as represented in Figure 3.26b. When probability of $[BO_3]^{3-}$ - $[SiO_4]^{4-}$ and $[BO_3]^{3-}$ - $[AlO_4]^{5-}$ bonds increases, due to lowered bond energy in the overall structure, viscosity decreases even higher than the addition of basic oxides as shown in the viscosity evaluation Figure 3.25. On the other hand, affinity of Na_2O and B_2O_3 fluxes to

slag species (Al_2O_3, SiO_2) is much higher than the CaO, where it is more likely to bond B_2O_3 rather than those species as stated in Figure 3.20.

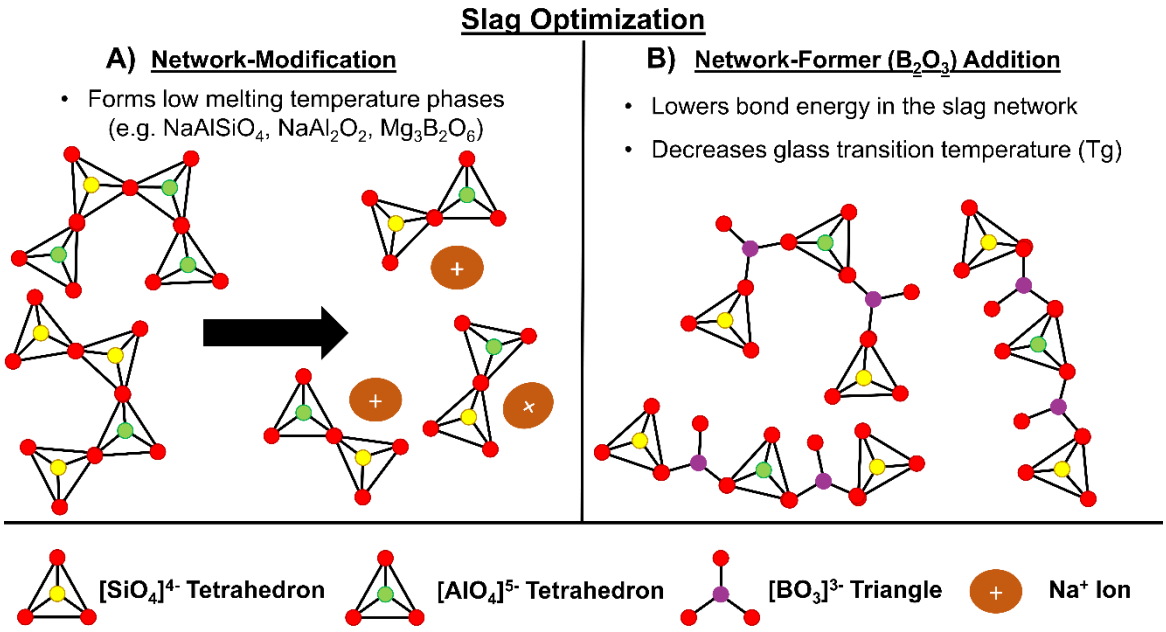

Figure 3.26: Illustration of slag optimization made in this work. (a) Shows the effect of network-modifier oxides in the slag network. (b) Effect of network-former addition on slag network.

In conclusion, the optimal ratios of Na_2O and B_2O_3, resulting in the lowest liquidus temperature, are employed for both Al_2O_3 and SiO_2 percentages in the slag, which corresponds to 0.75 SiO_2/Na_2O+SiO_2, 0.05 $Al_2O_3/Na_2O+Al_2O_3$, 0.5 MgO/B_2O_3+MgO respectively in order to achieve a homogenous melt. Additionally, from viscosity calculations, %30 B_2O_3 is selected to lower the viscosity of slag.

3.2.4. Metal Recovery Experiments

To investigate efficiency of the slag optimization methodology which is proposed in this work, Cu slag was mixed with 0.22 FeO/Na_2O+SiO_2, 0.75SiO_2/Na_2O+SiO_2 and %30 B_2O_3, where Na_2O is added to create a homogenous slag while B_2O_3 added to decrease viscosity and to obtain glass phase. Table 3.5 shows the recovery efficiency of Cu, before and after the treatment.

Table 3.5: Cu and S content of fayalite slag before and after metal recovery procedure.

Number of samples		Initial Cu concentration				After Metal Recovery			
		1	2	3	4	1	2	3	4
%[a] [w/w]	Cu	1.49	0.92	1.16	1.18	0.243	0.127	0.118	0.131
	S	1.22	1.10	1.09	1.015	0.613	0.652	0.705	0.639

[a]Weight percentage was determined using a XRF.

Metal concentration of SAC before and after metal recovery experiment is given on Table 3.6 when 0.75 SiO_2/Na_2O+SiO_2, 0.05 $Al_2O_3/Na_2O+Al_2O_3$, 0.5 MgO/B_2O_3+MgO and %30 B_2O_3 of Na_2O and B_2O_3 added to slag mixture. It is important to note that the minimum metal concentrations determined by the XRF could not exceeded to <0.002% where the accurate efficiency could be lower than the current results.

Table 3.6 Pt, Pd and Ce concentration of SACs before and after metal recovery treatment.

Number of samples		Initial metal concentration			After metal recovery		
		1	2	3	1	2	3
%[a] [w/w]	Pt	0.026	0.027	0.032	<0.002	<0.002	<0.002
	Pd	0.003	0.004	0.005	<0.002	<0.002	<0.002
	Ce	0.061	0.08	0.098	0.022	0.044	0.042

[a]Weight percentage was determined using a XRF.

Table 3.7 shows the Cu, Ag and Pt concentration of jewelery slag when 30% B_2O_3 is added to slag. Ag and Cu showed a relatable decrease in the slag content while nearly no Pt were collected on the metal phase.

Table 3.7: Cu, Ag and Pt concentration of waste jewelery slag, before and after metal recovery experiment.

Number of samples		Initial metal concentration			After metal recovery		
		1	2	3	1	2	3
%[a] [w/w]	Cu	4.75	3.59	4.321	0.687	0.545	0.526
	Ag	0.307	0.422	0.512	0.008	0.006	0.005
	Pt	0.033	0.022	0.012	0.015	0.021	0.024

[a]Weight percentage was determined using a XRF.

Table 3.8 shows the recovery efficiency from selected slags and secondary metal sources. From the results it can be said that over 92.94% Pt was recoverd from SAC while 83.16% for Cu flash furnace and Ag – 98.48% and Cu - 84.77% for jewelry slag were achieved.

Table 3.8: Summarized metal recovery efficiency taken from Table 3.6-3.9.

Slag Name	Recovery Efficiency [%]
Spent Auto-catalyst	Pt – 92.94%
Cu flash furnace slag	Cu – 83.16%
jewelery waste slag	Ag – 98.48% Cu - 84.77

Cu recovery became as high as %85 could be the result of sulfidic or oxidic dissolved Cu, where could not be recovered by the metal-slag seperation. On other reason so support Cu is not in metallic form up to 15% is the high recovery of Pt and Ag from the slag phases. Herein this work, a simple but effective slag methodology which could be adapted to various slags having SiO_2, Al_2O_3, MgO and FeO inside its composition. With the flux usage as low as 60% (percentage equal of mole ratios) is believed to be an important parameter for both industrial scale adaptability and recovery efficiency which lead to higher volumes.

3.3.Arc Smelting Trials

During arc smelting, the resistance of the melt environment constantly changes thus, it is challenging to maintain a continuous arc. Continuous arc formation is crucial for efficient smelting and electrode consumption and therefore an automation system is needed to control the arc formation.

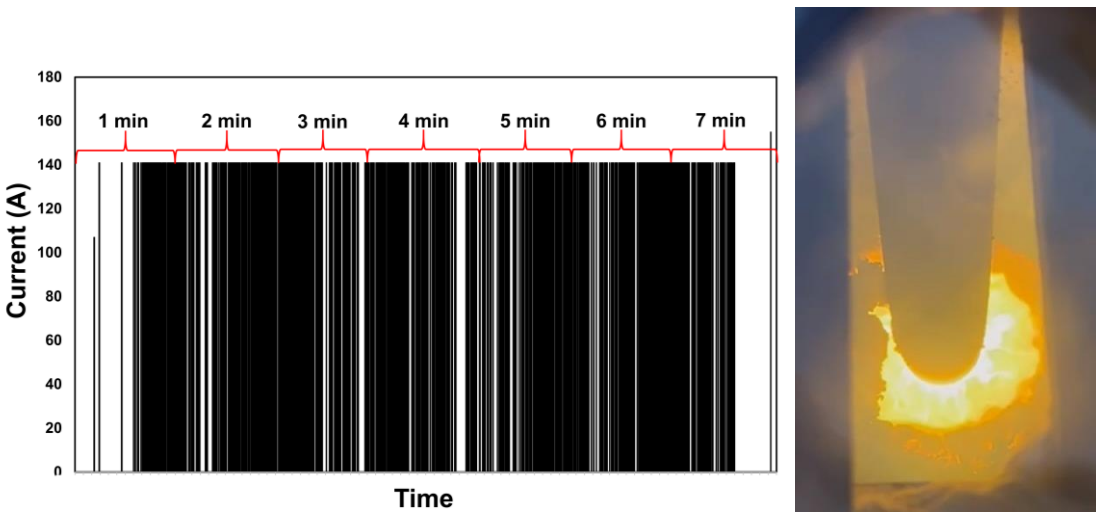

Figure 3.27: Arc continuity graph of EAF system at 140 A in 1 min time intervals. (a) Photograph taken during the arc smelting trials. (b)

Figure 3.27b shows the arc continuity at 140 A in 1 minute intervals. Initially electrode adjust itself to gain reponse as a current thus after the adjusting stage continuous arc is formed despite small breaks during the smelting. At that stage, resistance of the

environment which is attributed to gas formation, charging of materials temperature and electrode arc points. For this reason, a continuous arc is achieved through automation. When the first arc is formed, the motion system stops upon detecting the initial current data indicating the flow of current through the electrodes. Throughout the operation of the electrode motion system, current and electrode distance data are recorded at intervals of 1 millisecond. When the arc ceases, the motion system raises the electrode and subsequently lowers it until the first current begins to flow through the system again. In Figure 3.27a, a photograph captured during arc smelting distinctly illustrates the formation of arcs, appearing as conspicuous white waves. Figure 3.28 shows the sensitivity of the system where arc formation can be achieved in matter of seconds.

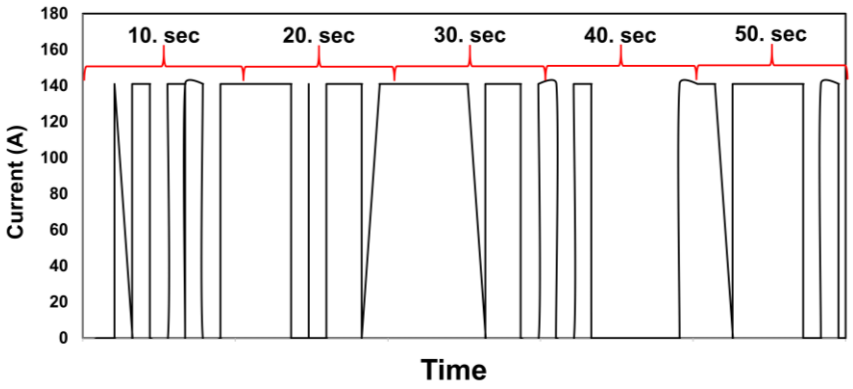

Figure 3.28: Arc continuity graph of EAF system at 140 A in 10 sec. time intervals.

Smelting experiments were made by three different slag specimen; a) Spent auto catalyst (SAC) b) Cu flash furnace slag and b) jewelery waste slag. Main characteristics of SAC were shown in Figure 3.1 and Table 3.1.

4. CONCLUSION

In this study, a pyrometallurgical process was developed to efficiently separate metal from slag, with a specific focus on recovering valuable metals trapped in various sources like Cu flash furnace slag, jewelry waste slag and PGM-containing spent auto-catalytic converters. The process involved the design and construction of a direct-current (DC) electric arc furnace (EAF) chosen for its capability to rapidly reach high temperatures (1800 °C), providing the necessary heat to melt the slag phase and reduce its viscosity due to the elevated temperature.

A pyrometallurgical process for efficient metal/slag seperation was designed especially to recover valuable metal that are trapped in various sources such as Cu flash furnace slag, jewelery waste containing jewelery waste slag and PGM containing spent auto-catalytic convertor. In the process, a direct-current (DC) electric arc furnace (EAF) was designed and constructured owing to its ability to reach high temperatures (1800 °C) in short time that could supply the heat required to melt the slag phase and decrease its viscosity due to high temperature. During the DC-EAF construction:

- A hearth design was made through heat transfer calculations where inner crucible could withstand high temperatures as maximum as 1800 °C. For this reason inner hearth was made using high purity Al_2O_3 castable while outer hearth was made using MgO bricks and Al_2O_3-ZrO cement. According to heat transfer calculations, outer steel casing could reach temperatures high as 425 °C and therefore a cooling system was utilized for both electrodes and steel casing.
- A electrode motion system having two step-motors which are connected in two axes was constructed for electrode motion. During the smelting, continuous arc formation is essential reach high temperatures as quickly as possible. However, resistance of the smelting environment constantly changes by the temperature, presence of solid and liquid phases. Therefore, arc formation should be controlled using an automation system, that could utilize both voltage and electrode to electrode distance (or arc length). Continous arc formation were investigated by

measuring the current versus time graph, were suggest arc generally present despite small shortcuts at which automation was activited.

- A power source with an AC to DC rectifier and electrode system was also made to supply the energy needed for arc smelting.
- A mechanical tilting system was also constructed for simple tapping of the system.

To increase to efficency of metal recovery from slag phase, it is important to decrease the overall liquidus temperature and obtaining a homogenous melt while achieving low viscosity. For this reason, initially slag specimens were characterized using X-ray diffraction (XRD), X-ray fluorescence (XRF). SACs were mainly made by cordierite, a phase region which includes high percent of SiO_2, Al_2O_3 and MgO, Cu flash furnace slag is mainly composed of FeO.SiO based fayalite slag while, jewelry waste slag is high on PbO due to cuppelation process that is used for collecting metal phase in lead. Slag optimization was made and explained using SAC phase due to its high melting temperature and acidic oxide composition which is believed to the difficult to smelt relative to Cu and jewelery slag. In slag optimization investigations thermodynamical calculations were made as follows:

- Binary phase diagrams of SiO_2, Al_2O_3, MgO and FeO together with flux additions (CaO, Na_2O, B_2O_3) were investigated and possible formation of low temperature phases, eutectics and low liquidus temperatures were determined.
- Phase-equilibrium diagrams of SAC phase with flux additions Na_2O, CaO, B_2O_3 (stoichiometries determined by binary phase diagrams) were calculated. Results have shown without any flux addition, SAC phase could melt and form slag at 1453 °C despite high temperature mullite and SiO_2 phases still present in the structure. Na_2O addition ((0.75 SiO_2/Na_2O+SiO_2) and (0.05 $Al_2O_3/Na_2O+Al_2O_3$)) froms $NaAlO_2$, $NaAlSiO_4$ and Na_2SiO_3 phases thus total slag formation temperature was achieved at 1100 °C. Addition B_2O_3 (0.5 MgO/B_2O_3+MgO) to SAC formed $Mg_3B_2O_6$ at low temperature as ~ 500 °C. When only %30 (w/w) B2O3 added to system, slag temperature drastically decreased to 900 °C despite mullite and SiO_2 still present in the structure. Decrease in the slag formation temperature is linked to the behavior of B_2O_3, which reduces the average bond energy of the SiO_2-Al_2O_3 network, consequently lowering the Tg point. Conversely, B_2O_3 does not react with the main SiO_2 phase, allowing high-temperature cordieritic phases to maintain their

structure. On the other hand addition of CaO, ((0.6 $SiO_2/CaO+SiO_2$) and (0.354 $Al_2O_3/CaO+Al_2O_3$) creates calcium-based silicate and aluminates, including $CaAl_2Si_2O_8$, $Ca_2MgSi_2O_7$, $CaMgSi_2O_6$ and $CaSiO_3$, are generated At temperatures of 1350 °C, 1200 °C, 1180 °C and 1150 °C. These phases experience depletion at their respective temperatures, culminating in the comprehensive transformation of the slag at 1370 °C.

- Reaction feasibilities between fluxes and the slag phases were investigated by calculating Gibbs free energy (ΔG^{θ}) of the reactions. Results have shown that when using CaO togather with B_2O_3 forms CaB_2O_4 rather than calcium silicate and aluminate phases which does not affect the slag properties. Whereas Na2O is mostly reacts with SiO_2, forming $Na_6Si_8O_{19}$ despite formation of sodium borate species are more feasible then $NaAlO_2$. When both Na_2O and B_2O_3 utilized as flux in metal recovery process, its important to add Na_2O to form low temperature phases where B_2O_3 added to melt after the formation of slag to decrease its viscosity. FeO have no reaction between both B_2O_3 and CaO however, when Na_2O is added to FeO contained system, formation energy of Na_2FeO_2 is much higher than the Fe_2SiO_4 until the system temperature exceeding ~1280 °C, Fe_2SiO_4 and $FeAl_2O_4$ forms again.
- Thermal behavior of possible slag compositions were investigated using differential scanning calorimetry (DSC). DSC of only SAC phase have an endothermic peak at 1453 °C that corresponds to slag formation temperature.
- When ((0.75 SiO_2/Na_2O+SiO_2) and (0.05 $Al_2O_3/Na_2O+Al_2O_3$)) is added to SAC, melting temperature decreases to 1290 to 1370 °C Peaks detected at 1299 °C and 1350 °C imply the persistence of certain silicate and aluminate phases in the structure, indicating that not all Na_2O content has been completely utilized or made available at those temperatures due to decomposition of Na_2CO_3 to Na_2O
- When 30% $Na_2B_4O_7$ is added to the SAC, endothermic peak decreases to 1190 °C, which may suggest the melting temperature of sodium silicate and aluminate phases while the boardening of the endothermic peak between 850 °C to 1500 °C is due to connection of B_2O_3 to silicate network of the slag where its Tg varies with the temperature.

- Viscosity of SAC when different fluxes were added to system was also calculated. Results have shown that the B_2O_3 made the most drastic decrease an even in low additions (5% - 10%) slag viscosity decrease to 125 Pa.s.
- When calculated flux ratios, (0.75 SiO_2/Na_2O+SiO_2, 0.05 $Al_2O_3/Na_2O+Al_2O_3$ $0.5MgO/MgO+B_2O_3$ and 30% B_2O_3) added to SAC, (0.22 $FeO/FeO+Na_2O$ and 30% B_2O_3) added to Cu flash furnace slag while only 30% B_2O_3 added to jewelery slag. Recovery efficiencies were determined as <92% Pt and Pd for SAC, <83.16% Cu for Cu flash furnace slag and 98.47% Ag and 84.77% Cu for waste jewelery slag was achieved.

In slag optimization studies it was concluded that the Na_2O and CaO give rise to low-temperature phases like sodium/calcium silicates and aluminates before the formation of slag. Once the glass transition temperature (Tg) is surpassed and a homogeneous melt is established, these oxides act as "network modifiers." They disrupt the $[SiO_4]^{4-}$-$[SiO_4]^{4-}$ and $[SiO_4]^{4-}$ - $[AlO_4]^{5-}$ bonds owing to their high oxygen bonding capacity, resulting in shorter network lengths. This, in turn, decreases the melting temperature and viscosity of the slag. On the contrary, B_2O_3 acts as a recognized "network former" that can integrate into the silica-alumina network. As the probability of $[BO_3]^{3-}$ - $[SiO_4]^{4-}$ and $[BO_3]^{3-}$ - $[AlO_4]^{5-}$ bonds increases, due to reduced bond energy in the overall structure, viscosity decreases even more than with the addition of basic oxides. This study aims to endeavor the development of a generalized process for metal recovery from slag phases. It combines high-temperature smelting and introduces a slag optimization methodology to decrease melting temperature and viscosity. The goal is to use a low volume of flux, a factor crucial for both enhancing recovery efficiency and facilitating the industrial adaptation of the process

REFERENCES

[1] **I.-K. Suh, Y. Waseda, and A. Yazawa,** "Some Interesting Aspects of Non-ferrous Metallurgical Slags," *High Temp. Mater. Process.*, vol. 8, no. 1, pp. 65–88, Sep. 1988, doi: 10.1515/HTMP.1988.8.1.65.

[2] **J. J. Moore and E. A. Boyce,** *Chemical metallurgy*, 2nd ed. London Boston: Butterworths, 1990.

[3] **G. Liang and Z. Qu,** "Insight into Pyrometallurgical Recovery of Platinum Group Metals from Spent Industrial Catalyst: Co-disposal of Industrial Wastes," *ACS EST Eng.*, Jul. 2023, doi: 10.1021/acsestengg.3c00129.

[4] **G. A. Brooks, M. M. Hasan, and M. A. Rhamdhani,** "Slag Basicity: What Does It Mean?," in *10th International Symposium on High-Temperature Metallurgical Processing*, T. Jiang, J.-Y. Hwang, D. Gregurek, Z. Peng, J. P. Downey, B. Zhao, O. Yücel, E. Keskinkilic, and R. Padilla, Eds., in The Minerals, Metals & Materials Series. Cham: Springer International Publishing, 2019, pp. 297–308. doi: 10.1007/978-3-030-05955-2_28.

[5] **W. Vogel**, Ed., *Glass Chemistry*. Berlin, Heidelberg: Springer Berlin Heidelberg, 1994. doi: 10.1007/978-3-642-78723-2.

[6] **J. Muller, J. Zietsman, and P. Pistorius,** "Modeling of Manganese Ferroalloy Slag Properties and Flow During Tapping," *Metall. Mater. Trans. B*, vol. 46, Jul. 2015, doi: 10.1007/s11663-015-0426-7.

[7] **N. M. Piatak and E. Vojtech,** "Introduction: Metallurgical Slags – Environmental Liability or Valuable Resource?," in *Metallurgical Slags: Environmental Geochemistry and Resource Potential*, in Chemistry in Environment, no. 2. , Royal Society of Chemistry, 2021.

[8] **I. Bellemans, E. De Wilde, N. Moelans, and K. Verbeken,** "Metal losses in pyrometallurgical operations - A review," *Adv. Colloid Interface Sci.*, vol. 255, pp. 47–63, May 2018, doi: 10.1016/j.cis.2017.08.001.

[9] **M. Benson, C. R. Bennett, M. K. Patel, J. E. Harry, and M. Cross,** "Collector-metal behaviour in the recovery of platinum-group metals from catalytic converters," *Miner. Process. Extr. Metall.*, vol. 109, no. 1, pp. 6–10, Apr. 2000, doi: 10.1179/mpm.2000.109.1.6.

[10] **S. S. Dukhin, G. Kretzschmar, and R. Miller,** *Dynamics of Adsorption at Liquid Interfaces: Theory, Experiment, Application*. Elsevier, 1995.

[11] **D. Poggi, R. Minto, and W. G. Davenport,** "Mechanisms of Metal Entrapment in Slags," *JOM*, vol. 21, no. 11, pp. 40–45, Nov. 1969, doi: 10.1007/BF03378796.

[12] **S.-H. Seok, S.-M. Jung, Y.-S. Lee, and D.-J. Min,** "Viscosity of Highly Basic Slags," *ISIJ Int.*, vol. 47, no. 8, pp. 1090–1096, 2007, doi: 10.2355/isijinternational.47.1090.

[13] **K. O. Fagerlund and H. Jalkanen,** "Microscale simulation of settler processes in copper matte smelting," *Metall. Mater. Trans. B*, vol. 31, no. 3, pp. 439–451, Jun. 2000, doi: 10.1007/s11663-000-0150-8.

[14] **J. M. Toguri and N. H. Santander,** "Distribution of copper between Cu-Au alloys and silica-saturated fayalite slags," *Metall. Trans.*, vol. 3, no. 2, pp. 590–592, Feb. 1972, doi: 10.1007/BF02642068.

[15] **L. Andrews,** "Base metal losses to furnace slag during processing of platinum-bearing concentrates," Apr. 2009, Accessed: Dec. 15, 2023. [Online]. Available: https://repository.up.ac.za/handle/2263/24503

[16] **R. J. C. Billington F. D.,** "Copper and silver in silicate slags.," *Trans Inst Min Met. 59*, vol. 3, pp. 273–297, 1956.

[17] **P. J. Mackey,** "The Physical Chemistry of Copper Smelting Slags—A Review," *Can. Metall. Q.*, vol. 21, no. 3, pp. 221–260, Jul. 1982, doi: 10.1179/cmq.1982.21.3.221.

[18] **S. I. Imris. F.,** "Slags from continuous copper production.," presented at the Proc. Internat. Symposium on Advances in Extractive Metallurgy and Refining, Institution of Mining and Metallurgy, London, 1972, pp. 39–77.

[19] **M. Nagamori,** "Metal loss to slag: Part I. Sulfidic and oxidic dissolution of copper in fayalite slag from low grade matte," *Metall. Trans.*, vol. 5, no. 3, pp. 531–538, Mar. 1974, doi: 10.1007/BF02644646.

[20] **R. Sridhar, J. M. Toguri, and S. Simeonov,** "Copper losses and thermodynamic considerations in copper smelting," *Metall. Mater. Trans. B*, vol. 28, no. 2, pp. 191–200, Apr. 1997, doi: 10.1007/s11663-997-0084-5.

[21] **A. Habib, H. N. Bhatti, and M. Iqbal,** "Metallurgical Processing Strategies for Metals Recovery from Industrial Slags," *Z. Für Phys. Chem.*, vol. 234, no. 2, pp. 201–231, Feb. 2020, doi: 10.1515/zpch-2019-0001.

[22] **S. Ndlovu, G. S. Simate, and E. Matinde,** *Waste Production and Utilization in the Metal Extraction Industry*, 1st ed. Boca Raton : Taylor & Francis, CRC Press, 2017.: CRC Press, 2017. doi: 10.1201/9781315153896.

[23] **G.-H. Zheng and J. A. Kozinsk,** "Solid waste remediation in the metallurgical industry: Application and environmental impact," *Environ. Prog.*, vol. 15, no. 4, pp. 283–292, 1996, doi: 10.1002/ep.670150419.

[24] **C. Shi,** "Characteristics and cementitious properties of ladle slag fines from steel production," *Cem. Concr. Res.*, vol. 32, no. 3, pp. 459–462, Mar. 2002, doi: 10.1016/S0008-8846(01)00707-4.

[25] **M. Reuter, Y. Xiao, and U. Boin,** "Recycling and environmental issues of metallurgical slags and salt fluxes," *VII Int. Conf. Molten Slags Fluxes Salts*, pp. 349–356, Jan. 2004.

[26] **"Properties," Euroslag.** Accessed: Dec. 15, 2023. [Online]. Available: https://www.euroslag.com/products/properties/

[27] **"Chemical characteristics of iron and steel slag : NIPPON SLAG ASSOCIATION."** Accessed: Dec. 15, 2023. [Online]. Available: https://www.slg.jp/e/slag/character.html

[28] **H. Yi, G. Xu, H. Cheng, J. Wang, Y. Wan, and H. Chen,** "An Overview of Utilization of Steel Slag," *Procedia Environ. Sci.*, vol. 16, pp. 791–801, Dec. 2012, doi: 10.1016/j.proenv.2012.10.108.

[29] **I. Z. Yildirim and M. Prezzi,** "Chemical, Mineralogical, and Morphological Properties of Steel Slag," *Adv. Civ. Eng.*, vol. 2011, p. e463638, Oct. 2011, doi: 10.1155/2011/463638.

[30] J**. Waligora, D. Bulteel, P. Degrugilliers, D. Damidot, J. L. Potdevin, and M. Measson,** "Chemical and mineralogical characterizations of LD converter steel slags: A multi-analytical techniques approach," *Mater. Charact.*, vol. 61, no. 1, pp. 39–48, Jan. 2010, doi: 10.1016/j.matchar.2009.10.004.

[31] **B. Das, S. Prakash, P. S. R. Reddy, and V. N. Misra,** "An overview of utilization of slag and sludge from steel industries," *Resour. Conserv. Recycl.*, vol. 50, no. 1, pp. 40–57, Mar. 2007, doi: 10.1016/j.resconrec.2006.05.008.

[32] **M. Tossavainen, F. Engstrom, Q. Yang, N. Menad, M. Lidstrom Larsson, and B. Bjorkman,** "Characteristics of steel slag under different cooling conditions," *Waste Manag.*, vol. 27, no. 10, pp. 1335–1344, Jan. 2007, doi: 10.1016/j.wasman.2006.08.002.

[33] **C. Shi,** "Steel Slag—Its Production, Processing, Characteristics, and Cementitious Properties," *J. Mater. Civ. Eng.*, vol. 16, no. 3, pp. 230–236, Jun. 2004, doi: 10.1061/(ASCE)0899-1561(2004)16:3(230).

[34] **H. Shen, E. Forssberg, and U. Nordström,** "Physicochemical and mineralogical properties of stainless steel slags oriented to metal recovery," *Resour. Conserv. Recycl.*, vol. 40, no. 3, pp. 245–271, Feb. 2004, doi: 10.1016/S0921-3449(03)00072-7.

[35] **J. Setién, D. Hernández, and J. J. González,** "Characterization of ladle furnace basic slag for use as a construction material," *Constr. Build. Mater.*, vol. 23, no. 5, pp. 1788–1794, May 2009, doi: 10.1016/j.conbuildmat.2008.10.003.

[36] **H. Shen and E. Forssberg,** "An overview of recovery of metals from slags," *Waste Manag.*, vol. 23, no. 10, pp. 933–949, Jan. 2003, doi: 10.1016/S0956-053X(02)00164-2.

[37] **F. López, A. López-Delgado, and N. Balcazar,** "Physico-chemical and mineralogical properties of EAF and AOD Slags," *Afinidad*, vol. 53, pp. 39–46, Jan. 1996.

[38] **F. Habashi,** *Handbook of Extractive Metallurgy, Volume 2*, vol. Two. 1997. Accessed: Dec. 04, 2023. [Online]. Available: https://works.bepress.com/fathi_habashi/22/

[39] **N. M. Piatak, M. B. Parsons, and R. R. Seal,** "Characteristics and environmental aspects of slag: A review," *Appl. Geochem.*, vol. 57, pp. 236–266, Jun. 2015, doi: 10.1016/j.apgeochem.2014.04.009.

[40] **A. Kilicarslan and M. N. Saridede,** "Treatment of Industrial Brass Wastes for the Recovery of Copper and Zinc," *Sep. Sci. Technol.*, vol. 50, no. 2, pp. 286–291, Jan. 2015, doi: 10.1080/01496395.2014.952304.

[41] **A. Potysz, E. van Hullebusch, J. Kierczak, M. Grybos, P. N. L. Lens, and G. Guibaud,** "Copper Metallurgical Slags – Current Knowledge And Fate: A Review," *Crit. Rev. Environ. Sci. Technol.*, vol. 45, May 2015, doi: 10.1080/10643389.2015.1046769.

[42] **H. S. Altundoğan and F. Tümen,** "Metal recovery from copper converter slag by roasting with ferric sulphate," *Hydrometallurgy*, vol. 44, no. 1, pp. 261–267, Jan. 1997, doi: 10.1016/S0304-386X(96)00038-2.

[43] **P. K. Gbor, V. Mokri, and C. Q. Jia,** "Characterization of smelter slags," *J. Environ. Sci. Health Part A*, vol. 35, no. 2, pp. 147–167, Feb. 2000, doi: 10.1080/10934520009376960.

[44] **C. D. Barnes, I. Lumsdaine, and 'Hare S. M. O,** "Copper converter slag treatment at Mount Isa Mines Limited, Mount Isa, Qld.," *AESIS*, p. 31, Jan. 1993, doi: 10.3316/aesis.199402099.

[45] **O. Herreros, R. Quiroz, E. Manzano, C. Bou, and J. Viñals,** "Copper extraction from reverberatory and flash furnace slags by chlorine leaching," *Hydrometallurgy*, vol. 49, no. 1, pp. 87–101, Jun. 1998, doi: 10.1016/S0304-386X(98)00010-3.

[46] **E. Virčíková and L. Molnár,** "Recovery of copper from dump slag by a segregation process," *Resour. Conserv. Recycl.*, vol. 6, no. 2, pp. 133–138, Feb. 1992, doi: 10.1016/0921-3449(92)90039-5.

[47] **P. Xin, J. Wei, L. Xu, W. Wu, and D. Lan,** "The Recovery of Pb and Zn in Antimony Smelting Slag," in *PbZn 2020: 9th International Symposium on Lead and Zinc Processing*, A. Siegmund, S. Alam, J. Grogan, U. Kerney, and E. Shibata, Eds., in The Minerals, Metals & Materials Series. Cham: Springer International Publishing, 2020, pp. 653–660. doi: 10.1007/978-3-030-37070-1_56.

[48] **F. He,** "A novel method for metal recovery from zinc fuming slags," University of British Columbia, 2001. doi: 10.14288/1.0078672.

[49] **Y. Wang, R. Zhu, Q. Chen, G. Wei, S. Hu, and Y. Guo,** "Recovery of Fe, Ni, Co, and Cu from Nickel Converter Slag through Oxidation and Reduction," *ISIJ Int.*, vol. 58, no. 12, pp. 2191–2199, Dec. 2018, doi: 10.2355/isijinternational.ISIJINT-2018-533.

[50] **F. Burat, H. Baştürkcü, and M. Özer,** "Gold&silver recovery from jewelry waste with combination of physical and physicochemical methods," *Waste Manag.*, vol. 89, pp. 10–20, Apr. 2019, doi: 10.1016/j.wasman.2019.03.062.

[51] **Ş. B. Aydın and A. Gül,** "Environmentally friendly process instead of cyanide leaching on recycling of gold and silver from jewellery scraps and wastes," *Waste Manag. Res.*, vol. 39, no. 2, pp. 233–241, Feb. 2021, doi: 10.1177/0734242X20931947.

[52] **J. P. Vaughan,** "The process mineralogy of gold: The classification of ore types," *JOM*, vol. 56, no. 7, pp. 46–48, Jul. 2004, doi: 10.1007/s11837-004-0092-8.

[53] **R. Nithya, C. Sivasankari, and A. Thirunavukkarasu,** "Electronic waste generation, regulation and metal recovery: a review," *Environ. Chem. Lett.*, vol. 19, no. 2, pp. 1347–1368, Apr. 2021, doi: 10.1007/s10311-020-01111-9.

[54] **J. Yu, E. Williams, and M. Ju,** "Analysis of material and energy consumption of mobile phones in China," *Energy Policy*, vol. 38, no. 8, pp. 4135–4141, Aug. 2010, doi: 10.1016/j.enpol.2010.03.041.

[55] **J. Cui and L. Zhang,** "Metallurgical recovery of metals from electronic waste: A review," *J. Hazard. Mater.*, vol. 158, no. 2–3, pp. 228–256, Oct. 2008, doi: 10.1016/j.jhazmat.2008.02.001.

[56] **C. Saguru, S. Ndlovu, and D. Moropeng,** "A review of recent studies into hydrometallurgical methods for recovering PGMs from used catalytic converters," *Hydrometallurgy*, vol. 182, pp. 44–56, Dec. 2018, doi: 10.1016/j.hydromet.2018.10.012.

[57] **I. Yakoumis, M. Panou, A. M. Moschovi, and D. Panias,** "Recovery of platinum group metals from spent automotive catalysts: A review," *Clean. Eng. Technol.*, vol. 3, p. 100112, Jul. 2021, doi: 10.1016/j.clet.2021.100112.

[58] **J. Xia and A. Ghahreman,** "Platinum group metals recycling from spent automotive catalysts: metallurgical extraction and recovery technologies," *Sep. Purif. Technol.*, vol. 311, p. 123357, Apr. 2023, doi: 10.1016/j.seppur.2023.123357.

[59] **M. E. Holuszko, A. Kumar, and D. C. R. Espinosa,** Eds., "Front Matter," in *Electronic Waste*, 1st ed., Wiley, 2022. doi: 10.1002/9783527816392.fmatter.

[60] **C. S. K. Lin,** Ed., *Chemistry and Chemical Technologies in Waste Valorization*. in Topics in Current Chemistry Collections. Cham: Springer International Publishing, 2018. doi: 10.1007/978-3-319-90653-9.

[61] **J. Hao, Y. Wang, Y. Wu, and F. Guo,** "Metal recovery from waste printed circuit boards: A review for current status and perspectives," *Resour. Conserv. Recycl.*, vol. 157, p. 104787, Jun. 2020, doi: 10.1016/j.resconrec.2020.104787.

[62] **C. Hagelüken**, A. Umicore, and K. Co, *Improving metal returns and eco-efficiency in electronics recycling*. 2006.

[63] **J. B. Legarth, L. Alting, and G. L. Baldo,** "Sustainability issues in circuit board recycling," in *Proceedings of the 1995 IEEE International Symposium on Electronics and the Environment ISEE (Cat. No.95CH35718)*, Orlando, FL, USA: IEEE, 1995, pp. 126–131. doi: 10.1109/ISEE.1995.514963.

[64] **J. Cui and E. Forssberg,** "Characterization of shredded television scrap and implications for materials recovery," *Waste Manag.*, vol. 27, no. 3, pp. 415–424, Jan. 2007, doi: 10.1016/j.wasman.2006.02.003.

[65] **S. Ilyas, M. A. Anwar, S. B. Niazi, and M. A. Ghauri,** "Bioleaching of metals from electronic scrap by moderately thermophilic acidophilic bacteria," *Hydrometallurgy*, vol. 88, no. 1–4, pp. 180–188, Aug. 2007, doi: 10.1016/j.hydromet.2007.04.007.

[66] **L. D. Busselle, T. A. Moore, J. M. Shoemaker, and R. E. Allred,** "Separation processes and economic evaluation of tertiary recycling of electronic scrap," in *Proceedings of the 1999 IEEE International Symposium on Electronics and the Environment (Cat. No.99CH36357)*, May 1999, pp. 192–197. doi: 10.1109/ISEE.1999.765874.

[67] **L. Theo,** "Integrated recycling of non-ferrous metals at Boliden Ltd. Ronnskar smelter," *Proc. 1998 IEEE Int. Symp. Electron. Environ. ISEE - 1998 Cat No98CH36145*, pp. 42–47, 1998, doi: 10.1109/ISEE.1998.675028.

[68] **J. E. Hoffmann,** "Recovering precious metals from electronic scrap," *JOM*, vol. 44, no. 7, pp. 43–48, Jul. 1992, doi: 10.1007/BF03222275.

[69] **L. S. Morf, J. Tremp, R. Gloor, F. Schuppisser, M. Stengele, and R. Taverna,** "Metals, non-metals and PCB in electrical and electronic waste – Actual levels in Switzerland," *Waste Manag.*, vol. 27, no. 10, pp. 1306–1316, Jan. 2007, doi: 10.1016/j.wasman.2006.06.014.

[70] **D. Dutta *et al.*,** "A review on recovery processes of metals from E-waste: A green perspective," *Sci. Total Environ.*, vol. 859, p. 160391, Feb. 2023, doi: 10.1016/j.scitotenv.2022.160391.

[71] **C. Hagelüken,** "Precious metals process catalysts: Material flows and recycling," *Chim. Oggi*, vol. 24, pp. 14–17, Jan. 2006.

[72] **J. Hait, R. K. Jana, and S. K. Sanyal,** "Processing of copper electrorefining anode slime: a review," *Miner. Process. Extr. Metall.*, vol. 118, no. 4, pp. 240–252, Dec. 2009, doi: 10.1179/174328509X431463.

[73] **F. Burat, A. Demirağ, and M. C. Şafak,** "Recovery of noble metals from floor sweeping jewelry waste by flotation-cyanide leaching," *J. Mater. Cycles Waste Manag.*, vol. 22, no. 3, pp. 907–915, May 2020, doi: 10.1007/s10163-020-00982-y.

[74] **C. W. Corti,** "Recovery of Refining of Gold Jewellery Scraps and Wastes" The Santa Fe Symposium on Jewelery Manufacturing Technology, 2002

[75] **C. Durmaz,** "Kuyumculuk Kökenli Cüruflardan Fiziksel Zenginleştirme Yöntemleri ile Altın Geri Kazanımı," Istanbul Technical University, 2012.

[76] **C. Liu, S. Sun, G. Tu, and F. Xiao,** "A novel method for extraction of platinum from spent automotive catalyst: utilization of spent fluid catalytic cracking catalyst as flux," *Environ. Technol.*, vol. 44, no. 2, pp. 139–149, Jan. 2023, doi: 10.1080/09593330.2021.1965662.

[77] **Y. Ding, H. Zheng, S. Zhang, B. Liu, B. Wu, and Z. Jian,** "Highly efficient recovery of platinum, palladium, and rhodium from spent automotive catalysts via iron melting collection," *Resour. Conserv. Recycl.*, vol. 155, p. 104644, Apr. 2020, doi: 10.1016/j.resconrec.2019.104644.

[78] **H. Tang *et al.*,** "Recycling of platinum-group metals from spent automotive catalysts by smelting," *J. Environ. Chem. Eng.*, vol. 10, no. 6, p. 108709, Dec. 2022, doi: 10.1016/j.jece.2022.108709.

[79] **H. Tang *et al.*,** "Recovery of platinum-group metals from spent catalysts by microwave smelting," *J. Clean. Prod.*, vol. 318, p. 128266, Oct. 2021, doi: 10.1016/j.jclepro.2021.128266.

[80] **S. Ilyas, R. R. Srivastava, H. Kim, and H. A. Cheema,** "Hydrometallurgical recycling of palladium and platinum from exhausted diesel oxidation catalysts," *Sep. Purif. Technol.*, vol. 248, p. 117029, Oct. 2020, doi: 10.1016/j.seppur.2020.117029.

[81] **S. Ilyas, H. Kim, and R. R. Srivastava,** "Hydrometallurgical Recycling of Rare Earth Metal–Cerium from Bio-processed Residual Waste of Exhausted Automobile Catalysts," *JOM*, vol. 73, no. 1, pp. 19–26, Jan. 2021, doi: 10.1007/s11837-020-04471-3.

[82] **F. Zotin, O. Gomes, C. Oliveira, A. Neto, and M. Cardoso,** "Automotive catalyst deactivation: Case studies," *Catal. Today*, vol. 107, pp. 157–167, Oct. 2005, doi: 10.1016/j.cattod.2005.07.111.

[83] **H. B. Trinh, J. Lee, Y. Suh, and J. Lee,** "A review on the recycling processes of spent auto-catalysts: Towards the development of sustainable metallurgy," *Waste Manag.*, vol. 114, pp. 148–165, Aug. 2020, doi: 10.1016/j.wasman.2020.06.030.

[84] **I. Yakoumis, M. Panou, A. M. Moschovi, and D. Panias,** "Recovery of platinum group metals from spent automotive catalysts: A review," *Clean. Eng. Technol.*, vol. 3, p. 100112, Jul. 2021, doi: 10.1016/j.clet.2021.100112.

[85] **D. Jimenez de Aberasturi, R. Pinedo, I. Ruiz de Larramendi, J. I. Ruiz de Larramendi, and T. Rojo,** "Recovery by hydrometallurgical extraction of the platinum-group metals from car catalytic converters," *Miner. Eng.*, vol. 24, no. 6, pp. 505–513, May 2011, doi: 10.1016/j.mineng.2010.12.009.

[86] **C. Saguru, S. Ndlovu, and D. Moropeng,** "A review of recent studies into hydrometallurgical methods for recovering PGMs from used catalytic converters," *Hydrometallurgy*, vol. 182, pp. 44–56, Dec. 2018, doi: 10.1016/j.hydromet.2018.10.012.

[87] **A. Fornalczyk and J. Willner,** "Dissolution of ceramic monolith of spent catalytic converters by using hydrometallurgical methods," *Arch. Metall. Mater.*, vol. 60, pp. 2945–2948, Dec. 2015, doi: 10.1515/amm-2015-0470.

[88] **A. S. Kirichenko, A. N. Seregin, and A. I. Volkov,** "Developing a Technology for Recycling Automotive Exhaust-Gas Catalysts," *Metallurgist*, vol. 58, no. 3, pp. 250–255, Jul. 2014, doi: 10.1007/s11015-014-9897-z.

[89] **A. Fornalczyk *et al.*,** "Dissolution of Metal Supported Spent Auto Catalysts in Acids," *Arch. Metall. Mater.*, vol. 61, no. 1, pp. 233–236, Mar. 2016, doi: 10.1515/amm-2016-0043.

[90] **C. A. Nogueira, A. P. Paiva, P. C. Oliveira, M. C. Costa, and A. M. R. da Costa,** "Oxidative leaching process with cupric ion in hydrochloric acid media for

recovery of Pd and Rh from spent catalytic converters," *J. Hazard. Mater.*, vol. 278, pp. 82–90, Aug. 2014, doi: 10.1016/j.jhazmat.2014.05.099.

[91] **S. Chen, S. Shen, Y. Cheng, H. Wang, B. Lv, and F. Wang,** "Effect of O2, H2 and CO pretreatments on leaching Rh from spent auto-catalysts with acidic sodium chlorate solution," *Hydrometallurgy*, vol. 144–145, pp. 69–76, Apr. 2014, doi: 10.1016/j.hydromet.2014.01.018.

[92] **M. Kim, S. Park, J. Lee, and P. K. Choubey,** "A novel zero emission concept for electrogenerated chlorine leaching and its application to extraction of platinum group metals from spent automotive catalyst," *Hydrometallurgy*, vol. 159, pp. 19–27, Jan. 2016, doi: 10.1016/j.hydromet.2015.10.030.

[93] **A. Chen, S. Wang, L. Zhang, and J. Peng,** "Optimization of the microwave roasting extraction of palladium and rhodium from spent automobile catalysts using response surface analysis," *Int. J. Miner. Process.*, vol. 143, pp. 18–24, Oct. 2015, doi: 10.1016/j.minpro.2015.08.007.

[94] **C.-H. Kim, S. I. Woo, and S. H. Jeon,** "Recovery of Platinum-Group Metals from Recycled Automotive Catalytic Converters by Carbochlorination," *Ind. Eng. Chem. Res.*, vol. 39, no. 5, pp. 1185–1192, May 2000, doi: 10.1021/ie9905355.

[95] **A. K. Upadhyay, J. Lee, E. Kim, M. Kim, B.-S. Kim, and V. Kumar,** "Leaching of platinum group metals (PGMs) from spent automotive catalyst using electro-generated chlorine in HCl solution," *J. Chem. Technol. Biotechnol.*, vol. 88, no. 11, pp. 1991–1999, 2013, doi: 10.1002/jctb.4057.

[96] **S. Harjanto *et al.***, "Leaching of Pt, Pd and Rh from Automotive Catalyst Residue in Various Chloride Based Solutions," *Mater. Trans.*, vol. 47, no. 1, pp. 129–135, 2006, doi: 10.2320/matertrans.47.129.

[97] **H. Dong, J. Zhao, J. Chen, Y. Wu, and B. Li,** "Recovery of platinum group metals from spent catalysts: A review," *Int. J. Miner. Process.*, vol. 145, pp. 108–113, Dec. 2015, doi: 10.1016/j.minpro.2015.06.009.

[98] **Y. Ding, S. Zhang, B. Liu, H. Zheng, C. Chang, and C. Ekberg,** "Recovery of precious metals from electronic waste and spent catalysts: A review,"

Resour. Conserv. Recycl., vol. 141, pp. 284–298, Feb. 2019, doi: 10.1016/j.resconrec.2018.10.041.

[99] **G. Kolliopoulos, E. Balomenos, I. Giannopoulou, I. Yakoumis, and D. Panias,** "Behavior of Platinum Group Metals during Their Pyrometallurgical Recovery from Spent Automotive Catalysts," *Open Access Libr. J.*, vol. 1, no. 5, Art. no. 5, Aug. 2014, doi: 10.4236/oalib.1100736.

[100] **A. Fornalczyk and M. Saternus,** "Possible ways of refining precious group metals (PGM) obtained from recycling of the used auto catalytic converters," *Metal. -Sisak Then Zagreb.*, vol. 52, pp. 267–270, Jun. 2013.

[101] **L. Zhang, Q. Song, Y. Liu, and Z. Xu,** "Novel approach for recovery of palladium in spent catalyst from automobile by a capture technology of eutectic copper," *J. Clean. Prod.*, vol. 239, p. 118093, Dec. 2019, doi: 10.1016/j.jclepro.2019.118093.

[102] **G. You, W. Fang, Q. Li, Y. Ma, X.-T. Yang, and H. Yang,** "Study on enrichment method of platinum, palladium and rhodium in spent auto-catalysts," vol. 36, pp. 7–11, May 2016, doi: 10.13228/j.boyuan.issn1000-7571.009680.

[103] **M. Morcali,** "A new approach to recover platinum-group metals from spent catalytic converters via iron matte," *Resour. Conserv. Recycl.*, vol. 159, p. 104891, Aug. 2020, doi: 10.1016/j.resconrec.2020.104891.

[104] **Z. Peng *et al.*,** "Thermodynamic Analysis of Smelting of Spent Catalysts for Recovery of Platinum Group Metals," in *9th International Symposium on High-Temperature Metallurgical Processing*, J.-Y. Hwang, T. Jiang, M. W. Kennedy, D. Gregurek, S. Wang, B. Zhao, O. Yücel, E. Keskinkilic, J. P. Downey, Z. Peng, and Rafael. Padilla, Eds., in The Minerals, Metals & Materials Series. Cham: Springer International Publishing, 2018, pp. 215–223. doi: 10.1007/978-3-319-72138-5_22.

[105] **Z. Peng *et al.*,** "Pyrometallurgical Recovery of Platinum Group Metals from Spent Catalysts," *JOM*, vol. 69, no. 9, pp. 1553–1562, Sep. 2017, doi: 10.1007/s11837-017-2450-3.

[106] **R. T. Jones and I. J. Geldenhuys,** "The pros and cons of reductive matte smelting for PGMs," *Miner. Eng.*, vol. 24, no. 6, pp. 495–498, May 2011, doi: 10.1016/j.mineng.2011.03.007.

[107] **B. Friedrich, M. Kalisch, D. Friedmann, R. Degel, F. Kaußen, and J. Böhlke,** "The Submerged Arc Furnace (SAF): State-of-the-Art Metal Recovery from Nonferrous Slags," *J. Sustain. Metall.*, vol. 4, no. 1, pp. 77–94, Mar. 2018, doi: 10.1007/s40831-017-0153-1.

[108] **M. Karbowniczek,** *Electric Arc Furnace Steelmaking*, 1st ed. Boca Raton: CRC Press, 2021. doi: 10.1201/9781003130949.

[109] **J. Madias,** "Chapter 1.5 - Electric Furnace Steelmaking," in *Treatise on Process Metallurgy*, S. Seetharaman, Ed., Boston: Elsevier, 2014, pp. 271–300. doi: 10.1016/B978-0-08-096988-6.00013-4.

[110] **R. Orman,** "Laboratuvar Tipi Elektrik Ark FIrını Tasarımı ve E-atıktan Öğütlebilir Alaşım Üretimi," p. 102, 2019.

[111] **R. T. Jones, Q. G. Reynolds, and M. J. Alport,** "DC arc photography and modelling," *Miner. Eng.*, vol. 15, no. 11, Supplement 1, pp. 985–991, Nov. 2002, doi: 10.1016/S0892-6875(02)00167-X.

[112] **A. N. Makarov, V. V. Rybakova, and M. K. Galicheva,** "Electromagnetism and the Arc Efficiency of Electric Arc Steel Melting Furnaces," *J. Electromagn. Anal. Appl.*, vol. 06, no. 07, pp. 184–192, 2014, doi: 10.4236/jemaa.2014.67018.

[113] **H. Andrei, C. Cepisca, and S. Grigorescu,** "Power Quality and Electrical Arc Furnaces," in *Power Quality*, A. Eberhard, Ed., InTech, 2011. doi: 10.5772/15996.

[114] **M. F. Hoyaux,** *Arc Physics*, vol. 8. in Applied Physics and Engineering, vol. 8. Berlin, Heidelberg: Springer Berlin Heidelberg, 1968. doi: 10.1007/978-3-642-85652-5.

[115] **A. Vignes,** "Electric Melting and Smelting Furnaces," in *Extractive Metallurgy 3: Processing Operations and Routes*, John Wiley & Sons, Ltd, 2013, pp. 217–263. doi: 10.1002/9781118617106.ch8.

[116] **F. A. Oyawale,** "Design and Prototype Development of a Mini-Electric Arc Furnace," *Metals*, vol. 8, no. 1, 2007.

[117] **J. H. L. Voncken,** "Recovery of Ce and La from Spent Automotive Catalytic Converters," in *Critical and Rare Earth Elements*, CRC Press, 2019.

[118] **D. Yang, Q. Yang, W. Ma, X. Ma, S. Wang, and Y. Lei,** "Characteristics of spent automotive catalytic converters and their effects on recycling platinum-group-metals and rare-earth-elements," *Sep. Purif. Technol.*, vol. 308, p. 122977, Mar. 2023, doi: 10.1016/j.seppur.2022.122977.

CURRICULUM VITAE

Name Surname : Mert Saraçoğlu

EDUCATION :

- **B.Sc. :** 2021, Istanbul Technical University, Chemistry-Metallurgy Faculty, Material and Metallurgical Engineering Department

PROFESSIONAL EXPERIENCE AND REWARDS:

- 2020 – Currently Co-founder, Nanosilver Inc. İstanbul Teknopark, Pendik, İstanbul Turkey
- 2018 – Currently Graduate – Undergraduate Researcher, ITU Electrometallurgy Lab
- 2021 High Honor List for > 3.50 GPA in Chemistry and Metallurgy Faculty
- 2020 High Honor List for for > 3.50 GPA in Chemistry and Metallurgy Faculty
- 2020 Best Paper Reward on 6th World Congress on New Technologies

PUBLICATIONS, PRESENTATIONS AND PATENTS ON THE THESIS:

- **Saraçoğlu, M.,** Ayvaz, B., Karaman S., Dizdar K., Gezici, U., S., Timur (2023): Enrichment of PGMs From Waste Auto-catalytic Convertors: Lab-scale Arc Furnace Design and Slag Optimization, International Conference on Materials Science and Manufacturing, November 17-18, 2007 Karaman, Turkey.